Non-invasive near-field THz imaging using a single pixel detector

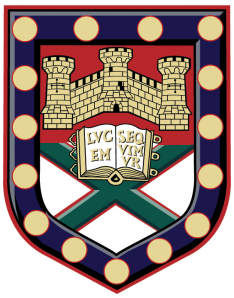

Rayko Ivanov Stantchev

School of Physics

University of Exeter

A thesis submitted for the degree of

Doctor of Philosophy

Signature:..... March 2017

Non-invasive near-field THz imaging using a single pixel detector

Submitted by Rayko Ivanov Stantchev to the University of Exeter as a thesis for the degree of Doctor of Philosophy in Physics
2017

I certify that all material in this thesis which is not my own work has been identified and that no material has previously been submitted and approved for the award of a degree by this or any other University.

Rayko Ivanov Stantchev
2017

Аз, Райко Иванов и Станчев, посвещавам тази страница на мама и тате заради техните само жертвания за да мога да създам този документ.

I, Rayko Ivanov Stantchev, dedicate this page to mum and dad for their self sacrifices so that I could create this document.

И за Звездите които гледат за нас
And to the Stars that watch over us

Preamble ramble: d[° △ °]b

Sorry I'm still preambling...

In the present day, we heavily use writing to communicate our thoughts via this medium we call the *internet*. So, I will use it to communicate my thoughts to you dear reader. And yea I want to stamp my identity on this document. I don't want to pretend that I am not human and didn't feel a myriad of emotions related and not related to the creation of this works. *The Sun shines every day,* and not knowing the grammatical rules of this language I might not stick to them and apologize if this next bit is a sketchy ride into my thoughts. Аз не се шегувам ;) As a child, I was terrible at sticking inside the lines when colouring in things. And I still am terrible. So as I write this, I wonder what the writing process is like for you dear Reader. I get lost and forget I am human until I am reminded otherwise by the needs of my body...

Even at the end, as I write this thing, I still remember the day I began this PhD. I had no idea of what I was about to embark upon and neither could I imagine the things I would learn. I was free of expectation, filled with naive innocence, empty of despair and full of hope. And now? I can imagine the thousands upon thousands of students that have worked hard so that as a collective we could have the photo-lithographic technology used to create the laptop in front of me now. The keys I am pressing, the mouse I move and the screen pixels I now command. Oh deary me, I wish that no one would have to hold all of those technical details in their head! With the loss of the naive innocence I once had I appear to have become sad. I believe this to be due to my observation of how science is portrayed by society and the media in general.

In 1986, scientists at a conference announced that we, as a collective, are causing a mass extinction event. An event similar to what had occurred when the dinosaurs became extinct. This news made it onto page 26 of the New York times, *"Action is urged to save species"* By Philip Shabecoff, Special to the New York Times Published: September 28, 1986. There was 26 pages of thoughts to share that were deemed more important than then we are annihilating life on our planet. Where as an article with a title *"iPhone 8 production will start sooner than expected, report suggests"* by Andrew Griffin, Independent Newspaper, 08/FEB/2017 makes it near the front of the technology section in UK newspaper *The Independent*. I guess us not killing life on the planet is not profitable. Therefore, you must gives us better technology that will

save us from our boredom, allow us to escape our problems, be profitable and make us control the elements with greater ease. This previous sentence is what I feel that human society is demanding from the scientific collective. This really worries me as its manifestation, I believe, is that a piece of scientific research will only be funded depending if it is profitable or it helps other people do things. Whilst helping people appears kind and noble, helping someone kill a million people is not. For example, the nuclear bomb... Therefore, helping others is not kind and noble in all cases. The profitable part, on April/24/1965 Clair C. Patterson published an article named *"Contaminated and Natural Lead Environments of Man"*. With this article Patterson attempted to raise public awareness that our car industry, in particular the leaded petrol used by cars then, has increased the levels of lead in the environment and the food chain. He fought against the lobbying power of petrol companies. Even though his arguments were you are literally killing yourselves and everyone else, the petrol companies still fought a 20 year campaign to protect their profits which included funding research which proved Patterson wrong.

Not that I really care about any of this nonsense in the previous paragraph. I just wanted to point it, sorry. I really like to point out what is obvious in life, like a lamp post on the road. But I always regret doing such things because it is soo funny when somebody walks into a post! :D

I am not going to condemn society! No! I live a good life. I am not going to condemn a society whose best description, I believe, was given by a Hopi[1] elder: *You all have watches but have no time.* Rushing endlessly and endlessly amidst the concrete jungles of our metropolitan cities. Physically so close to each other yet I can not help but feel lonely amongst soo many people. If you look at someone in the eyes and smile, the reaction of "Why is this person looking at me? What a creep!" occurs at too high of a frequency in my opinion. yeah (° ‿ °) The next point I wish to illuminate is the works of John B. Calhoun, *Population Density and Social Pathology,* Scientific American, February 1962. I'm only pointing to it coz I'm too scared to talk about the details... I don't think we, as a species evolved to live in hunter-gatherer communities, are able to handle the amount of human contact we have to deal with on a daily basis.

Aah, loom and gloom. It's always there so don't worry! Of the utmost importance is to not get up caught up on perfection but on progress. The world is beautiful in all

[1] The Hopi wikipedia link or something goes here at some point...

its fractal aesthetics and fragile symmetry. It begins and ends like a story, temporal and impermanent. But as this day turns to night I wonder, are these things nothing more than human constructs used to describe the ever changing shapes and forms that dance in the emptiness of this physical reality? A reality composed of complex phenomelogical effects that when understood with simple causal principles, an awe-inspiring feeling arises. Like a living thing it consumes and nourishes the inner depths of your mind. So come on work yourself harder coz it's boring when a dancer doesn't push themselves to the point at which they might breakdown. Down, and down you'll roll on the mountain slopes where you'll find Truth dotted about everywhere and create Beauty every time you take a poop (according to the flies anyways). So don't worry about a thing, coz you've found the elegance of this moment.

The ugliness, I hope you've found. What the hell happens in this world? I don't even know what space is! There is no set of axioms that can prove their own consistency and this statement is unprovable. Well isn't that funny? This statement is false. I can't say it's true or false due to the self-reference within the statement. I find it very interesting that such paradoxes are created from self-reference; it just talks about itself. I did this and I did that so I am this. The self: aaaa who am I? I have no idea, I just know I came out of this world and you can get multiple reflections if you don't set your boundary conditions right, then the overall solution is compromised. But what if you get an infinite number of reflections? Should I even contemplate infinity? A concept we came up with coz no one could be asked to count all the natural numbers... I certainly can't! And so I ask will the square root of minus one remain after humanity is gone. I dunoo; surely it must! So here's a self-referring question: why was the question why created?

We are the universe thinking about itself,
so count the stars
and the number of sunsets you've seen.
And tell me what you see,
because I do wonder about you!
Thank you dear reader.
d[° Δ °]b

Acknowledgements

And what is any human being without those around him?

This first person on this thanks list is *Euan Hendry*, my PhD supervisor. His constant curiosity in my work is something that pushed my forward and made me realize that my work is worth something. I can assure you that if you think your work is not worth while then you end up in an pit of abysmal thoughts of hatred and despise towards the world around you. *Euan*'s never ending curiosity pulled me out of this pit uncountable number of times and gave me the will to carry on going forward.

The next thanks goes to *Sam Hornett,* a postdoctoral researcher in our group. An impressive title, but then you realize he is just a normal human being who has his good and bad days. Seeing someone with an impressive set of a capabilities look like they wanna cry because their experiment never wants to work gives you the realization that you are not alone. This is the life you have embarked upon and now you have to grit your teeth, bite the bullet and walk forward with a straight back! The blood, sweat and tears will never cease to be shed.

Peter A. Hobson, the person from QinetiQ who funded my PhD. I had to speak to him every 3 months about my progress. He was always interested in my work and talked about other cool physics fields. So he helped with the same problem as Euan, but I didn't have to speak to him all the time. Hence, whenever I did speak to him it felt like a nice break where I'd get to speak to someone about the details of my work. It is rare to speak to someone about the details of your work, so it felt nice.

The Spanish crew: *Alba & Sergio Paniagua, Santiago G.-C. Carrilo, Erik O. B. Para* and *Gloria S. Alvear.* They were a happy bunch who knew how to party, but they were humble about the basic necessities of life. I only remember laughing in stitches with them, enjoying nice food and smiling so much my cheeks would always hurt :)

The Buddhist crew, a fun loving people who make effort to kind and compassionate. They give you something else to focus on. Namely, how to achieve happiness through all the pain and sorrow that life bestows upon those experiencing it. It is

an important problem to work upon I assure you, however it was nice to engage in something where you couldn't succeed or fail.

Kate Evans, a girl with whom I had many cups of tea that kept me sane somehow. Yep, they were soo enjoyable she gets a lil paragraph all to herself over here. There's many things we discussed during our encounters and I am happy we did.

Bleddyn Williams, a dude from my undergraduate course. Yep, during the start of my PhD whenever I wanted to have a cup of tea to relax from the stresses of my work, I'd ring him and be like "Cuppa tea in 15 mins?". That is something that I will forever remember and be thankful for!

And the final acknowledgement goes to my blood relatives: *Lidia Stantcheva* (mother), *Ivan Stantchev* (father), *Rayko Stantchev* (granddad), *Marin Marinov* (granddad), *Maria Marinova* (grandmother) & *Nadejda Stantcheva* (grandmother). There is nothing like complaining about how your experiment has failed, then remembering the stories of how your grandfathers were sent to the front line of world of 2 when they were the same age as you. These are the people that have raised me since birth and forged a mind capable of carrying the work necessary for creating this document.

So thank you all!

And to answer my question;
Without those around oneself,
a human is **** all!
Just a tiny spec of dust
on a minuscule planet
crusading through the endless caverns of space.
Don't despair though dear Reader, that's where the fun part is!

Abstract

The terehertz radiation potentially has many interesting applications. From airport security, non-destructive evaluations of electronics and space shuttle panels, to non-ionizing photon energies with the potential to detect cancer growths and quality control of pharmaceutical tables, the list of potential applications is vast as shown in chapter 1. However, there is a lack of cheap, robust and efficient THz sources, detectors and modulators. Further, the long wavelengths render micron sized details unseeable with far-field imaging techniques. This has rendered most imaging applications unusable in the real world. This thesis is based around demonstrating an imaging technique that uses a near-field THz modulator to obtain sub-wavelength images. There are five distinct experimental demonstrations that show the full capacity of the imaging technique developed here.

Chapter 2 gives an outline of the background physics knowledge needed to understand the entirety of the thesis. An outline of the mathematics used for modelling is given in the latter part of the chapter as well. Chapter 3 gives a background on the THz generation and detection techniques used in our THz-TDS system, optical rectification and electro-optic sampling in ZnTe. Further more, our system is capable of photoexciting a sample in conjunction to it being probed with a THz pulse. For the most part, we photoexcite a silicon wafer in order to use its photoconductive properties to modulate our THz pulse. Our photoexcitation pulse is spatially modulated, via a digital micromirror device, which in turn spatially modulates our THz pulse. This patterned THz pulse can then be used with a single-element detector to perform imaging. How to do this and the type of patterns needed is described in the latter part of chapter 3.

Chapter 4 is the first demonstration that photo-induced conductivity in silicon can be used to manipulate evanescent THz fields for sub-wavelength imaging. For this, we imaged a 1D sub-wavelength slit and were able to obtain the slit profile with 65μm ($\lambda/6$ at $0.75THz$) resolution.

Chapter 5 demonstrates what limits the resolution in our imaging system. Namely, the distance which the patterned THz pulse propagates to the object from where it

was spatially modulated. We demonstrate $9\mu m$ ($\lambda/45$ at $0.75THz$) resolution using an ultra-thin ($6\mu m$) silicon wafer. At such sub-wavelength scales polarization becomes an important factor. We show how one can use polarization in order to detect $8\mu m$ breaks in a circuit board hidden by $115\mu m$ of silicon.

Chapter 6 concerns itself with showing how noise affects our images. Further more, our imaging system is compatible with compressed sensing where one can obtain an image using fewer measurements than the number of pixels. We investigate how different under-sampling techniques perform in our system. Note under-sampling at sub-wavelength resolutions, as is done here, is rather unusual and is of yet to be demonstrated for other part of the electro-magnetic spectrum.

Chapter 7 shows that one does not need to photoexcite silicon. One can in principle illuminate any material, hence we photoexcite graphene with our spatially modulated optical pulses. This allows us to obtain the THz photoconductive response of our graphene sample with sub-wavelength resolution ($75\mu m \approx \lambda/5$ at $0.75THz$). We compare our results with Raman spectra maps. We find a clear correlation between THz photoconductivity and carrier concentration (extracted from Raman).

Chapter 8 exploits the full capacity of our imaging system by performing hyper-spectral near-field THz imaging on a biological sample. For this, in our imaged field of view, we measured the full temporal trace of our THz pulse at a sub-wavelength spatial resolution. This has allowed us to extract the frequency dependent permittivity of our biological sample, articular cartilage, over our spectral range (0.2-2THz). We find the permittivity to change on a sub-wavelength scale in correlation with changes in the structure of our sample. However, the permittivity extraction procedures that have been developed make a far-field approximation. We mathematically show the presence of the THz near-fields to render the long wavelength spectral parts of our extracted permittivity to be wrong.

Chapter 9 is where we conclude and point out the main problem that needs to be addressed in order to make the measurements presented here more accessible to others. Namely, the cost of the laser system powering the THz-TDS and how to further reduce the acquisition time.

Contents

List of Figures

Nomenclature

Abbreviations

CVD Chemical vapour deposition

CW Continuous wave

DMD Digital micro-mirror device

EM Electromagnetic

EO Electro-optic

THz Terahertz

THz-TDS Terahertz time-domain spectrometer

TV Total variation

ZnTe Zinc telluride

Definitions

$Microwave\ regime$ $1 \rightarrow 200$ GHz

$Optical/Visible\ regime$ $300 \rightarrow 1000$ THz

$Terahertz\ regime$ $0.2 \rightarrow 3$ THz

Equipment

Balanced photo-diodes: Model 2007 Nirvana Auto-Balanced Photoreceiver

Digital micromirror device: $DLP\ lightcrafter\ evaluation\ module$ from Texas Instruments

Lock-In amplifier: Model 7270 from SIGNAL RECOVERY

Ti:Sapphire regenerative amplifier model: $Coherent\ Legend\ Elite$, 800nm 100fs pulses, 3mJ per pulse, 1050Hz repetition rate

Ti:Sapphire seed laser model: $Coherent\ Vitese$, 800nm 85fs pulses, 12nJ per pulse, 80MHz repetition rate

Publications

R. I. Stantchev, B. Sun, S. M. Hornett, P. A. Hobson, G M. Gibson, M. J. Padgett, E. Hendry *Noninvasive, near-field terahertz imaging of hidden objects using a single-pixel detector* Science Advances **2** e160019 (2016)

R. I. Stantchev, D. B. Phillips, P. A. Hobson, S. M. Hornett, S. M. Hornett, E. Hendry *Compressed sensing with near-field THz imaging* submitted to Optica

R. I. Stantchev, J. Mansfield, R. S. Edginton, P. A. Hobson, F. Palombo, E. Hendry *Subwavelength hyperspectral THz studies of articular cartilage* submitted to Physical review X

R. I. Stantchev, S. M. Hornett, P. A. Hobson, E. Hendry *Enhanced THz transmission and imaging of a sub-wavelength slit via light induced diffraction* Physical Review A **92**, pp.043820 (October 2015)

S. M. Hornett, R. I. Stantchev, M. Z. Vardaki, C. Beckerleg, E. Hendry *Subwavelength Terahertz Imaging of Graphene Photoconductivity* Nano Letters **16** pp. 7019−7024 (2016)

Chapter 1

Introduction

1.0.1 A paragraph on the history of THz

The birth of THz science as we know it today can be traced to back the late 1960s with the studies of the materials responses to the newly developed ultrafast picosecond pulsed lasers. Research continued into improved laser performance and better fabrication methods of materials needed for the THz detection and generation processes, thus the 1990s saw the creation of the standard layout for the modern THz time-domain spectrometer (THz-TDS). Most THz-TDS are based on photoconductive antennas (PCA), or on an electro-optical (EO) crystal, being illuminated by a pulsed laser. Such systems are large, heavy and expensive, thus the development of more compact commercially utilizable systems has been on going since the late 1990s. Companies such as TeraView (UK), Picometrix (USA), Toptica (Germany), Advantest (Japan) and Zomega (USA) offer integrated systems of various sizes and functionalities. A fuller history of terahertz can be found in ref. [1].

1.1 Uses and applications of THz

In the last two decades, the THz frequency range (0.2-2 THz) has attracted a lot of attention due its unique properties [2–4]. Many many low frequency vibrations of molecules and solids lie in here [5]. For industrial applications, most non-conductive materials and non-polar liquids are THz transparent. This is useful for non-invasive inspection of many multi-component or buried systems, such as defects in space shuttle panels [6] and complex electronic circuits [7, 8]. Further, the low photon energies will

not damage sensitive electronics [9]. THz can also be used in quality control of pharmaceutical tablets [10, 11]. Most molecules have a unique THz spectral fingerprint, which allows for the sensing of explosive and illegal substances [12]. Spectroscopic THz imaging has been used in uncovering the material composition and substructure of paintings, murals or frescoes [13].

For bio-medical applications the non-ionizing THz photon energies are of great interest for biological tissue evaluation [14, 15]. Further, the high THz sensitivity to polar molecules are qualities of much interest in the diagnosis of cancer [4, 16]. Here, cancerous cells greater absorption coefficients compared to healthy cells. Moreover, many low-frequency vibrational modes of biological molecules in aqueous media lie in this frequency range, allowing THz spectroscopy to identify and characterize inter-molecular bonding in amino acids [17], sugars [18], DNA [19] and proteins [20], as well as dynamics at biomolecule-water interfaces [21] and in photoactive proteins [22]. Furthermore, long-range collective vibrational modes, which mediate structural changes and the reaction coordinates critical to the function of active proteins [23], normally manifest themselves at THz frequencies. Whilst THz spectroscopy can readily identify such vibrational modes [24], there are several difficulties in the determination of structural features of these systems. These are discussed in the section below.

1.2 THz imaging technology now

To image with EM-radiation one must detect and generate said wavelengths. Unlike the visible regime, materials that exhibit bandgaps in the THz regime are few. This has rendered THz technology to be cumbersome and expensive. For generation of CW THz there exist: far-infrared gas lasers [25], germanium THz lasers [26], quantum cascade lasers [27] and free-electron lasers [28] to name a few. All of these sources are either expensive or lack broadband tunability ($\geq 0.5THz$). There are broadband pulsed THz sources, namely photoconductive antennas [29], non-linear crystals [30] and plasma mixing in air [31]. These methods are commonly used in THz-TDS systems due to their broadband frequency range and picosecond temporal resolution. However, they have weak field strengths and are powered by expensive, large, amplified femtosecond laser systems [32]. Recently, the size and cost of a THz-TDS has been highly reduced by dispensing away the amplified laser system and using a femtosecond

solid state laser instead [33].

For thermal detection of THz there exist bolometers [34], pyroelectric detectors [35] and Golay Cells [36]. Further, THz detector arrays exist but they are typically low-bandwidth or require cryo-genetic temperatures for operation [37, 38]. Nevertheless, there is progress [39]. These are typically used to detect CW sources. Picosecond THz pulses are detected in THz-TDS systems via photoconductive antennas [29] and with non-linear crystals [30]. These are normally limited by photoexcited saturation of charge carriers [40] and crystal phonon absorption resonances [41] respectively. THz detection using air ionized plasma is free of such limitations [42] giving rise to larger bandwidths, however this method can only be used for far-field detection to prevent sample damage from plasma filament.

Near-field THz imaging is typically done by scanning a tapered metal tip in the near-field of a sample. One of the initial demonstrations of this technique achieved $\lambda/4$ resolution [43]. It is also possible to use a vibrating metal tip, as in the case of apertureless near-field scanning optical microscopy, to yield a resolution of a few μm [44]. Alternatively, one can use THz fields to modulate the bias in a scanning tunnelling microscope, which yields a resolution of a few nm for some specific samples [45–47]. However, these tip scanning methods are inherently slow and invasive [48]. Image acquisition speed can be improved by placing an EO detection crystal in the near-field of a sample [49]. However, this requires a complex detection scheme.

In regards to biological imaging there is two main problems. The first problem, owing to the long wavelengths employed (λ=300μm at 1THz), near-field approaches are required to get sub-mm resolution. However, imaging techniques involving scanning near-field tips can perturb the sample or require nm-flat surfaces. This renders the techniques of refs [43–47] unusable. The second problem, samples have to be kept hydrated for normal biological function to be maintained, which is problematic due to the large THz absorption of water [50]. For this, it is usually necessary to encapsulate biological samples to maintain hydration, severely restricting the resolution achievable by scanning apertures, and the apertures themselves typically have a very strong frequency response [51] making them unusable for spectroscopic applications. For these reasons, subwavelength spectroscopic THz measurements of biological samples, although existent [52–54], have been plagued by problems. Consequently, biological imaging has mostly been restricted to large structures such as organs [55, 56].

1.3 Imaging with single-element detectors

Imaging with a single-element detector has been around since the 1970s [57]. However, at that time the spatial encoding masks had to be physically made thus rendering these techniques awkward to use. Furthermore, imaging with a single-element detector requires that measurements have to be taken sequentially (as opposed to in parallel as is done with detector arrays) which hinders the acquisition rate. These two things prevented their wide spread use. However, in recent years there has been increased attention towards such imaging techniques. There are two reasons. First, the development of spatial light modulators, such as digital micro-mirror devices (DMD), has enabled one to spatially encode a beam of radiation without making a physical mask. Second, such techniques are compatible with compressed sensing [58], a field born in 2006 with two papers [59, 60], where one obtains an image using fewer measurements than the number of pixels.

Imaging with a single-element detector has been implemented in the THz regime [61–66]. All of these works use photoconductivity in semiconductors in order to create a THz spatial modulator (details of this are given in chapter 3). However, all these studies have been performed in the far-field, hence the spatial resolutions are around $0.5mm$. Finally, it does need to be noted that using photoconductivity in semiconductors for near-field THz imaging has been performed in 2000 [67]. However, spatial light modulators were non-existent when this proof-of-principle demonstration was first performed. Therefore, they were limited to raster scanning a single focal optical spot. This resulted in near-field tip scattering techniques [43–47] outperforming the technique of ref. [67].

1.4 This thesis

This thesis performs near-field THz imaging with a single-element detector. This is achieved by the placing our THz spatial modulator, a silicon wafer pumped with optical light, in the near-field of the object to be imaged. We demonstrate sub-wavelength spatial resolution ($9\mu m \sim \lambda/45$ at $0.75THz$) whilst been able to under-sample our images (we measure down to 35% the number of measurements as the number of pixels). Under-sampling at sub-wavelength resolutions is yet to be experimentally demonstrated even in the visible regime. Further more, we have a hyperspectral

detector with which we are able to extract the near-field permittivity of a sample (see ch. 8). Whilst certainly impressive, our technique is very slow with the acquisition of a single image taking hours. The reason for this slow acquisition rate is that we use a high-power low-repetition rate laser system[1]. We use this high-powered laser because in order to achieve good THz modulation one has to photoexcite a silicon wafer with a lot of power. The need for this large pump power is the biggest drawback to our technique. A smaller drawback that needs to be mentioned is that this is a complicated setup requiring the temporal synchronization and the spatial alignment of three beams: a THz beam, an optical pump and a detection probe pulse.

[1]The laser system had a 1050Hz repetition rate with 3mJ energy per pulse (duration 100fs).

Chapter 2

Background Electromagnetic theory

2.1 THz interaction with matter

This entire work lays its foundations upon Maxwell's macroscopic equations:

$$\nabla \cdot \mathbf{D} = \rho_f, \qquad (2.1)$$

$$\nabla \cdot \mathbf{B} = 0, \qquad (2.2)$$

$$\nabla \times \mathbf{E} = -\frac{\partial \mathbf{B}}{\partial t}, \qquad (2.3)$$

$$\nabla \times \mathbf{H} = \frac{\partial \mathbf{D}}{\partial t} + \mathbf{J}_f, \qquad (2.4)$$

where ρ_f and $\mathbf{J}_f$ are respectively the free charge and current densities within some space. The macroscopic fields $\mathbf{D}$ and $\mathbf{H}$ are defined as

$$\mathbf{D} \equiv \epsilon_0 \mathbf{E} + \mathbf{P} = \epsilon \mathbf{E}, \qquad (2.5)$$

$$\mathbf{H} \equiv \frac{1}{\mu_0}\mathbf{B} - \mathbf{M} = \frac{1}{\mu}\mathbf{B}, \qquad (2.6)$$

where ϵ_0 and μ_0 are respectively the permittivity and permeability of free space with ϵ and μ being the electric permittivity and the magnetic permeability of a material, respectively. The polarization $\mathbf{P}$ and magnetization $\mathbf{M}$ hold the macroscopic information regarding the properties of the medium in mind.

2.1.0.1 Boundary Conditions at a surface discontinuity

The above equations are stated for regions of space where there is no discontinuity in the material properties of the medium. However, objects exist causing abrupt changes in the material properties needed to describe the scene in mind. These changes impose boundary conditions to the electric and magnetic fields across the surface of such discontinuities. These boundary conditions are only stated here due to their immense importance in all electro-magnetic phenomena and for the sake of completeness;

$$\mathbf{n}_{12} \cdot (\mathbf{B}^{(2)} - \mathbf{B}^{(1)}) = 0, \tag{2.7}$$

$$\mathbf{n}_{12} \cdot (\mathbf{D}^{(2)} - \mathbf{D}^{(1)}) = \rho_s, \tag{2.8}$$

$$\mathbf{n}_{12} \times (\mathbf{H}^{(2)} - \mathbf{H}^{(1)}) = \mathbf{j}_s, \tag{2.9}$$

$$\mathbf{n}_{12} \times (\mathbf{E}^{(2)} - \mathbf{E}^{(1)}) = 0, \tag{2.10}$$

where ρ_s and $\mathbf{j}_s$ are respectively the surface charge and current densities across the discontinuity and $\mathbf{n}_{12}$ is the vector normal to the surface. In words, these boundary conditions can be stated as: *The normal component to the magnetic induction and the tangential electric field are both continuous across the discontinuity, and the normal electric displacement and tangential magnetic fields change abruptly with their discontinuities respectively equaling* ρ_s *and* $\mathbf{j}_s \times \mathbf{n}_{12}$. A full derivation of these boundary conditions can be found in chapter 1.1.3 of ref. [68].

2.1.1 Wave equation and Fabry-Perot

From Maxwell's equations, we next obtain the wave equation for the electric field. This is accomplished by putting eqs. (2.4), (2.5) & (2.6) into the curl of eq. (2.3) and simplifying with the vector identity $\nabla \times (\nabla \times \mathbf{A}) = \nabla(\nabla \cdot \mathbf{A}) - \nabla^2 \mathbf{A}$;

$$\nabla^2 \mathbf{E} - \epsilon\mu \frac{\partial^2 \mathbf{E}}{\partial t^2} = \mu \frac{\partial \mathbf{J}_f}{\partial t} + \frac{1}{\epsilon} \nabla \rho_f. \tag{2.11}$$

Further simplifications are made with Ohm's law $\mathbf{J}_f = \sigma \mathbf{E}$ and neglecting charge density fluctuations, ie. $\nabla \rho_f = 0$, to then obtain

$$\nabla^2 \mathbf{E} - \epsilon\mu \frac{\partial^2 \mathbf{E}}{\partial t^2} = \sigma\mu \frac{\partial \mathbf{E}}{\partial t}, \tag{2.12}$$

where σ is the electrical conductivity. An identical wave equation is obtained is for $\mathbf{H}$ in an identical manner. In the case of free space propagation, $\sigma = 0,\ \epsilon = \epsilon_0,\ \mu = \mu_0$, one obtains $c = 1/\sqrt{\epsilon_0\mu_0}$ as the speed at which an electromagnetic wave moves through a vacuum. In other words c is the speed of light. However, should $\sigma = 0$, $\epsilon \neq \epsilon_0$ and $\mu \neq \mu_0$ then the wave propagates with speed $v = c/n$ where n is the refractive index of the material given by $n^2 = \frac{\epsilon\mu}{\epsilon_0\mu_0}$.

Having an equation only sets up the problem and does not yield insight or information regarding the observable world. For this reason, we look for solutions to the wave equation that are expressed as linearly polarized, monochromatic, plane waves traveling in the z-direction with wave-vector $\mathbf{k} = k_z\hat{\mathbf{z}}$, ie:

$$\mathbf{E}(\mathbf{r}, t) = \mathbf{E}_0 e^{i(k_z z - \omega t)}. \tag{2.13}$$

Putting this equation into eq. (2.12) yields the following dispersion relation

$$k_z^2 = \omega\mu(\epsilon\omega + i\sigma). \tag{2.14}$$

This relationship determines how a wave propagates in a medium with specific electromagnetic properties ϵ, μ, σ. In the case of a dielectric or an insulator $\sigma \simeq 0$ hence k_z is purely real. Then the wave propagates as

$$\mathbf{E}(\mathbf{r}, t) = \mathbf{E}_0 e^{i(\omega\sqrt{\mu\epsilon}z - \omega t)} \tag{2.15}$$

and experiences no decay provided μ and ϵ are both positive and real. In a conductor, however, the conductivity is very large such that $\sigma \gg \epsilon\omega$ thus $k^2 \approx i\omega\mu\sigma$. Evidently

$$k = k_r + ik_i \approx \sqrt{\frac{\omega\mu\sigma}{2}}(1 + i), \tag{2.16}$$

where k_r and k_i are the real and imaginary parts of the k vector. In this case the EM wave propagates as

$$\mathbf{E}(\mathbf{r}, t) = \mathbf{E}_0 e^{i(\omega\mu\sigma z/2 - \omega t)} e^{-z/d}, \tag{2.17}$$

where $d = \sqrt{\frac{2}{\omega\mu\sigma}}$ is known as the attenuation length or skin depth. This value indicates how far the wave will penetrate before being attenuated.

2.1.1.1 Reflections at Boundaries

We now have a plane wave as a simple solution to our wave equation. If we input this into $\nabla \cdot \mathbf{E} = 0$ and $\nabla \cdot \mathbf{H} = 0$ we observe the following relation

$$\mathbf{k} \cdot \mathbf{E} = \mathbf{k} \cdot \mathbf{H} = 0. \tag{2.18}$$

This relationship implies that $\mathbf{E}$ and $\mathbf{H}$ are both perpendicular to the direction of travel, hence EM waves are transverse. A consequence of this is that if one considers transmission through an interface between two media of different refractive indices, then the wave can be polarized perpendicular or parallel in regards to the plane incidence (Figure 2.1). This consequence combined with the continuity boundary conditions at the surface, in §2.1.0.1, implies that you get different reflection and transmission coefficients depending on how your incident light is polarized. This fact

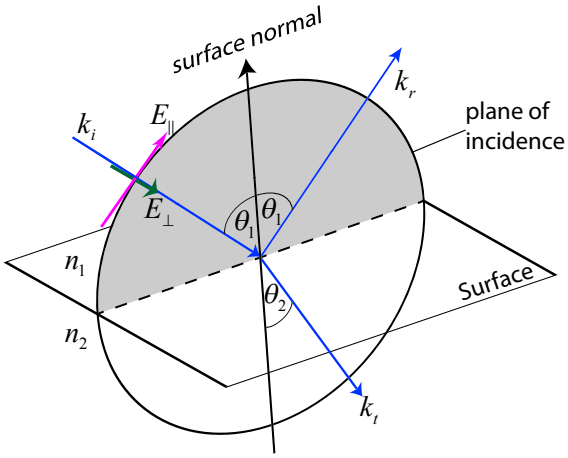

Figure 2.1: Reflection and transmission of a plane wave at a surface between two mediums with different refractive indices. Shown are the incident, reflected and transmitted k vectors in blue, and shown with the pink and green arrows is wave polarization parallel and perpendicular to the plane of incidence respectively.

when combined with Snell's law of refraction

$$n_1 \sin\theta_1 = n_2 \sin\theta_2, \tag{2.19}$$

where $n_{1,2}$ are the refractive indices of the two mediums and $\theta_{1,2}$ are the angles of incidence and refraction, yields the famous Fresnel amplitude reflection and transmission coefficients:

$$r_{\parallel} = \frac{n_2 \cos\theta_1 - n_1 \cos\theta_2}{n_1 \cos\theta_1 + n_2 \cos\theta_2}, \qquad (2.20) \qquad r_{\perp} = \frac{n_1 \cos\theta_1 - n_2 \cos\theta_2}{n_1 \cos\theta_1 + n_2 \cos\theta_2}, \qquad (2.22)$$

$$t_{\parallel} = \frac{2n_1 \cos\theta_1}{n_1 \cos\theta_1 + n_2 \cos\theta_2}, \qquad (2.21) \qquad t_{\perp} = \frac{2n_1 \cos\theta_1}{n_1 \cos\theta_1 + n_2 \cos\theta_2}. \qquad (2.23)$$

Furthermore one defines the Reflectivity and Transmissivity as $R = |r|^2$ and $T = n_2|t|^2/n_1$.

2.1.1.2 Fabry-Perot Interference

The above consideration would hold absolutely true if our world was made from solely two materials. Obviously untrue, hence the next step of extending our mathematical model of the world is to consider the scenario when the second material is of a finite thickness L. When a plane arrives at the incident interface it will split into a reflected and a transmitted component. Then, the transmitted part will come up against the second exit interface and split again. The consequential reflected component will split again at the other interface. This process will carry on going indefinitely. Further, every time the wave travels through the dielectric it will pick up a phase shift, between each preceding member of the set of reflected or transmitted waves, of

$$\phi = \frac{2\pi f}{c} L n_2 \cos\theta_2, \qquad (2.24)$$

where f is the frequency of the wave. A *Fabry-Perot resonance* is defined as when all the components resulting from each individual splitting of the wave interfere constructively. Now, if one considers the superposition of all these waves then the total transmitted field E_t is given by

$$\begin{aligned} E_t &= E_i t_1 t_2 e^{i\phi}(1 + r_1 r_2 e^{2i\phi} + r_1^2 r_2^2 e^{4i\phi} + ... \\ &= E_i t_1 t_2 e^{i\phi} \sum_{n=0}^{\infty} (r_1 r_2 e^{2i\phi})^n \\ &= E_i \frac{t_1 t_2 e^{i\phi}}{1 - r_1 r_2 e^{2i\phi}}, \end{aligned} \qquad (2.25)$$

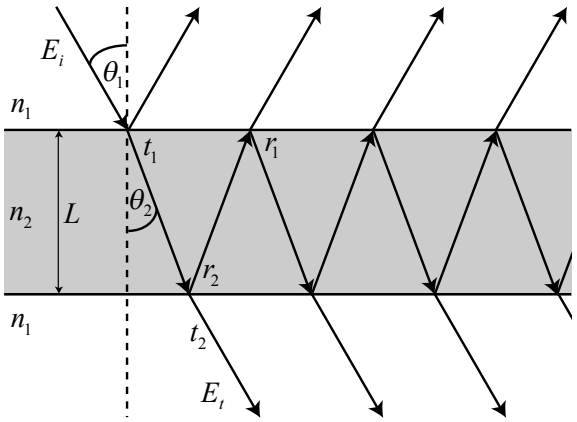

Figure 2.2: Reflection and transmission of a plane wave undergoing multiple reflections within a dialectic.

where $t_1,\ t_2,\ r_1,\ r_2$ are the relevant Fresnel coefficients in fig. 2.2. A more detailed derivation is given in ch. 7.6.1 of ref. [68] along with the equation for reflection;

$$E_r = -\frac{r_2(1-(r_2^2+t_1t_2)e^{2i\phi}}{1-r_2^2e^{2i\phi}}E_i. \tag{2.26}$$

These two equations (2.25) & (2.26) do need to be considered if one wishes to do a reflection or transmission experiment through any material. In THz measurements they are also used to extract permittivity of an unknown material, as outlined in §3.2.1.

2.1.2 Fundamental models of matter

So far, the previous sub-sections have assumed that the materials properties, ϵ, μ and σ, do not change with the frequency of the EM wave. This is false for all materials in an absolute sense, however for certain frequency ranges this can be approximately true and such materials are called dispersion-less. However, most materials do change with frequency since everything contains atoms and electrons which interact with an incident EM wave.

2.1.2.1 Classical Lorentzian

For an improved mathematical description of the world the classical Lorentzian model was developed. It accounts for the response of charged and bound particles to an

incident EM wave. Here, one assumes that a bound charge oscillates about its equilibrium position and thus has a potential energy given by a simple harmonic oscillator of frequency ω_0 and mass m:

$$U(x) = \frac{1}{2} m\omega_0^2 x^2. \tag{2.27}$$

Then the charged particle will experience a restoring force F_r from $\mathbf{F} = -\nabla U$. Further more, there will be a damping term F_d and a force from the incident electric field F_E. Combining these forces into Newton's second law gives;

$$\begin{aligned} m\frac{d^2x}{dt^2} &= F_r + F_d + F_E \\ &= -m\omega_0^2 x - m\gamma\frac{dx}{dt} + qE, \end{aligned} \tag{2.28}$$

where γ is the phenomelogical damping rate and q is the charge of the charged particle. If we say that we have a scalar monochromatic linearly polarized EM wave, ie. it is of the form of eq. (2.13), then the solution to eq. (2.28) is given by

$$x(t) = \frac{qE_0 e^{-i\omega t}}{m(\omega_0^2 - \omega^2 - i\gamma\omega)}. \tag{2.29}$$

Now one knows the electric dipole moment per charged harmonic oscillator $p(t) = qx(t)$. Hence, for a medium with N oscillators per unit volume we have an electric polarization of

$$P(t) = Nqx(t) = \frac{Nq^2 E_0 e^{-i\omega t}}{m(\omega_0^2 - \omega^2 - i\gamma\omega)} \equiv \epsilon_0 \chi(\omega) E_0 e^{-i\omega t}, \tag{2.30}$$

where $\chi(\omega)$ is the linear susceptibility of the medium. Now if we consider eqs. (2.5) and (2.30) we can define the relative permittivity of our medium

$$\epsilon_r(\omega) \equiv \frac{\epsilon(\omega)}{\epsilon_0} = 1 + \chi(\omega) = 1 + \frac{Nq^2}{m\epsilon_0(\omega_0^2 - \omega^2 - i\gamma\omega)} \tag{2.31}$$

with real and imaginary parts $\epsilon_r = \epsilon_r' + i\epsilon_r''$, given by

$$\epsilon_r' = \frac{Nq^2(\omega_0^2 - \omega^2)}{m\epsilon_0((\omega_0^2 - \omega^2) + \omega^2\gamma^2)} \tag{2.32}$$

$$\epsilon_r'' = \frac{Nq^2\omega\gamma}{m\epsilon_0((\omega_0^2 - \omega^2) + \omega^2\gamma^2)} \tag{2.33}$$

In terahertz this model is most often used to account for the absorption caused by crystal lattice vibrations.

2.1.2.2 Drude model

In the section above the charged particle is bound in space, however the scenario of it being free to move about in space is also possible. To account for such a response the Drude model was developed. Its assumptions are that we have a sea of mobile electrons and a set of stationary positively charged ions constituting our medium. The mobile electrons freely move in only straight lines unaffected by any other forces except those in the instantaneous (assumed to be so) collisions with the impenetrable ion cores (electron-electron collisions conserve momentum hence no change to the current). The electrons collide with the ion cores on average after time τ. This is the only mechanism by which they reach thermal equilibrium, hence we assume that each collision randomizes the velocity with a speed appropriate to the local thermal conditions.

With the above assumptions we can find the DC electrical conductivity of a material. This is done by considering the current density created from N electrons per unit volume moving through a surface area perpendicular to velocity of the electrons $\mathbf{v}$. The charge carried by each electrons is $-e$, hence the current density is simply

$$\mathbf{J} = -Ne\mathbf{v}. \tag{2.34}$$

Now, if we apply an electric field $\mathbf{E}$ then after time t an electron's velocity will be $\mathbf{v} = \mathbf{v}_0 - e\mathbf{E}t/m$, where $\mathbf{v}_0$ is the electron's velocity after its previous collision. Due to the velocity randomization through each collision $\mathbf{v}_0$ averages out to zero. Since each collision occurs on average after time τ, we have

$$\mathbf{v}_{avg} = -\frac{e\mathbf{E}\tau}{m}; \qquad \mathbf{J} = \frac{Ne^2\tau}{m}\mathbf{E}, \tag{2.35}$$

where $\mathbf{v}_{avg}$ is known as the electron drift velocity. From Ohm's law we can see that

the DC conducivity, σ_0, of a metal is

$$\mathbf{J} = \sigma_0 \mathbf{E}; \qquad \sigma_0 = \frac{Ne^2\tau}{m}. \tag{2.36}$$

In practice we don't know τ but by measuring the conductivity we can estimate values for it.

With the above assumptions, the Drude response of a medium to a monochromatic wave can be characterized by that of a Classical Lorentzian oscillator centered at zero frequency and a damping rate equal to the probability of collision per unit time, ie. $\omega_0 = 0$ and $\gamma = 1/\tau$ in eq. (2.29). However, we are interested in the velocity not position so we can use eq. (2.34) to obtain

$$\sigma(\omega) = \frac{Ne^2\tau}{m(1 - i\omega\tau)} = \frac{\sigma_0}{1 - i\omega\tau} \tag{2.37}$$

as the AC conductivity of our material. Now, if we turn our attention to the wave equation (2.12) describing our EM wave and say $\mu = \mu_0$, we can see that it can written in the form

$$\nabla^2 \mathbf{E} = -\omega^2 \mu_0 \left(\epsilon + \frac{i\sigma_0}{\omega(1 - i\omega\tau)} \right) \mathbf{E}. \tag{2.38}$$

This yields the following dispersion relation for our monochromatic wave;

$$k_z^2 = \omega^2 \mu_0 \epsilon_0 \epsilon(\omega); \qquad \epsilon(\omega) = \epsilon_\infty + \frac{i\sigma_0}{\epsilon_0 \omega(1 - i\omega\tau)}, \tag{2.39}$$

where ϵ_∞ is the frequency independent dielectric permittivity due to the contribution of bound charges and $\epsilon(\omega)$ is known as the Drude permittivity.

If we now consider the case of $\omega\tau >> 1$ we can see that our Drude permittivity approximates to

$$\epsilon(\omega) = \epsilon_\infty - \frac{Ne^2}{m\epsilon_0\omega^2} = \epsilon_\infty - \frac{\omega_p^2}{\omega^2}, \tag{2.40}$$

where $\omega_p = \sqrt{Ne^2/m\epsilon_0}$ is known as the plasma frequency of the material. Since $k_z \propto \sqrt{\epsilon(\omega)}$ then when $\omega^2\epsilon_\infty > \omega_p^2$ we have a purely real dispersion relation thus the wave propagates inside the material. For $\omega^2\epsilon_\infty < \omega_p^2$ we have a purely imaginary k_z signifying that the waves decay inside the material at the rate given by $k_i(\omega) = \frac{1}{c}\sqrt{\omega_p^2 - \epsilon_\infty\omega^2}$.

2.1.2.3 Quantum Models of Charge carriers

The Free-Electron model was developed to better understand solids and the conduction of electrons through metals. It considers the valence electrons of a material and makes similar assumptions to the Drude model along with taking into account Quantum theory and Pauli's exclusion principle. This model gives insight into the thermal and electrical conductivity, heat capacity and electrodynamics of metals. However, it fails to point out the distinction between metals, semiconductors and insulators. To understand this distinction the Nearly Free-Electron model was developed.

The Nearly Free-Electron model makes a step further by taking into account how the conducting electrons experience a potential energy variation due to the lattice arrangement of the positive ion cores within a crystal. This model gives intuitive insight into the observed band structure of solid matter, in other words why there exist electrons with momentum values which do not propagate through the crystal. This is done by considering the Bragg reflection condition within the first Brillouin zone of the crystal lattice in mind; one sees that two different standing waves can be set up from the periodicity of the lattice. One piles up electrons on top of the positive ions and the other in between the ion cores. Due to the attractive forces between the negative electrons and positive cores, the first wave has a lower total energy. The difference in two energies is known as the energy gap, E_g.

The size of the energy gap between the conduction and valance electron bands determines whether a material is a metal, a semiconductor or an insulator as follows; metals have no energy gap hence there is always filled states in the conduction band, semiconductors have a small gap thus it is easy to excite electrons into a conducting state and insulators have a large energy gap hence a lot of energy is required to force electrons to become conducting (shown in Fig. 2.3). Another important feature to consider here is when an electron is excited into the conduction band a vacant orbital is left in the valance band, which is referred to a hole. Holes act though as they are an electron with positive $+e$ charge and mass $m_h = -m_e$ in applied electric and magnetic fields. In other words, they contribute to the overall current within our material. Thus, they are considered as charge carriers along with the electrons. Both these charge carriers do not behave like their counterparts in free-space. To account for this a theoretical simplification is made by saying electrons and holes behave like free-space particles with an effective mass m^*.

Next, we define the charge carrier mobility as the magnitude of its drift velocity

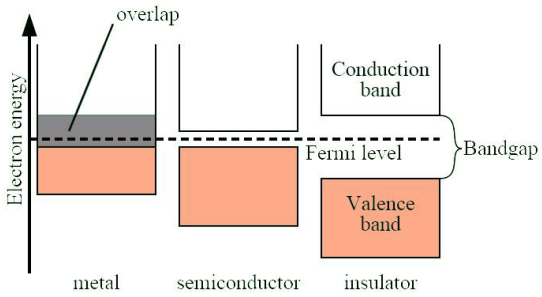

Figure 2.3: Band structures of metals, semiconductors and insulators. The Fermi level shows where the electron states are filled up to. Taken from hyperphysics

per unit electric field, ie $\mu = |\mathbf{v}_{avg}|/E$ or $\mu = q\tau/m^*$ from consideration of eq. (2.35) [69]. Then the electrical conductivity of our medium is

$$\sigma = N_e e\mu_e + N_h e\mu_h, \tag{2.41}$$

where μ_e & μ_h are the electron and hole mobilities respectively. Further, the conduction electrons and holes will diffuse according to the 3D diffusion equation. Hence, their mean square displacement is

$$< x^2 >= 6Dt, \tag{2.42}$$

where D is the diffusion coefficient given by the Einstein-Smoluchowski relation, $D = \mu_q k_B T/q$ where μ_q is the mobility of the charge carrier given earlier in this paragraph.

2.1.3 Material properties at THz

2.1.3.1 Conductors

The terahertz response to highly conductive mediums such as metals is well accounted for by the Drude model. The typical relaxation times of metals are on the order of 10^{-14}s implying that $\omega\tau << 1$. This reduces $\sigma(\omega)$ and $\epsilon(\omega)$ in eqs. (2.39) and (2.37) respectively down to $\sigma(\omega) = \sigma_0$ and $\epsilon(\omega) \approx i\sigma_0/(\epsilon_0\omega)$. This yields a reflectivity of $R(\omega) \approx 1 - \sqrt{8\epsilon_0\omega/\sigma_0}$. In the end, typical metals with conductivities on the order of 10^7 S.m^{-1} have a penetration depth of 400 nm and a reflectivity of 98-99%, table 2.1 show reflection values of common metals. Metals are used as THz reflectors.

Table 2.1: THz reflectivity of metals, uncertainty $\pm 0.1\%$. From [70].

Metals	R at 0.58THz	R at 2.55THz
Copper	0.997	1
Silver	0.996	0.995
Gold	0.994	0.994
Aluminium	0.995	0.994
Nickel	0.994	0.991
Chromium	0.993	0.974

In regards to THz applications, transparent conductors such as tin doped indium oxide (ITO) are very interesting. The visible light transmittance of ITO is reported to be around 90%. Its conductivity is on the order of 10^6 S.m^{-1} yielding a reflectivity of 98% at 1 THz. This allows for the creation of a THz reflector that transmits an optical beam.

2.1.3.2 Glass and polymers

Ordinary glasses exhibit high losses due to charged defects at THz and thus are not used as optical elements. Much more transmissive materials include polymers, dielectrics and semiconductors. Polymers give on average an absorption coefficients around 0.4 cm^{-1} at 1 THz [71] and typical refractive indices of around 1.5 [72]. Due to their refractive indices polymers can be used as THz lenses, however their absorption coefficients increase with frequency as shown by Fig. 2.4. A mention goes to Tsurupica, a highly transparent polymer for both THz and visible light with a refractive index of 1.52 for both bands.

2.1.3.3 Semiconductors

Silicon is probably going to be one of the most crucial materials for device development at Terahertz frequencies; the reasons are because it's very transmissive, nearly dispersionless and there is an advanced Silicon manufacturing industry which supplies highly quality cheap Silicon quickly, a feature useful for any realistic experimentalist. Further more there is a rich literature regarding its mechanical and electrical properties.

Silicon refractive index was measured to be 3.4175 and to vary by ± 0.0001 over the frequency range of 0.5-4.5 THz. Its absorption coefficient was measured to be

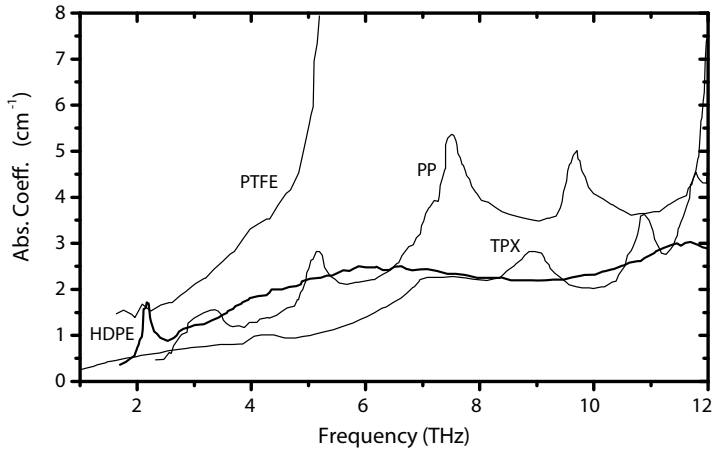

Figure 2.4: Absorption coefficients of some polymers versus frequency in the range of 2-12 THz. Polymers shown are: High-density polyethylene (HDPE), Teflon (PTFE), Polypropylene (PP) and Polymethylpentene (TPX). Figure from [71].

0.04 cm^{-1} at 1 THz [73]. Silicon is commonly used in THz lenses. An extra point, the plasma frequency of highly resistive Silicon lies below the terahertz regime. However, by modulation of free charge carrier concentration one can switch the material response from dielectric to conductor (see §3.3).

One way of controlling the carrier density is via optical excitation with photons of energy $\hbar\omega$, further discussed in §3.3. Reference [74] was the first to demonstrate amplitude, phase and frequency modulation of THz via the optical excitation of silicon. More recently, people have built upon these ideas to create an optically modulated wire-grid polarizer [75] and to image objects by creating an imaging mask [61] in Silicon. There are other materials which have similar properties such as InSb and GaAs.

2.2 Image theory and Fourier Optics

When light impinges upon an object it is scattered from it in all directions. Then, how this scattered light reaches our eyes, or an external detector, is the prime concern of imaging theory. Rephrased in modern terms, how is a set of EM-field disturbances at point A related to a set at point B. Below is an overview of the theories used for modeling in this thesis.

2.2.1 Scalar diffraction theory

Although light is a vectorial wave, many initial imaging experiments showed remarkable agreeance with scalar diffraction theories. In other words, the Cartesian components of an EM-field are not coupled together, by Maxwells eqs. (2.1-2.4), but the behavior of each individual component is summarized by a single scalar wave equation [76]

$$\nabla^2 U(p,t) - \frac{n^2}{c^2}\frac{\partial^2 U(p,t)}{\partial t^2} = 0, \tag{2.43}$$

where $U(p,t)$ represents the scalar field components at position p and time t. Now one needs to impose some boundary conditions describing the object in mind. After solving the resulting equation one can calculate how the field distribution at the object will propagate to any point of observation. However, different theories make various assumptions to obtain a solution.

Next, we follow the work of ref. [77]. Therein, by assuming a monochromatic wave and that all scatterers, sources and diffracting apertures are located in negative z-space Kowarz obtains a solution to eq. (2.43) for positive z-space. His expression for the electric field $U(x,z)$ is the sum of two parts, a homogeneous propagating field $U_h(x,z)$ and an evanescent field $U_i(x,z)$:

$$U_h(x,z) = \int_{|u_x|\leq 1} A(u_x) e^{iku_x x} e^{ikz\sqrt{1-u_x^2}} \mathrm{d}u_x, \tag{2.44}$$

$$U_i(x,z) = \int_{|u_x|\geq 1} A(u_x) e^{iku_x x} e^{-kz\sqrt{u_x^2-1}} \mathrm{d}u_x, \tag{2.45}$$

where u_x is the directional wavevector, k is the free space wavenumber in x and $A(u_x)$ is a spectral amplitude function that is the Fourier transform of the scatterer's field distribution in the plane $z = 0$, ie.

$$A(u_x) = \frac{k}{2\pi}\int_{-\infty}^{\infty} U(x,0) e^{-iku_x x} \mathrm{d}x. \tag{2.46}$$

From the above three equations one can calculate the diffraction of a field distribution $U(x,0)$ at any plane in positive z space. Note, the intensity is defined as $I(x,z) \equiv |U(x,z)|^2 = |U_h(x,z) + U_i(x,z)|^2$.

A technical note, in our experiments we have multiple frequencies. To account for this, we sum the diffracted fields for all our frequencies, where each frequency

component has an input amplitude given by our pulse spectrum (fig. 3.1**B**) and a silicon equivalent wavelength. Finally, for ch. 5 we extend this theory to two dimensions by considering the 2D Fourier transform of eq. 2.46 and adding an extra integral over u_y[1] in eqs. 2.44 & 2.45.

2.2.2 Vectorial modal matching theory

It is always of preference to use simpler mathematical models to describe the world. However, these usually come with assumptions and restrictions rendering them unusable in certain scenarios. Namely, polarization effects are neglected by the scalar diffraction approximation in the above section. For this reason, next follows an outline of a full wave modal matching solution to Maxwell's equations. Note that this theory was used in Ch. 4 and 8, however the method is outlined using the simpler equations of Ch. 8.

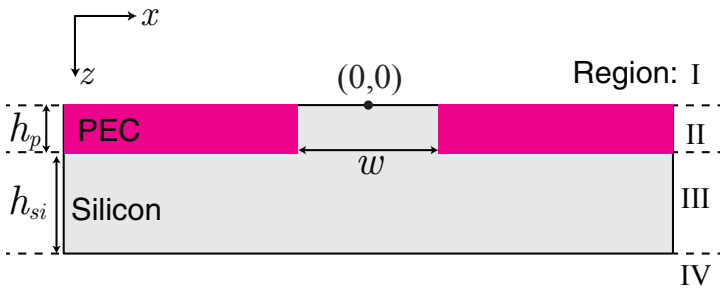

Figure 2.5: Schematic showing the variable definitions used in the modal matching calculations of Sec. 2.2.2. $h_p = 11\mu m$ is the penetration depth of our 800nm pump light [78], $h_{si} = 104\mu m$ is the thickness of our silicon wafer minus h_p. PEC stands for perfect electrical conductor.

The time dependent components of the fields ($e^{i\omega t}$) have been omitted for clarity. We begin by sectioning our system into four regions along the z-axis direction, shown by Fig. 2.5. Region I extends to the half space on the incident side of our system. Using the angular spectrum representation [76, 77] we have a normally incident plane wave and a reflected component that is a superposition of plane waves propagating away from the sample, written

$$E_{1x} = e^{ik_{1,z}(0)z} + \int_{-\infty}^{\infty} A_r(v_x) e^{-ik_{1,z}(v_x)z} e^{iv_x x} \mathrm{d}v_x, \tag{2.47}$$

[1]Note the square root terms become $\sqrt{1-u_x^2-u_y^2}$ and there is an extra $e^{iku_y y}$ term.

where v_x is the directional wavevector in x, $A_r(v_x)$ is a spectral amplitude function and $k_{1,z}(v_x) = \sqrt{(n_1 k_0)^2 - v_x^2}$. In the region II we have a perfectly conducting film with single slit of some refractive index, where the infinite conductivity approximation simplifies boundary conditions. Our fields are represented by the modes of a cavity. For simplicity, we choose polarization perpendicular to our cavity, thus the electric field parallel to the interfaces of the conducting sections will be zero. Boundary conditions will thus dictate that the fundamental mode of our cavity is described by a rectangle function. This is written

$$E_{2x} = \left(G_1 e^{ib_z z} - G_2 e^{-ib_z z}\right) \text{rect}\left(\frac{x}{w}\right) \tag{2.48}$$

where $b_z = n_2 k_0$ is the wave vector inside the cavity, w is width of cavity. In region III, containing an arbitrary dielectric, we have two sets of wave superpositions, each travelling in opposite z directions, written

$$E_{3x} = \int_{-\infty}^{\infty} F_1(v_x) e^{ik_{3,z}(v_x)z} e^{iv_x x} \mathrm{d}v_x - \int_{-\infty}^{\infty} F_2(v_x) e^{-ik_{3,z}(v_x)z} e^{iv_x x} \mathrm{d}v_x, \tag{2.49}$$

where $k_{3,z}(v_x) = \sqrt{(n_3 k_0)^2 - v_x^2}$. Finally, in region IV we have a transmitted component that is a superposition of plane waves propagating away from the sample in the positive z direction:

$$E_{4x} = \int_{-\infty}^{\infty} A_t(v_x) e^{ik_{4,z}(v_x)z} e^{iv_x x} \mathrm{d}v_x, \tag{2.50}$$

where $k_{4,z}(v_x) = \sqrt{(n_4 k_0)^2 - v_x^2}$. All E_y components are zero due to our choice of geometry and incident polarization. From the free space Maxwell's equations $\nabla \cdot \mathbf{E} = 0$ and $\nabla \times \mathbf{E} = -\mu_0 \partial \mathbf{H}/\partial t$ we obtain the z electric field components, and also the subsequent expressions for the magnetic $\mathbf{H}$-fields.

We now have the electric and magnetic components in all regions of space in terms of six unknow functions $A_r(v_x)$, $G_{1,2}$, $F_{1,2}(v_x)$ and $A_t(v_x)$. We solve for these by applying boundary conditions: the electric fields must be continuous for all x space at the interfaces between adjacent regions, while the magnetic fields are continuous only over our defined apertures [79, 80]. Hence, for the interface between regions I and II at $z = 0$ we end up with $E_{1x} = E_{2x}$ for the electric and $H_{1y} = H_{2y}$ for the magnetic continuity equations. Substituting eqs. (2.47) and (2.48) into the E-field

continuity equation for the interface at $z = 0$, and taking its Fourier transform[1], we end up with

$$\delta(v_x) + A_r(v_x) = (G_1 - G_2)\, Q(v_x) \tag{2.51}$$

where $\delta(v_x)$ is the delta function and $Q(v_x)$ is the Fourier transform of the rect function, ie.

$$Q(v_x) = \frac{1}{2\pi} \int_{-\infty}^{\infty} \text{rect}\left(\frac{x}{w}\right) e^{-iv_x x} \mathrm{d}x. \tag{2.52}$$

The H-field continuity equation at the same interface, $z = 0$, gives

$$k_z(0) - \int_{-\infty}^{\infty} A_r(v_x) e^{iv_x x} O(v_x) \mathrm{d}v_x = q_z\, (G_1 + G_2)\, \text{rect}\left(\frac{x}{w}\right) \tag{2.53}$$

where $O(v_x) = \frac{v_x^2 + k_{1,z}(v_x)^2}{k_{1,z}(v_x)}$ in eq. (2.53). We now substitute $A_r(v_x)$ from (2.51) into (2.53) and integrate the resulting equation over the values of x for which the magnetic continuity equations hold (the non-conducting regions), obtaining

$$k_z(0)w - \int_{-\infty}^{\infty} \Big((G_1 - G_2)\, Q(v_x) - \delta(v_x) \Big) I_h(v_x) A(v_x) \mathrm{d}v_x \;=\; q_z\, (G_1 + G_2)\, w, \tag{2.54}$$

where

$$I_h(v_x) = \int_{-w/2}^{w/2} e^{iv_x x} \mathrm{d}x. \tag{2.55}$$

Notice that the field amplitudes in the cavities in region II do not depend on the directional wavevector v_x and thus can be taken out of the integral in eq. (2.54). A similar consideration of the remaining interfaces between the regions is carried out; in the end we obtain six simultaneous equations which are solved for all six amplitude coefficient functions via matrix methods. We can now plot the electric & magnetic fields in any region of space for any choice of parameters $(w, \lambda, n_3, ...)$. In doing so, we must numerically evaluate the overlap integrals resulting from these mathematical manipulations. For example, the integral

$$\int_{-\infty}^{\infty} I_h(v_x) O(v_x) Q(v_x) \mathrm{d}v_x \tag{2.56}$$

[1]The Fourier transform is allowed since the E-fields are continuous for all x and the integration equates the fields for all x. However, a Fourier transform of a the H-fields is not possible since they are not continuous for all x space.

arising from eq. (2.54) is numerically evaluated using a Riemann sum over the interval [-125 000, 125 000]m^{-1} with 350 sampling points, each evaluated at the midpoint of the respective subintervals between the sampling points. Note that numerical instabilities were encountered when $v_x = n_1 k_0$ since $O(v_x)$ diverges to infinity at this point. These instabilities were solved by excluding the values around these poles[1]. The full mathematical workings as performed with Wolfram Mathematica is given in the appendix.

Use of Model

Our main use for the model in the section 2.2.2 is to investigate the validity of the permittivity extraction procedure of chapter 3.2.1. Briefly, this procedure involves solving the Fresnel equations for the transmission through our multilayer system with and without the sample. This is emulated in our model by calculating the far-field transmitted component, i.e. (2.50) for $v_x = 0$, when $n_3 = \sqrt{7.5 + 2i}$ and again when $n_3 = 1$. In both cases we set $n_{1,4} = 1.58$ in order to take into account the effect of the plastic coverslips encapsulating our sample and $n_2 = 3.44$ to model our silicon photomodulator. In our experiments we use a multi-aperture approach, meaning that our final amplitudes result from the addition of fields due to different sized apertures and scatterers. This is also emulated in the model by calculating (2.50) for a discrete range of values of w and then carrying out a complex summation of these fields, i.e. $\sum_{w_i} E_{4x}(w_i)$. These fields are then processed in a manner similar to the experimentally measured fields, as described in §3.2.1, so as to extract a frequency dependent permittivity of the sample layer.

[1] To be sure that excluding the poles did not affect the output value, we used the various intergration algorithms built in to Wolfram Mathematica 9 to obtain consistent values between all these algorithms. The Riemann sum was chosen for the final evaluation due to its speed.

Chapter 3

Experimental

This chapter gives the experimental details behind this thesis. The work here combines two major fields, THz spectroscopy and compressed sensing. Whilst nothing new is presented in regards to each individual field, the novelty is the successful combination of the two. The first two sections summarize THz spectroscopy and the latter two describe how one can perform compressed sensing in a THz time-domain spectrometer.

3.1 THz Time domain spectrometer

The fundamental layout of the setup is shown in figure 3.1. In its essence, a beam of femtosecond optical pulses is split into three beams: generation, detection and excitation. The first is used to generate a picosecond THz pulse, through optical rectification in ZnTe as discussed in sec. 3.1.2.1, which then passes through the sample under investigation. Our THz beam is collimated and collected by 90° off-axis parabolic mirrors made from gold. The second beam is used to detect the time profile of the THz waveform. This is achieved by temporally overlapping the much longer THz pulse with the very short detection pulse. The difference in pulse durations allows one to discretely sample the terahertz temporal profile by varying the path lengths with an optical delay line (typical THz transient and detection pulse envelope shown in figure 3.2). The electric field amplitude is extracted via electro-optic sampling in a ZnTe crystal, discussed in sec. 3.1.2.2. These systems detect the amplitude and relative phase of the THz pulse. This allows for the extraction of a real and imaginary permittivity of a sample as discussed in sec. 3.2. The third beam is used

to photoexcite the sample. These three beams are what constitute a typical THZ-TDS system. However, additionally in our system, the excitation beam is spatially modulated via a digital micromirror device (DMD) and a lens so as to project any binary intensity pattern onto our sample. Further more, our DMD is synchronized to the main laser system. The reason for this is discussed in sec. 3.4.2.2.

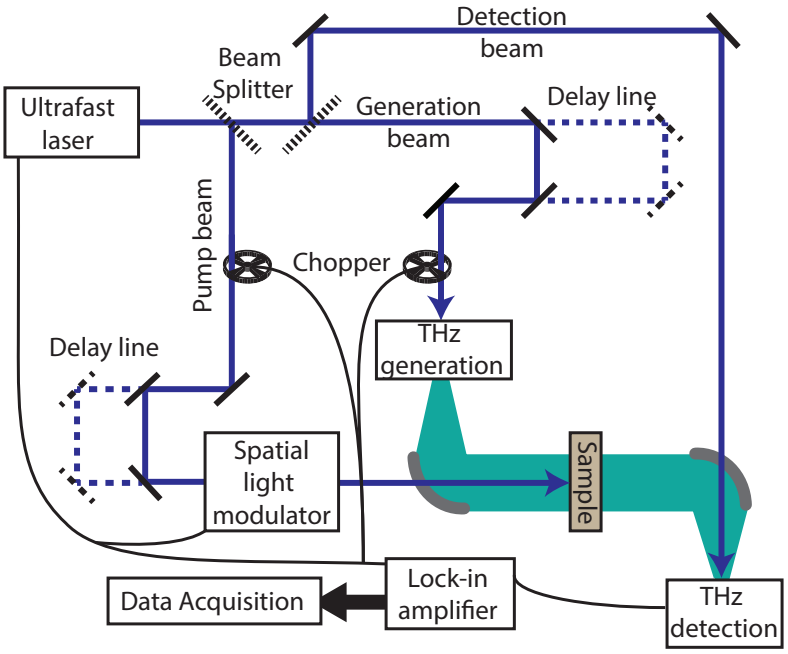

Figure 3.1: ***Schematic of time domain terahertz spectrometer.*** *A beam of ultrashort optical pulses leave an ultrafast laser. The beam is split into three beams: generation, detection and excitation. A chopper is placed in the detection or generation beams, depending on the needs of the experiment. A spatial light modulator, which can be synchronized to the ultrafast-laser, is placed in the excitation beam. Parabolic mirrors are used to collect and collimate the THz radiation.*

3.1.0.1 The ultra-fast laser source

The starting point of our THz-TDS is the laser powering the entire setup; a Ti:Sapphire system consisting of a seed laser and and regenerative amplification stage. Titanium-doped sapphire crystals have an absorption peak at $520nm$ and exhibit a gain over a large wavelength range, from $650nm$ to $1100nm$, with a maximum at $800nm$ (see ch. 3.1.2 of ref. [71]). Further, these crystals can withstand large optical pump power ($\sim 20W$). In our seed system, *Coherent Vitesse*, the Ti:Sapphire crystal is pumped

using a 535nm diode laser. The excited electrons within the crystal relax down to a lower state and emit photons with central wavelength 800nm. The continuous wave emission is converted in to pulses via a Kerr-lens modelocking mechanism. The emitted pulses have a duration of 85fs, 12nJ of energy per pulse and a repetition rate of 80MHz.

However, for the non-linear optical phenomena used to generate THz radiation in this thesis (§3.1.2.1) to be efficient, much bigger pulse energies are needed. Further more, most experiments here photoexcite a silicon wafer in order to modulate our THz pulse, see §3.3, which also requires large pulse energies. This is why we have a regenerative amplifier, *Coherent Legend Elite*, to increase the energy of the seed pulses although at lower the repetition rate. Before amplification, the seed pulses are temporally stretched using a reflection grating and collimating optics. This stretching stage lowers the instantaneous pulse intensity and thus avoids damaging the energy amplification optics at later stages. The regenerative amplifier is another Ti:Sapphire laser cavity that is optically isolated from the seed laser. The gain medium is pumped with its own diode laser until it has sufficient amounts of energy to be used an amplifier for the seed pulses. Unfortunately, this waiting stage results in throwing away many of the pulses from the seed laser. The seed pulses are injected into this amplification cavity with a Pockels cell and a polarizer[1]. The injected pulses absorb the energy in the gain medium increasing their own field strength every time they make a round trip in the laser cavity. This process carries on for approximately 20 round-trips until the pulses are switched out of the cavity with a second Pockels cell. Then the temporal stretching stage is reversed using another grating in order to compress the amplified pulses in to a 100 femtoseconds. In the end this amplification stage results in an increase in the instantaneous pulse intensity by a factor of 2×10^6 and a decrease in repetition rate by a factor of 8×10^4. The amplifier output is a train of pulses with temporal length of 100fs, 3mJ energy per pulse, 800nm central wavelength and a repetition rate of 1050Hz.

3.1.1 Single-cycle THz transients

This section describes the characteristics of our THz pulses. Figure 3.2 shows a typical temporal trace of the THz pulses detected by our THz-TDS, ie. a plot of $E(t)$ with

[1]When the Pockels cell is biased with a voltage it changes the polarization of the pulse so that it is transmitted by the polarizer.

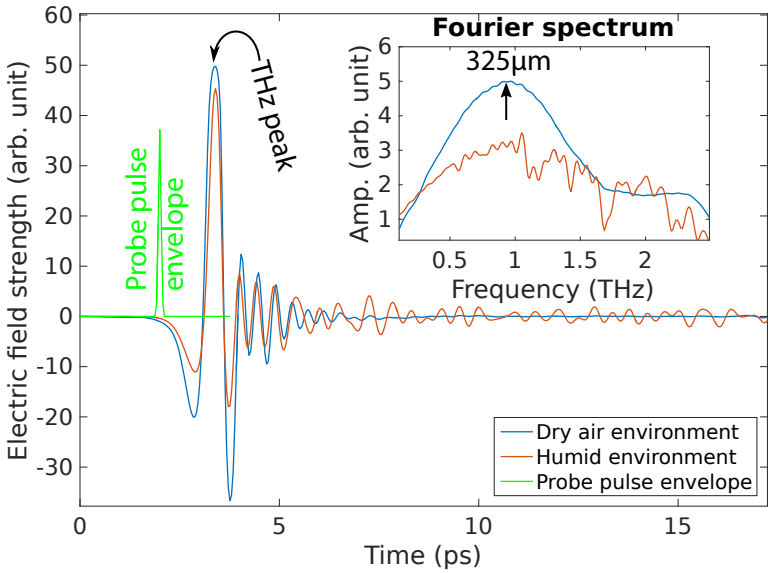

Figure 3.2: Red: typical THz pulse detected by our system in normal room conditions (~35% humidity). Blue: THz pulse recorded in a box pressurized with dry air (air passed through desiccant). Green: envelope of detection pulse used to discretely sample the THz waveform. Arrow points to the maximum field strength of our single-cycle THz pulse. Oscillations after the red THz pulse are due to water vapor in the background environment. ***Inset,*** *Blue(red): Fourier spectrum of the THz pulse without (with) water vapour oscillations.*

$0.04ps$ resolution. The envelope of our probe pulses used to discretely sample the field-strength of our THZ waveform is also shown here in green. The black arrow points to the maximum field value of our THz pulse at $\approx 4.2ps$. In-front and behind this positive value two other peaks with negative values can be seen. This is our main THz waveform which is generated and detected by our system. In the blue line, some other oscillations behind the main THz pulse can be seen. These are dependent of optics and alignment of the system, therefore they they do not change regularly but only when one performs a major change/update to the system[1]. In the red curve, one can see many other oscillations after the main THz pulse. The experimental difference between the red and blue curves is that the red pulse was measured in normal room conditions, where as the blue one was measured in a dry air enclosure[2]. Therefore, the numerous oscillations seen in the red pulse are due to the water vapor in the ambient atmosphere (~35% humidity). These are the rotational modes of the water

[1] For example changing a parabolic mirror or replacing the crystal detector.
[2] The box was pressurized with air that was passed through desiccant.

vapor molecules [81], and consequently the red THz pulse has reduced field-strength.

This measurement is performed in the time domain. Therefore, by Fourier transformation one can obtain the spectrum, including the phase information, of the frequencies in our THz pulse, or mathematically

$$|E(\omega)|e^{i\phi(\omega)} = \int_{\infty}^{\infty} E(t)e^{-2\pi itf}\mathrm{d}t, \tag{3.1}$$

where $\phi(\omega)$ is the phase information at each angular frequency $\omega = 2\pi f$. This Fourier transform implies that our spectral resolution is determined by the temporal length of our measurement. The amplitude spectrum, $|E(2\pi f)|$, of our THz pulse is shown in the inset of fig. 3.2. The full-width-half-maximum and the central frequency of our pulses are $1.3THz$ and $0.95THz$ $(325\mu m)$ respectively. The red line shows the spectrum when the water rotational oscillations are present. They manifest at various frequencies as absorptions lines of different widths. These give artifacts when performing spectroscopic analysis, sec. 3.2, hence they need to be eradicated in experiment if such analysis is required.

3.1.2 THz radiation from non-linear optics

The THz generation and detection mechanisms used here are respectively optical rectification and electro-optic sampling in ZnTe. They are both 2$^{\text{nd}}$ order non-linear polarization effects. The classical description of non-linear polarization phenomena is as follows. Electrons are modeled as masses held in place by non-linear springs. In other words, a Lorentzian oscillator §2.1.2.1 in a non-linear potential with cubic, and higher, displacement dependence terms. The solution to the equation of motion for an input of two superpositioned E-fields with frequencies ω_1 and ω_2 is [82]

$$P_i^{(2)}(\omega_1 - \omega_2) = \epsilon_0 \sum_{j,k} \chi_{i,j,k}^{(2)}(\omega_1 - \omega_2)E_j(\omega_1)E_k^*(\omega_2), \tag{3.2}$$

where $\chi_{i,j,k}^{(2)}$ is the susceptibility tensor and the i, j, k subscripts denote the Cartesian components of polarization. Note, this is the difference frequency term. The case of the sum frequency mixing is observed in the mathematical details [82]. In the early 1960s, Bass et al [83] observed difference frequency mixing, named optical rectification, and Franken et al [84] observed sum frequencies generation.

3.1.2.1 THz generation, Optical Rectification

Optical rectification falls out of eq. (3.2) when we take the limit of $\omega_2 \to \omega_1$,

$$P_i^{(2)}(0) = \epsilon_0 \sum_{j,k} \chi_{i,j,k}^{(2)}(0) E_j(\omega_1) E_k^*(\omega_1). \tag{3.3}$$

One can now see that a strong electric field at ω_1 gives rise to a DC polarization. In practice, the bandwidth of the input laser determines the distribution of difference frequency components. Lasers emitting ultra-short (100fs in this thesis) pulses have frequency bandwidths in the THz regime. Such pulses are shone onto a crystal. This causes a polarization and thus the oscillation of the bound charges. Accelerating charges cause the emission of E-fields. Since the polarization has low frequency components, the emitted field has THz frequencies.

The above process can only occur in crystals where the 2$^{\text{nd}}$ order susceptibility tensor, $\chi^{(2)}$, is non-zero. This excludes all crystals with inversion symmetry[1]. Listed in Table 3.1 are commonly used THz generation crystals and their symmetry point group. The crystal symmetry group determines the crystal's response to the angular orientation of the incoming radiation. ZnTe, the crystal used in this thesis, emits maximum THz when the optical polarization lies in the {110} plane. For crystals cut in this plane, THz generation is then maximized by rotation of the crystal wafer.

Table 3.1: Common THz generation crystals

Material	Point group
$LiNbO_3$, $LiTaO_3$	$3m$
ZnTe, GaAs, GaP, InP	$\bar{4}3m$
GaSe	$\bar{6}2m$

For further optimization the crystals needs: to be transparent with minimal absorption at all frequencies involved, to have a high damage threshold to withstand the intensities needed and to not have other competing non-linear processes. For final generation optimization, one has to have constructive interference between all the waves generated from all points in the crystal. In other words, the THz phase velocity has to be equal to the group velocity of the laser input packet within the material.

[1] All components of $\chi^{(2)}$ equal 0 in crystals with inversion symmetry

If the phase matching condition is fully satisfied, the THz field gradually gets amplified while propagating through the medium. Now consider an optical wave traveling faster than the THz wave. The effective interaction length is given as the coherence length l_c of when either waves are $\pi/2$ out of phase with each other:

$$l_c = \frac{c}{2f_{THz}|n_g - n_{THz}|}, \tag{3.4}$$

where n_g (n_{THz}) is the group (phase) refractive index at the visible (terahertz) frequencies. From eq. (3.4) one can see that $l_c \to \infty$ as $n_g \to n_{THz}$. In reality this condition is hard to satisfy. The most commonly used nonlinear crystal for THz generation is ZnTe because it best satisfies this condition at the operational wavelength (800nm) of Ti:Sapphire lasers. In ZnTe $l_c \to \infty$ for visible wavelengths around 800nm and terahertz frequencies around 1.69THz [85], shown in the fig. 3.3.

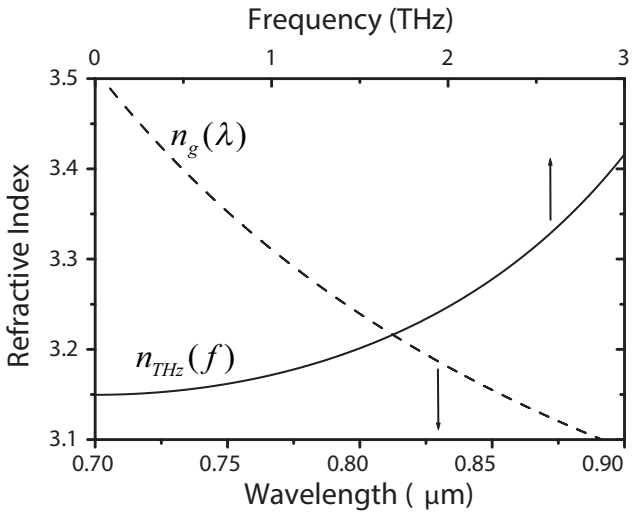

Figure 3.3: Group refractive index n_g and phase refractive index n_{THz} at optical and terahertz regimes, respectively, of ZnTe. Taken from [71]

Finally, one has to consider the crystal's absorption in the spectral region of interest. The dominant causes of absorption in such crystals are the transverse-optical phonon resonances in the terahertz region. Table 3.2 lists such resonances in commonly used crystals.

Table 3.2: Lowest TO-phonon resonances in some EO crystals, taken from [71]

	ZnTe	GaP	InP	GaAs	$LiNbO_3$
f_{TO} (THz)	5.3	11	9.2	8.1	7.7

3.1.2.2 THz Detection, Electro-Optic sampling

The THz detection mechanism used in this thesis is called Electro-Optic (EO) sampling. It falls out of eq. (3.2) when we take the limit of $\omega_2 \to 0$,

$$P_i^{(2)}(\omega_1) = \epsilon_0 \sum_{j,k} \chi_{i,j,k}^{(2)}(\omega_1) E_j(\omega_1) E_k^*(0). \tag{3.5}$$

From eq. (3.5) one can see that a DC electric field, $E_k^*(0)$, gives rise to a polarization $P_i^{(2)}(\omega_1)$ at frequency ω_1. In other words, a static electric field induces a birefringence in the non-linear crystal proportional to the bias field amplitude. This effect is known as the Pockels effect.

The detection of THz relies on the above process. The THz field strength is determined by the measuring the induced birefringence. This is achieved with polarization measurements of an optical probe pulse. Because the THz and visible light pulses have different temporal lengths (Fig. 3.2), the THz field is akin to a DC field when both pulses propagate through the EO crystal. Note, this only holds provided the THz wave and optical pulse travel at the same speed through the medium. The visible light pulse is scanned in time, via an optical delay line, to sample the full temporal THz waveform.

The electro-optic effect is weak. To enhance signal people use a balanced photo-diode detection scheme and a quarter wave-plate, shown in fig. 3.4. The quarter wave-plate is set to circularly polarize the probe beam if there is no THz present. A polarization beam splitter then sends equals amounts of power onto the balanced photo-diodes. Reading the difference in outputs from the diodes will yield zero. However, if the THz is present, the difference in outputs will correspond to the THz field amplitude. To further enhance signal, an optical chopper modulates the generation beam[1] at half the repetition rate of the main laser. One then uses a Lock-In amplifier to only record the modulated signal. This minimizes electrical noise in the circuitry and intensity fluctuations in the main laser.

[1] Can also be the excitation beam

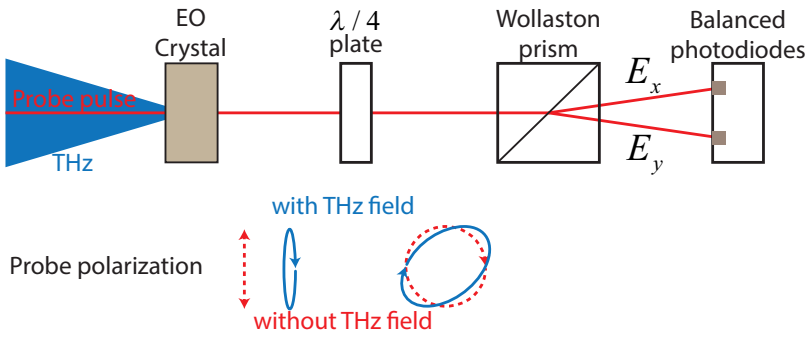

Figure 3.4: A schematic of EO sampling. A focused THz pulse and a detection probe pulse are incident onto an EO crystal. Afterwards, the polarization of the probe pulse is measured by a pair of balanced photodiodes. A Wollaston prism is used to separate the orthogonal polarizations and a quater-wave plate is used to enhance the signal. Probe polarization with (solid) and without (dashed) the THz field are shown before and after the $\lambda/4$ plate.

3.2 THz spectroscopic analysis

Obtaining the frequency dependent refractive index of a sample is the standard use of a THz-TDS. Consider a pulse of radiation incident upon a slab of material. There will be a transmitted and a reflected pulse (see inset of fig. 3.5**left**). The amplitudes of the transmitted and reflected pulses will be related to the incident pulse amplitude via the Fresnel reflection and transmission coefficients, §2.1.1.1. However, multiple reflections will occur within the material, as outlined in §2.1.1.2, hence the transmission and reflection functions of the material are respectively given by eqs. (2.25) and (2.26). Therefore, if one has knowledge the incident wave and measures the transmission through (or reflection of) some material of known thickness, then it is possible to solve eq. (2.25) for the refractive index of the material. We next outline how to extract the refractive index of a plastic cover slip with our system.

In our THz-TDS we perform two measurements: one measuring the temporal waveform transmitted through a sample, $E_{\text{samp}}(t)$, and the other to obtain a reference waveform without the sample , $E_{\text{ref}}(t)$. These two measurements are shown on the left of fig. 3.5. Here one can see that the sample pulse (in red) is at a later time than the reference pulse (in blue). This is because it has traveled through the sample which has a larger refractive index than air[1]. A small pulse at $\sim 14ps$ can be seen in the reference waveform, and it arises from the the first Fabry-Perot reflection in

[1]The reference pulse traveled through air.

the material. Note, some fast oscillations can be see behind our main pulses. They were found to change depending on the optical alignment of our system, hence are associated with detector response function of our ZnTe crystal.

Our measurements contain the relative amplitudes and propagation times of our pulses, therefore a Fourier transform, eq. (3.1), will yield the frequency spectrum and along with the relative phase of each frequency. The frequency spectrum and the phase of our THz pulses are shown on the right of fig. 3.5. Here the solid blue and red lines show the detected transmission spectrum through free-space and our sample respectively. It can be seen that these two solid curves have the similar shapes, however the red curve has small oscillations in it. These are due to the first Fabry-Perot pulse detected in the time-domain measurement. The blue and red dashed lines show the phase[1] of the free-space and our sample waveforms respectively. One can see that the red dashed line has larger values of phase. This is because the sample waveform has accumulated a bigger phase delay by propagating through the sample.

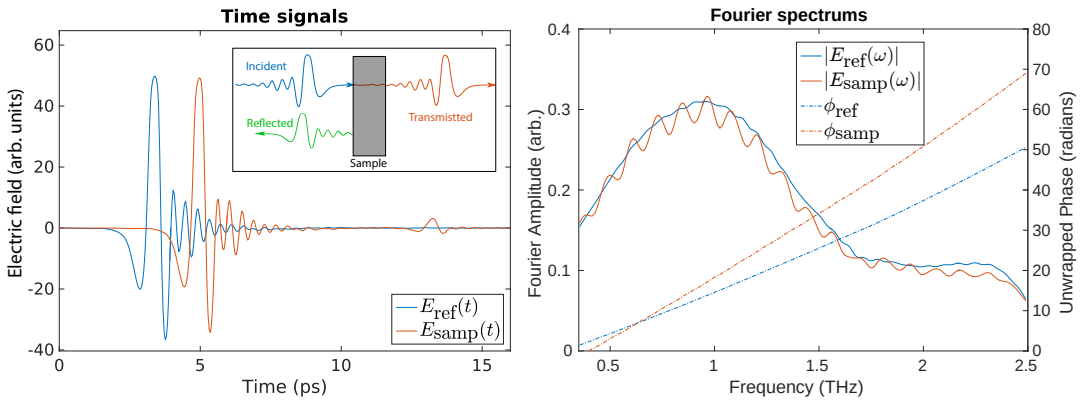

Figure 3.5: ***Left:*** *THZ pulses measured by our system. Blue shows the reference pulse and the red trace shows the THz pulse transmitted through our plastic cover slip (this was a 810μm thick plastic petry dish made from non-cytotoxic virgin polystyrene Sterilin BS EN ISO 24998:2008). Inset shows a schematic illustration of the measurement.* ***Right:*** *Fourier spectrum of the THz pulses on the left. The solid lines are the power spectrum and dashed lines are the unwrapped phase where the blue (red) colour shows the data from the reference (sample) scan.*

After the Fourier transformation, we have $E_{\mathrm{ref}}(\omega)$ and $E_{\mathrm{samp}}(\omega)$ which be substituted in eq. (2.25). Note, our reference measurement is related to the incident

[1]The unwrapped angle, shown here, is typically shown since it does not have 2π discontinuities hence it has more visual appeal.

waveform by $E_{\text{ref}}(\omega)e^{-i\omega L/c} = E_i$, where L is the sample thickness, since it has propagated through air with a refractive index of 1. Therefore we obtain

$$\frac{E_{\text{samp}}(\omega)}{E_{\text{ref}}(\omega)e^{-i\omega L/c}} = \frac{t_1 t_2 e^{i\phi_n}}{1 - r_1 r_2 e^{2i\phi_n}}, \tag{3.6}$$

where $\phi_n = \omega n L/c$ is the phase delay the wave accumulates by propagating through our sample, $t_{1,2}, r_{1,2}$ are the relevant Fresnel coefficients, eqs. (2.21-2.23). The only unknown left is the refractive index of our sample, n, which can be solved for numerically at each frequency point. Since our measurement contains the relative amplitudes and the relative phases, our solution can obtain the complex refractive index. However, since the phase term is 2π periodic there is an infinite number of solutions that satisfy eq. (3.6). Therefore, selecting the correct solution is of vital importance. This accomplished by making an initial guess at the refractive index. This guess can be made by looking at the time difference between the reference and sample waveforms. If we denote the temporal co-ordinates of the peaks of the sample and reference waveforms as t_s and t_r respectively, one obtains

$$n_r = 1 + \frac{(t_s - t_r)c}{L} \tag{3.7}$$

as the real part of the average refractive index. For non-absorbing samples this will suffice. However, should the sample be absorbing then one can use the above value and

$$\frac{|E_{\text{samp}}(\omega_c)|}{|E_{\text{ref}}(\omega_c)|} = t_1 t_2 e^{-n_i \omega_c L/c}, \tag{3.8}$$

where ω_c is the central angular frequency of the pulses and n_i is the imaginary part of the refractive index, to obtain an initial guess for the imaginary part[1]. A more accurate estimate is obtained by saying $t_{1,2}$ are also functions of n_i, however a numerical solver needs to then be used. Although crude, this initial guess will ensure that the numerical solver[2] of eq. (3.6) will find the physically relevant solution. A technical note, this crude initial guess is used only for the first frequency point inputed into the solver. Then the solution from the first frequency point is used as the initial guess for the second frequency point. This process is iterated until one has a solution for all the

[1] This equation is only valid if we consider only the first transmitted pulse through our sample, ie. zero out the Fabry-Perot pulses in the temporal measurement

[2] The numerical solve we use is the *vpasolve* function built into MATLAB 2016b.

frequencies in the spectrum. This iterative process ensures that the obtained refractive index is a continuous function.

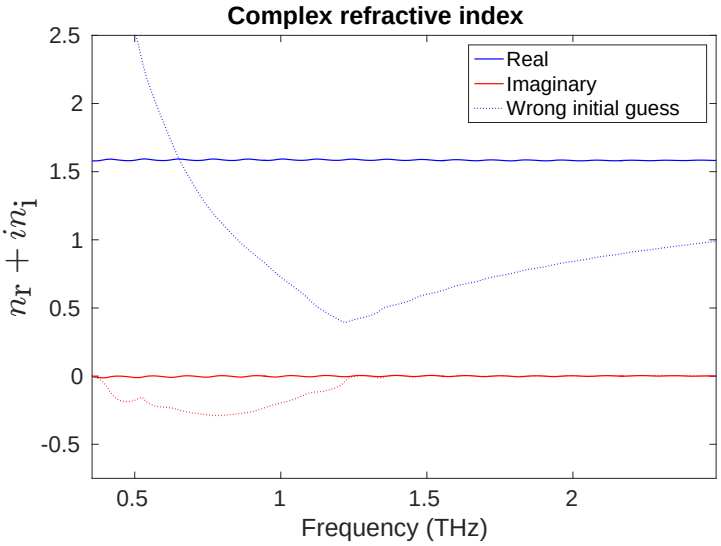

Figure 3.6: Refractive index of plastic cover slip. Solid blue and red lines respectively show the real and imaginary refractive index with an initial guess of $n = 1.50$. *The dashed lines show the obtained refractive index with an initial guess with* $n = 3$.

Figure 3.6 shows the real and imaginary refractive index of the plastic cover slip[1] used as a sample in the temporal measurements of fig. 3.5. The solid lines show the obtained solution using the initial guess of eq. (3.7) with the real (imaginary) part in blue (red). One can see a very flat dispersionless response with no absorption. However, one can see small oscillations. These are due to the fact that we have solved for the Fabry-Perot equation whereas in the temporal measurement we measured only the first Fabry-Perot pulse. The dotted lines show the obtained solution with an initial guess of $n = 3$. This solution is obviously false since it means that we have gain from 0.3 to $1.25THz$ in the imaginary part (dotted red line) and the real part (dotted blue line) is less than 1 from 0.8 to $2.4THz$.

This dispersion-less non-absorbing response from this type of plastic is very useful for THz measurements. The reason is they are originally designed to be used as petri dishes, hence they are non-toxic to bacteria, optically transparent, thermally resistant, mechanically rigid and readily available. These qualities make them excellent alternatives to glass cover slips, as used in the visible regime, since glasses absorb

[1] This was a $810\mu m$ thick plastic petry dish made from non-cytotoxic virgin polystyrene Sterilin BS EN ISO 24998:2008

THz radiation. The optical transparency can in principle allow a THz and an optical image to be taken simultaneously. More over, the main imaging technique in this thesis (described in the later sections of this chapter) uses visible light to switch the material response of silicon from dielectric to metal (§3.3), which has allowed the placement of a near-field THz probe next to a biological sample as shown in ch. 8.

3.2.1 Multi-layer systems

The previous section is only applicable if there are 3 materials, in other words the sample is free standing in space. However, if our sample is enclosed by two cover slips, ie. it is a multi-layered system, then it is convenient to use the transfer matrix method [86]. As before, our measurement contains the transmission coefficients, however our transmission function of the system is [86, 87]

$$t = \frac{2\sqrt{\epsilon_i}}{M_{21} + \sqrt{\epsilon_i}M_{11} + \sqrt{\epsilon_f}(M_{22} + \sqrt{\epsilon_i}M_{12})}, \tag{3.9}$$

where ϵ_i and ϵ_f are the permittivities of the initial and final media, respectively, enclosing the multilayer system and M is a 2×2 matrix associated with the propagation through the entire multilayer system. This matrix is given by the product of the individual layer matrices, $M \equiv M_1M_2M_3...M_N$, describing the propagation through each layer. The characteristic matrix of the j^{th} layer, M_j, with thickness l_j and dielectric function ϵ_j is given by

$$M_j = \begin{bmatrix} \cos\beta_j & \frac{-i}{\sqrt{\epsilon_j}}\sin\beta_j \\ -i\sqrt{\epsilon_j}\sin\beta_j & \cos\beta_j \end{bmatrix}, \tag{3.10}$$

where $\beta_j = \omega l_j\sqrt{\epsilon_j}/c$ is the phase delay associated with light propagation inside the j^{th} layer. By equating the experimental amplitude transmission coefficients $E_{\text{samp}}/E_{\text{ref}}$ with (3.9), we can then numerically solve for the permittivity of the sample as before. Then one can divide the transmission functions of the different systems and equate them to the experimental amplitudes. Note, it is of preference that the materials used in the reference measurement are not absorptive hence improve signal to noise.

This multi-layer analysis allows one model much more complex systems than a simple Fabry-Perot model. We use this multi-layer analysis in chapter 8.

3.3 THz modulation via photoexcitation of Si

3.3.1 Silicon photoexcitation

Undoped high-resist silicon is a dielectric for THz frequencies. It has a dispersionless refractive index of 3.42 from 0.5 to $4.5THz$ with minimal absorption [73]. It has very few charge carriers, therefore its Drude plasma frequency lies below the terahertz regime. However, if the number of charge carriers is increased via photoexcitation, then silicon can behave as a classical Drude conductor [74]. This has allowed for amplitude, phase and frequency modulation of THz via the optical excitation of silicon [74]. More recently, people have built upon these ideas to create an optically modulated wire-grid polarizer [75] in Silicon. There are other materials which have similar properties such as InSb and GaAs.

We next consider controlling the carrier density via optical excitation in our system. Consider the Drude model permittivity, §2.1.2.2,

$$\epsilon(\omega) = \epsilon_\infty + \frac{i\omega_p^2}{\omega(1/\tau - i\omega)} = \epsilon_\infty + \frac{iNe^2}{\epsilon_0 m\omega(1/\tau - i\omega)}, \tag{3.11}$$

where N is the number of charge carriers, e is the electron charge and τ is the average carrier collision time ($160fs$ for undoped silicon [88]). Here, the number of charge carriers, the primary modulating parameter, is modulated via optical excitation with photons of energy $\hbar\omega$. When such pulses hit this material electrons in the valance band are given enough energy for them to enter the conduction band[1]. In other words, they are no longer bound in the potential of the positive ion core they were orbiting and hence are able to traverse through the medium. Note, now there will also exist a vacant electron orbital referred to as a hole. Holes can travel through medium and act as though they have positive charge, thus are also considered as charge carriers. The excited electrons will then decay back down to their ground state and recombine with the vacant holes. The electron and hole populations at time t after photoexcitation are given by $N(t) = N(0)e^{-\tau_c t}$, where τ_c is known as the carrier lifetime. In silicon the carrier lifetime is $25\mu s$ [89]. The repetition period of our pulses is $1ms$, hence by the time our next pulse arrives all the carriers will have relaxed to their ground state. This allows us to neglect sample heating. Furthermore,

[1] This is provided the photons have enough energy to overcome the silicon bandgap of $1.12eV$ ($1100nm$) at room temperature.

since our THz-TDS allows us to probe our silicon picoseconds after photoexcitation, discussed in §3.3.2, we can also neglect carrier recombination effects. The key variable to determine is therefore the mean carrier-carrier distance. In our system, we probe our material $5ps$ after photoexcitation, see Fig. 3.9, thus we can calculate the mean square displacement of carriers via eq. (2.42). We obtain mean displacements of $\sqrt{< x^2 >} = 506nm(425nm)$[1] for our photo-electrons (holes). Since the diffusion lengths are considerably smaller than the penetration depth of the photoexcitation light (12μm [78]), we can neglect carrier diffusion from our considerations. Therefore, one only needs to consider the carrier generation rate. We arrive at a charge carrier density of

$$N = \frac{I_0(1-R)}{2\hbar\omega Ad} \tag{3.12}$$

where I_0 is the incident intensity, R is the reflectivity of Si at the incident wavelength, d is the penetration depth and A is the area of excitation.

In all experiments involving silicon as the photomodulator, ch. 4, 5, 6, 8, our pulse energy per unit area is $\sim 100\mu$J/cm^2, $R = 0.3$ is the Fresnel reflectance of a Si interface at our excitation wavelengths, $\hbar\omega_l$ is the photon energy of the $800nm$ pump light, d is the penetration depth ($d\approx 12\mu$m [78] for our wavelengths) and the factor of 2 accounts for the excitation of electrons and holes. Using the average of the electron and hole masses, we obtain a Drude plasma frequency (eq. 2.40) of $70THz$ with $\epsilon(1THz) = -101 + 36i$ for our photoexcited silicon. In other words, we generate a THz material with a negative real and positive imaginary part to the dielectric function, the characteristics of a lossy conductor.

3.3.2 Photoexcitation studies with THz-TDS

THz pump-probe spectroscopy allows one to study carrier photoexcitation and relaxation dynamics on picosecond time scales. This is achieved by investigating how the THz pulse changes at different excitation times. For now we ignore what happens at different excitation times and return to this later. In figure 3.7 we plot the THz pulses transmitted through undoped (solid line, E_{ref}) and photoexcited (dashed line, E_{photo}) silicon. For the undoped silicon, we can see the main THz pulse at $\sim 2ps$, then we see the 2$^{\text{nd}}$ and 3$^{\text{rd}}$ Fabry-Perot pulses arriving at $\sim 5ps$ and $\sim 7.5ps$ re-

[1] These numbers determine subsequent smearing and broadening of spatial features should an optical pattern be transferred to a THz beam using a silicon photomodulator. How we transfer an optical pattern to a THz beam is discussed in §3.4.1.

spectively. In the Fourier spectrum these secondary pulses manifest themselves as the Fabry-Perot peaks seen here. The pulse transmitted through the photoexcited silicon (dashed red line) is seen to have a similar shape as the other one and it arrives at the same time. However, the amplitude has been decreased by $\sim 85\%$. This is because, as discussed in the previous section, we have generated a lossy conductor which has absorbed our THz radiation. Consequently, Fourier spectrum of this pulse has much lower amplitudes.

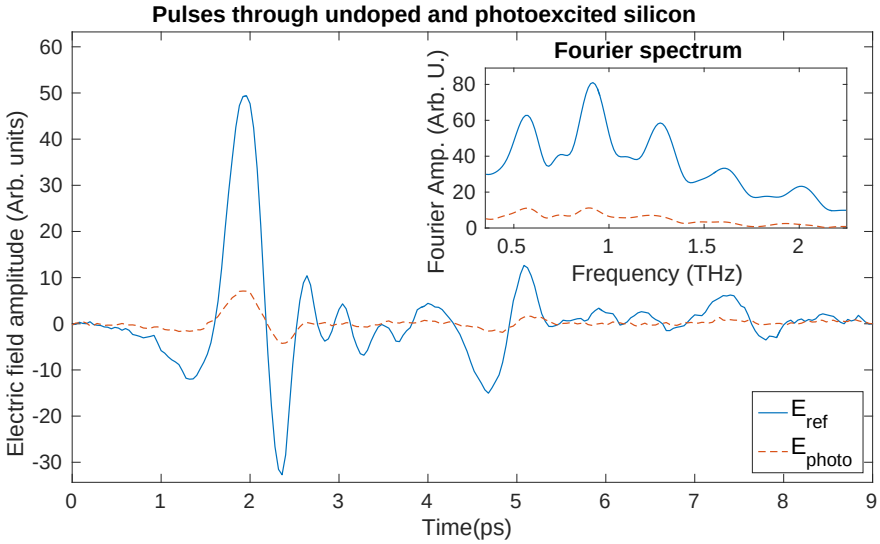

Figure 3.7: THz pulses transmitted through an undoped (solid blue line) and a photoexcited (dashed red line) silicon wafer ($115\mu m$ thick, $1000\Omega \cdot cm$ resist). Wafer is excited with $800nm$ pump light with $\sim 100\mu J/cm^2$ fluence. Inset shows that Fourier transform of the pulses.

We can calculate the transmission of the photoexcited silicon from the the pulses in Fig. 3.7. This is achieved by dividing the spectra of the photoexcited pulse by the other one, ie. $|E_{\text{photo}}/E_{\text{ref}}|$. This is what is plotted in figure 3.8 as the solid blue line. You can see that the transmission goes from 0.17 in our low frequencies to 0.07 in our higher frequencies. From eq. (3.11) the higher frequencies see a less absorbing material, however the shorter wavelengths see an optically thicker absorbing material. The latter mechanism seems to win over our frequency range hence the decrease in transmission. This is supported by modeling[1]. However, there is a mismatch in the

[1]Our model consists of calculating the transmission through a 2-layer system using eq. (3.9). The first layer is the photoexcited region of thickness $15\mu m$ (a small amount more than the penetration depth) with permittivity given by eq. (3.11) with $\omega_p = 71THz$ and the second layer is undoped silicon of thickness $100\mu m$ (wafer used in experiment was $115\mu m$ thick).

number of peaks with experiment, namely there are 5 peaks in experiment and only 3 in modeling. This is because our model assumes a homogeneous photoexcitation layer where as in experiment the power is absorbed with an exponential decay rate with penetration depth of $12\mu m$. Thus in experiment there is no sharp boundary that the Fabry-Perot reflections to interact with. Note that due to the large silicon refractive index of 3.42, the photoexcitation layer can not be assumed to be an infinitely thin sheet either. This mismatch changes the Fabry-Perot resonance conditions in experiment and modeling. Further, in experiment we have a small amount of water vapor present affecting our measurements.

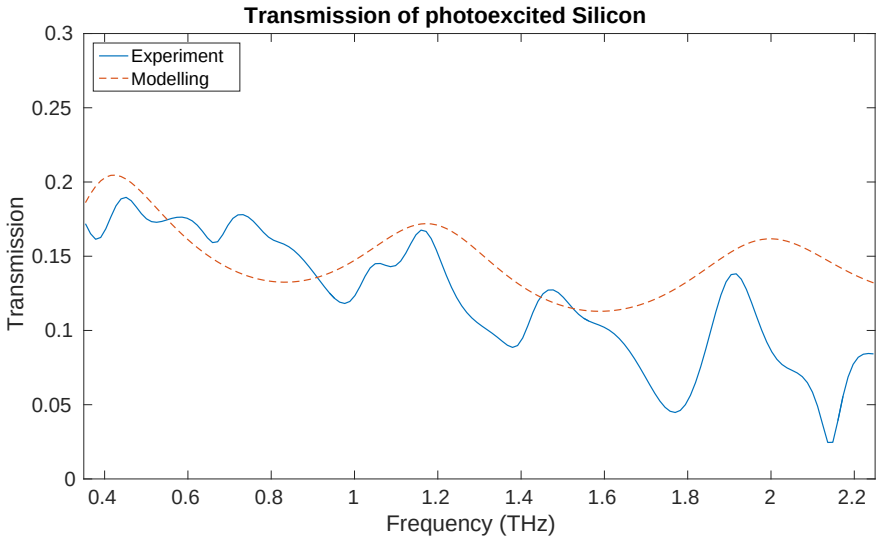

Figure 3.8: Amplitude transmission through photoexcited silicon with experiment and modeling in solid blue and dashed red lines respectively. There is a ∼2.5% error in the experimental measurement. This error arises from the noise in the measurement of our THz waveforms, ∼5% (see fig. 6.1), and the number of averages, 5, therefore rounding up the error is $\sim 5/\sqrt{5} \approx 2.5\%$.

The previous two paragraphs have so far ignored what happens when we vary the arrival time of the pump excitation pulse. This is what will be considered next. For this we overlap our detection pulse overlapped with the peak of our THz waveform, as indicated in the inset of fig. 3.9. Then we change when our pump excitation pulse arrives at our silicon sample. Note, we measure the change in transmission due to photoexcitation, ie. $\Delta E = E_{\text{ref}} - E_{\text{photo}}$ from fig. 3.7. For negative arrival times the pump arrives after our THz pulse. Therefore, since the THz pulse has passed through the sample unphotoexcited, we do expect a value of zero for ΔE. This is

what we observe. When the pump pulse arrives at similar times as the THz pulse, we start to observe non-zero values. This is because the photoexcitation has started to generate charge carriers and thus change the permittivity. These photoexcited carriers will eventually relax back down to their ground state. However, in silicon carrier relaxation occurs on microsecond time scales [89] and our system measures up to a nanosecond difference in time delay[1].

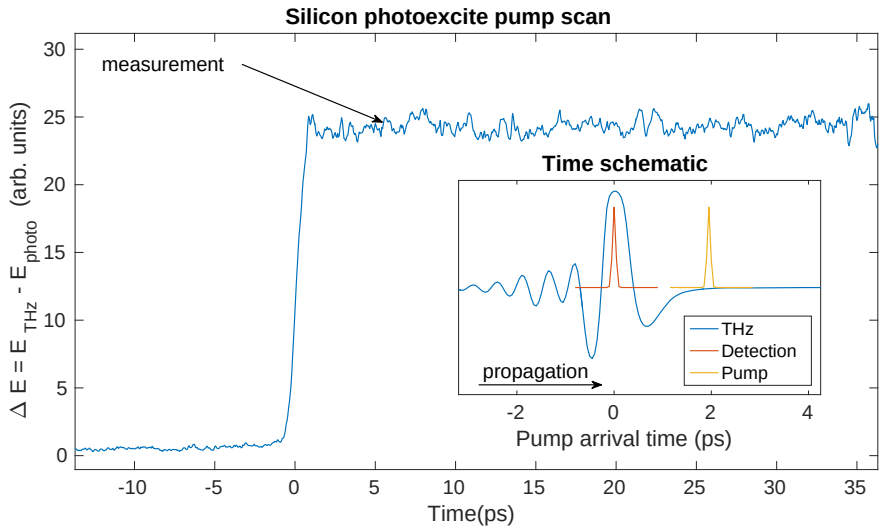

Figure 3.9: Difference in THz transmission due to the photoexcitation of silicon. Inset shows a schematic illustrating when the pump pulse arrives on the sample with respect to the THz and detection pulses. Propagation arrow points the direction which the pulses are traveling.

The black arrow labeled as "measurement" indicates when the pump pulse arrives on our silicon wafer when we use the photoexcitation of silicon for imaging with a single-element detector, discussed in the next section.

3.4 Imaging with a Single-Element Detector

THz detector arrays are currently difficult and expensive to manufacture [90]. As a consequence, we can not use array based imaging techniques, such as those used in the modern day cameras, where one uses a lens to project an image of some scene on a detector array, thereby obtaining the intensity (or amplitude) of each spatial point of the scene simultaneously. Our detector can only measure the total amplitude

[1] This is due to light traveling $30cm$ in $1ns$, hence the need for much longer delay lines.

emanating from the scene, hence why it is called a single-element detector. The simplest way of imaging with such a detector is to block the light from the entire scene leaving only a small square to be transmissive, an aperture. Then our detector readout will correspond to the light emanating from that small square, the first pixel in our image. If we move the aperture and measure again, then we will the know the light emanating from the area adjacent to our first measurement. This process is iterated until we have sampled the entire scene. In other words, our imaging measurements are obtained sequentially rather than in parallel. For this reason, single-element imaging typically has a longer acquisition time compared to focal plane imaging arrays, its major disadvantage. However, single-element detectors are generally cheaper and more robust.

The resolution of a raster scanning technique, as outlined above, is determined by size of the aperture. However, if this aperture is made smaller and smaller, the light reaching our detector is reduced and eventually one will run into detector noise.

One could sample more than one aperture simultaneously to increase the detected signal level in order to overcome detector noise, an idea which seems to first originate in 1935 with Yates [91]. This idea is illustrated in fig. 3.10. Here, we have a light source shining upon a spatial encoding mask (ie. it has many apertures open as opposed to one). This spatially encodes a beam of radiation, and then this beam passes through an object and all the light is gathered by a single-element detector. In the next measurement we change the configuration of our encoding mask (ie. change the location of the apertures) and measure again. Although we have increased the light reaching our detector in each measurement, to form an image with such encoding masks, however, introduces extra calculation difficulties as the measured intensity is due to the sum of the scanning apertures. Therefore, the mask configurations (the locations of the scanning apertures) in each measurement must form a set of simultaneous equations which can be solved for the individual pixels of the object's transmission function.

We now consider the construction of an N-pixel image $\mathbf{y}$; our i^{th} measurement, y_i, is the dot product of the object transmission function and the i^{th} mask configuration, mathematically expressed as

$$y_i = \sum_{j=1}^{N} a_{ij} x_j, \tag{3.13}$$

where a_{ij} holds the spatial information of the i^{th} mask and x_j is the j^{th} pixel of the

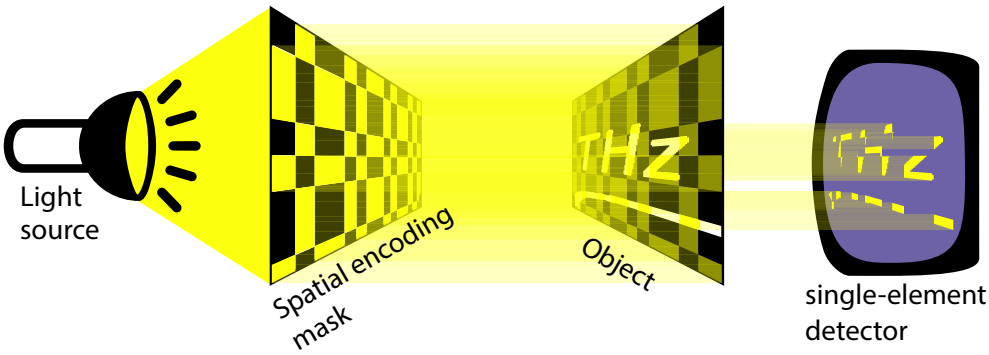

Figure 3.10: Imaging with a single-element detector. An encoding mask spatially encodes a beam of radiation. Follow this, the beam is passed through an object and onto the single-element detector.

object. The full set of measurements can be represented by the matrix equation

$$\mathbf{y} = A\mathbf{x}, \tag{3.14}$$

where the rows of matrix A are shaped into the projected masks. For invertible matrices A, the image vector $\mathbf{x}$ can be obtained through matrix inversion $\mathbf{x} = A^{-1}\mathbf{y}$. Otherwise, one can use least squares solvers and more complicated recovery algorithms. Note that $\mathbf{x}$ then has to be reshaped into a 2D matrix of pixel values. A note on terminology, the matrix equation (3.14) represents the image being expanded in some basis given by A and they are discussed in §3.4.2.

3.4.1 Implementation in the THz regime

As discussed in §3.3, the material response of an undoped Silicon wafer can be switched from dielectric to conducting via photoexcitation with high energy pulses, ie. it can be made to absorb and block our THz radiation. Therefore, to spatially pattern our THz we can photoexcite this silicon wafer with the desired spatial pattern. To this end, we use a digital micromirror device[1] (DMD) to impart a spatial structure into the pump beam used to photoexcite the silicon wafer, as illustrated by Fig. 3.11. The photoexcited regions have values of 0, in eq. (3.14), since they absorb our THz radiation where as the other regions transmit THz and thus they have values of 1. Then we pass our THz pulse through this spatially photoexcited space, then through an object and finally on our single-element detector.

[1]We use the DLP lightcrafter evaluation module by Texas instruments.

Our physical masks are composed of 1s and 0s whereas some encoding schemes might be made of +1s and -1s, for example orthogonal masks derived from Hadamard matrices. However, as is outlined in [92], we can still perform a measurement with masks made +1s and -1s in our system. Consider the H_2 matrix and two other matrices G^+ and G^-:

$$H_2 = \begin{bmatrix} 1 & 1 \\ 1 & -1 \end{bmatrix}, \quad G^+ = \begin{bmatrix} 1 & 1 \\ 1 & 0 \end{bmatrix}, \quad G^- = \begin{bmatrix} 0 & 0 \\ 0 & 1 \end{bmatrix}. \tag{3.15}$$

It is easy to see that $H_2 = G^+ - G^-$. Thus if we have two sets of measurement vectors each using one of the complementary sets of masks, $\mathbf{y}^+ = G^+\mathbf{x}$ and $\mathbf{y}^- = G^-\mathbf{x}$, then subtraction of the second set gives the desired encoding matrix. This doubles the number of measurements required. However, due to detection scheme used, discussed in §3.1.2.2, the difference in THz transmission is obtained via a Lock-In amplifier. Our DMD is triggered by the main laser to switch between the $+ve$ and $-ve$ masks. This prevents doubling the total measurement time. This is because we use a Lock-In to detect the difference when the THz is switched on and off onto our detector. Moreover, since the complementary negative mask is projected immediately after its positive counterpart, one can eliminate an unwanted source of noise, namely low frequency source oscillations as shown in §6.2.1.

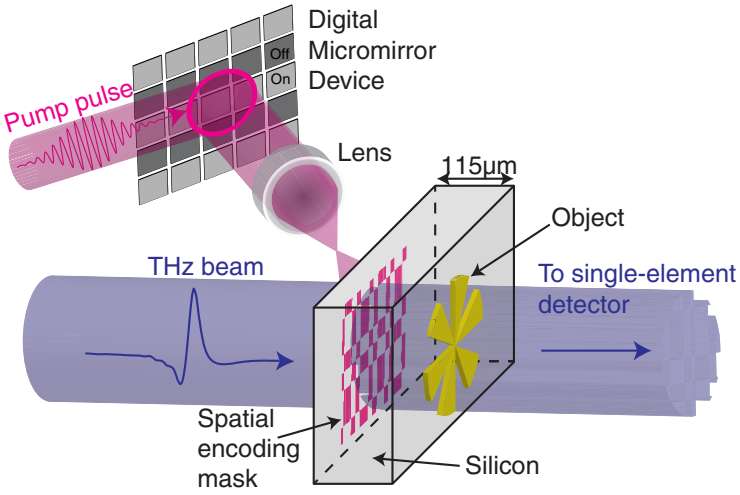

Figure 3.11: ***Single pixel THz imaging****: An 800nm pump pulse is spatially modulated and used to photoexcite a semiconducting wafer, which transfers the spatial encoding mask onto a coincident THz pulse. The subsequent THz pulse is then passed through an object onto a single pixel detector.*

3.4.1.1 Phase Front Correction

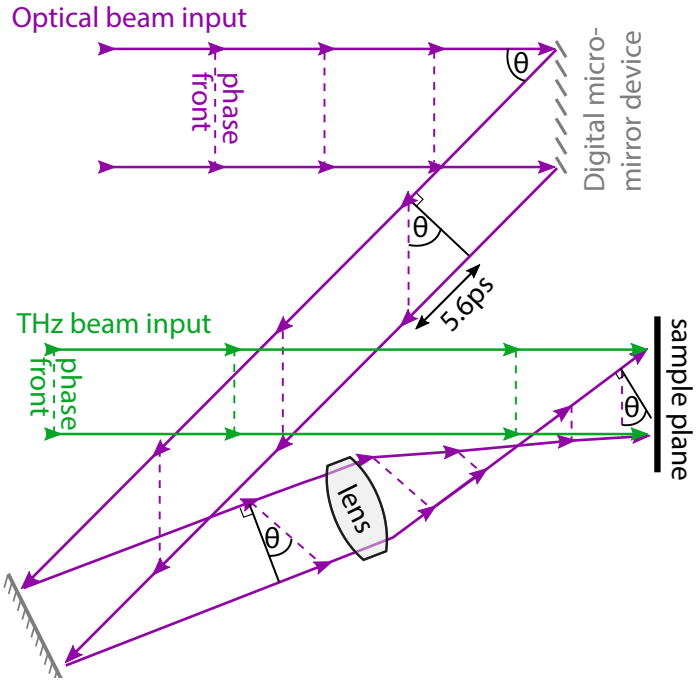

Figure 3.12: Diagram of the optical excitation scheme showing how a flat phase front is achieved with off axis photoexcitation. Each micro-mirror tilts at $\theta = 13^o$ to DMD array plane.

It needs to be mentioned that there is a phase front distortion induced by the DMD. This phase front distortion arises from the fact that each individual mirror tilts on its own at a 13° angle with respect to the overall mirror plane. This shortens, or lengthens, the optical path length of light hitting a mirror on the edge of the DMD array compared to one in the middle, as shown in fig. 3.12. This means one will photo-excite different parts of the sample at different times. Therefore, if one wishes to study ultra-fast carrier dynamics, in graphene for example (see ch. 7), this wavefront distortion needs to be removed. This is achieved by photoexciting at an angle off normal opposite to the angle of the DMD mirrors. Figure 3.12 clarifies the arrangement used to achieve a photo-excitation without a temporally smeared wavefront.

3.4.2 Choice of basis: Raster, Orthogonal, Random

Next we outline the ideas behind using three different measurement matrices, namely the identity matrix, orthogonal and random matrices. How each one of these performs in noisy experimental conditions is shown in chapter 6.

3.4.2.1 Raster Scanning

As pointed out earlier, we can raster scan a single aperture across our field of view. This means our i^{th} measurement directly corresponds to i^{th} pixel of our image. In the matrix notation of eq. (3.14), A is the identity matrix I_N.

There is one great disadvantage to using raster scanning techniques. Namely that to increase resolution the aperture size is reduced, however this also reduces the amount of light transmitted through an aperture. Therefore, by continual decrease of the aperture size eventually one will only measure detector noise. For apertures much larger than the wavelength the amplitude transmission is proportional to the area, i.e. $E \propto r^2$ where r is the aperture radius and E is the transmitted field amplitude. However, when the aperture size is smaller than the wavelength the dependence is described by Bethe's theory [93], mathematically $E \propto r^3$. This has already been demonstrated for THz frequencies [94] and such apertures can achieve $3\mu m$ spatial resolution [51]. It also possible to overcome the small transmissions of apertures and use near-field scattering tips [43] in order to reach nm resolution [45, 47]. Whilst impressive, raster scanning techniques necessitate long measurement times due to the small signals emanating from sub-wavelength scatterers.

3.4.2.2 Orthogonal Hadamard matrices

In this section, we use orthogonal Hadamard matrices as our basis expansion. So, A is a Hadamard matrix of order N. A Hadamard matrix H_n is defined as an $n \times n$ matrix of +1s and -1s with the property that the scalar product between any two distinct rows is 0 (each row is orthogonal to every other one). Thus H_n satisfies:

$$H_n H_n^T = H_n^T H_n = nI_n, \tag{3.16}$$

where H_n^T is the transpose of H_n. This allows for easy image reconstruction since $H_n^{-1} = H_n^T/n$, which is equivalent to summing the projected patterns with each pattern weighted by its detector readout.

Every Hadamard mask (apart from the first one which is all 1s) has equal amounts of 1s and -1s, therefore in every measurement we use half of the total incident light. Therefore, a Hadamard basis will minimize the effect of detector noise [95]. This is the major reason why one should use a Hadamard sampling matrix. However, it should be noted that this Hadamard imaging scheme is quite sensitive to source noise. To explain this we modify eq. (3.14) into $\mathbf{Ry} = A\mathbf{x}$ where $\mathbf{R}$ is an N-sized vector with the i^{th} entry describing our source's power output at the time of measurement and $\mathbf{y}$ is the noiseless measurement vector. The i^{th} entry of $\mathbf{R}$ is the total power transmitted through the i^{th} mask, in other words the sum of the dot product between the i^{th} mask and source power output at the time of measurement. With Hadamard masks we use of half of the total light in each measurement. Therefore, 5% source noise fluctuations manifest themselves as 2.5% noise fluctuations in $\mathbf{R}$. For this reason, Hadamard imaging schemes are much more sensitive to source noise than raster scanning schemes[1]. Although source noise can be minimized by using $+ve$ and $-ve$ mask pairs, as demonstrated in §6.2.1, it still makes this Hadamard scheme unfavorable should one have a noisy source but a low-noise detector.

The most common method of constructing Hadamard matrices is via the *Sylvester construction method*, first used in the 1860s. If we have some Hadamard matrix H_n of order n, then

$$H_{2n} = \begin{bmatrix} H_n & H_n \\ H_n & -H_n \end{bmatrix}. \tag{3.17}$$

The lowest Hadamard matrix is $H_1 = [1]$, therefore using eq. (3.17) one can construct matrix of order 2^k where k is a real integer. This is the most common method due to its simplicity, however it can be quite restrictive in terms of the number of pixels one can use, namely only powers of 2. Further more, for an $N \times N$ image one needs an $N^2 \times N^2$ matrix, which can cause memory problems when $N > 512$.

There is another construction method, the *Paley construction technique*. Let q be a prime power congruent to $3(\mod 4)$. Then one constructs a vector, V, of length

[1] In raster scanning we only use very small amounts light in each measurement, hence source noise minimized

q in which the i^{th} entry equals $\chi(i-1)$, where

$$\chi(x) = \begin{cases} 0 & \text{if } x = 0 \\ 1 & \text{if } x \text{ is a quadratic residue of } q \\ -1 & \text{if } x \text{ is a quadratic non-residue of } q. \end{cases} \tag{3.18}$$

Then one constructs a $q \times q$ matrix, Q, where the j^{th} row is obtained by cyclically permuting V to the right $j-1$ times. Finally,

$$H_{q+1} = I + \begin{bmatrix} 0 & J^T \\ -J & Q \end{bmatrix}, \tag{3.19}$$

where J is a column vector of length q where every entry equals 1 and I is the identity matrix. This method has two great advantages over the Sylvester method. First, it has greater freedom in terms of how many pixels one can sample since the allowed matrices are of order $q+1$ where q is a prime congruent to $3(\mod 4)$. Second, due to the cyclic permutation of V, one can construct each individual mask whilst only holding a vector of length $(N-1)^2$ in memory.

Note, when creating masks of subwavelength dimensions, as in this thesis, then polarization effects in the masks need to be considered. This is done in §5.3.2.

3.4.2.3 Random matrices

In this section we discuss the scenario of when A is a random matrix, such as Gaussian iid matrices or Bernoulli matrices as used in compressed sensing [59]. Note that for a fairer comparison with Hadamard matrices the random matrices used in this thesis always consist of only $+1s$ and $-1s$. Random matrices do not offer better noise suppression than orthogonal ones, however compared to raster scanning they increase the amount of light reaching a detector due to the number of opened apertures in each measurement.

The main motivation for using a random matrix to sample your object is that it allows for the reconstruction of an image using an undersampled set of measurements, ie. fewer measurements than number of pixels. In terms of the notations of eq. (3.14), A is now an M by N matrix, $\mathbf{y}$ is M sized vector of our measurements and $\mathbf{x}$ is our N-pixel image that is to be reconstructed. Unfortunately, A is no longer invertible and there exist an infinite amount of solutions to this problem. Obtaining the physically

relevant solution is key and also the difficult part.

An intuitive explanation of compressed sensing is obtained by reversing image compression schemes. Briefly, an image is Fourier transformed and then any spatial frequencies with small amplitudes are discarded. This reduced data set is then Fourier inversed to show an approximate representation of the image. This final image is stored using less memory space hence is considered a compressed representation of the image. In essence, one tries to find the sparsest representation of the image data using some basis, and in the previous example this is done using a Fourier basis. Compressed sensing aims at obtaining this "compressed representation" of the image without fully measuring the object. This is achieved by finding the sparsest vector $\mathbf{x}$ that satisfies eq. (3.14).

A vector is considered k-sparse if it has k non-zero components. The number of non-zero components are measured with a l_0 norm, defined as $||x||_0 := \#\{i : x_i \neq 0\}$ [58]. Then the mathematical problem is stated as

$$\text{min } ||x||_0 \text{ subject to } y = Ax. \tag{3.20}$$

However, this problem is NP-hard [96]. In one of the two fundamental compressed sensing papers [97] the l_0 norm was replaced with the l_1 norm, the closest norm to it. Thus they solved the following minimization problem

$$\text{min } ||x||_1 \text{ subject to } y = Ax. \tag{3.21}$$

Many compressed sensing papers concern themselves with when does '$l_0 = l_1$'. However, we shy away from such considerations and point out that our measurements have a lot of noise. Therefore, we point to an alternative algorithm better able to cope with noise. Namely,

$$\text{min } ||x||_1 \text{ subject to } ||Ax - y||_2 \leq \gamma, \tag{3.22}$$

where γ is a parameter used to determine the 'smoothness' of the final image[1]. Finally, total variation minimization algorithms have been shown to denoise images

[1] In our system, this value depends on the amount of noise in the measurements.

[98]. Hence, we also consider the the following problem

$$\text{min TV}(x) \;\; \text{subject to } ||Ax - y||_2 \leq \gamma, \tag{3.23}$$

and TV is total variation of our image defined as

$$\text{TV}(x') := \sum_i \sqrt{(D_h x')_i^2 + (D_v x')_i^2}, \tag{3.24}$$

where x' is a 2D image and $D_{h,v}$ are the discretized gradient operators along the horizontal and vertical directions respectively. All three problems of eqs. (3.21-3.23) have been solved using the L1-magic package, see reference [99] for algorithm details and downloadable MATLAB scripts.

A final note on image reconstruction, if we sum the projected patterns with each pattern weighted by its detector readout, akin to the orthogonal image reconstruction, then we can also obtain an image. This is a computationally simple and fast method used a initial guess for the more complex algorithms of eqs. (3.21-3.23).

3.4.3 Adaptive Computational Imaging

The previous section concerns itself with how to sample a desired region with three distinct measurement matrices. However, once an image with a particular number of pixels has been taken, one can calculate which regions are interesting and then sample them with smaller pixel sizes. This reduces total measurement time since measurements are concentrated in the regions of interest only. This process can be iterated until the desired pixel size is reached. This is the idea of reference [100] and is an alternative to compressed sensing.

We first measure a low resolution image (I_i) consisting of $N_i \times N_i$ pixels, where i is the tier number. $i = 1$ in the first case. This image is measured using a full set of Hadamard projections (Sylvester construction), and the reconstruction is the weighted sum of the Hadamard patterns, each weighted by its detector readout. Next we perform a single tier Haar Wavelet transform on I_1. In general the single tier Haar wavelet transform T_i is calculated as follows, where T_i' is the partial Haar transform calculated as an intermediate step.

$$T_i'(x, y) = I_i(2x, y) + I_i(2x + 1, y) \tag{3.25}$$

$$T_i'(x + N_i/2, y) = I_i(2x, y) - I_i(2x + 1, y) \tag{3.26}$$

$$T_i(x, y) = T_i'(x, 2y) + T_i'(x, 2y + 1) \tag{3.27}$$

$$T_i(x, y + N_i/2) = T_i'(x, 2y) - T_i'(x, 2y + 1) \tag{3.28}$$

Here x and y are Cartesian coordinates defining pixel locations. Eqns. 3.25 to 3.28 essentially calculate the sum and differences between adjacent rows and columns of pixels. In figure 3.13 we show single tier wavelet transform on an image. Our wavelet transformed image, T_i, consist of 4 quadrants (here referred to as Q1-Q4). Q1 is a downscaled version of the original image, with the linear resolution reduced by a factor of two. Q2-Q4 represent images of the object at the same resolution as Q1, with vertical, horizontal and diagonal edges highlighted respectively, at the scale of the pixels sizes in the original low resolution image. We now use the identification of edges highlighted in T_i to guide where to make further measurements at higher resolution. We form image I_{edge}, which combines the highlighted edge information present in images Q2-Q4. I_{edge} is formed by calculating the pixel-by-pixel quadrature sum of Q2,Q3 and Q4 to create image:

$$I_{edge}(x, y) = \left[\sum_{j=2}^{j=4} Qj^2(x, y)\right]^{\frac{1}{2}} \tag{3.29}$$

We now create an image mask by binarising I_{edge} based on either a threshold value or by setting a required percentage of pixels to image at higher resolution. This mask defines which regions of the object we will sample at the next phase.

The next tier of imaging is performed by making a series of Hadamard projection measurements using a fully sampled set of patterns confined to the regions defined by the mask. Here the most common Sylvester Hadamard construction is no longer optimal, as the number of patterns (and therefore pixels) in the Sylvester Hadamard sets are confined to 2^k, where k is a non-negative integer, while the number of pixels within the next phase is unlikely to equal 2^k. Therefore we now use the Paley type-II Hadamard construction, which is of more flexible scale, since it can possess a number of patterns equal to $p + 1$, where p is a Prime number that is congruent to 3 (mod

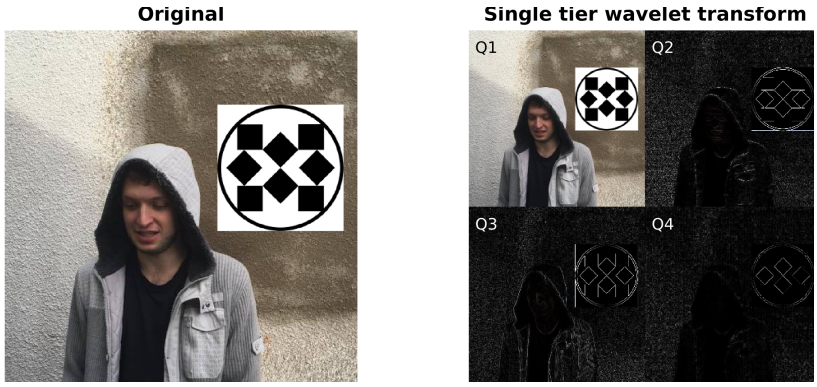

Figure 3.13: ***Left:*** *Picture of Rayko Stantchev.* ***Right:*** *Single tier Haar wavelet transform of image on the left. For the transform the wavelet coefficients (quadrants Q2-Q4) have been multiplied by 5 to improve contrast. Large wavelet values are shown as white and indicate regions with strong edges.*

4). Therefore we create the smallest Paley type-II Hadamard matrix which can be used to critically or slightly oversample the target area of the object defined by the mask, at twice the resolution of the initial low resolution initial image I_1. The fully sampled higher resolution image of the masked regions is once again reconstructed from a weighted sum of the Paley Type-II Hadamard patterns, each weighted by its measured correlation with the object.

Finally, image I_1 is upscaled by a factor of 2, and updated to I_2 by either replacing those parts of I_1 with the higher resolution information, or to make the best use of all measurements, we can combine both low and high resolution measurements by representing all our measurements as a matrix equation as shown in Eqn. (3.14), and solving for the image. In the second case, the newly imaged areas are now oversampled, and so a least squares fit provides a level of noise suppression. In the regions that have not been re-sampled at higher resolution we keep our initial low resolution measurements with uniform intensity across each larger scale pixel. Once I_2 is obtained, it is used as the input for the single tier Haar wavelet transform and the process is repeated at increasing resolutions. Evidently, as the algorithm progresses, the selection of new regions to image at higher resolutions is likely to be made inside regions that were imaged in the previous phase. This represents the truncation of the Wavelet tree, which is following the assumption that high values of wavelet coefficients at coarse scales are highly correlated with high values at finer scales. This is a reasonable assumption which can be understood by considering that sharp edges are represented by Fourier components across a wide range of frequencies.

Chapter 4

Imaging a sub-wavelength slit

Summary

In this chapter, we demonstrate that manipulating the THz near fields using photoconductivity is possible, and show this can be used to construct an image. By generating a pair of thin conducting stripes in a silicon wafer using structured illumination, we show that the near field interference pattern can be used to irradiate a sub-wavelength metallic slit. Further, by creating a constructive near field interference we bring about enhanced transmission through the slit. Then, by displacing this pattern in the direction perpendicular to a slit, we build a near field profile of this slit by recording the far field transmission of our THz pulses. This experiment demonstrates imaging capability of metallic features with a resolution of $\sim 60\mu$m ($\approx \lambda/4$). The main experimental idea is a shown in Figure 4.1.

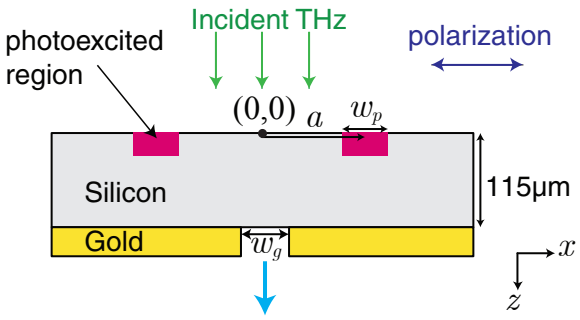

Figure 4.1: Schematic side view of a THz plane wave incident upon a silicon wafer with a single slit in a thin gold film on the exit side. The dark (pink) regions indicate the photoexcited conductive regions.

4.1 Theoretical Modelling

4.1.1 Scalar Diffraction Pattern

In order to investigate the dimensional dependence of the interference pattern generated by the two parallel stripes we use scalar diffraction theory. We approximate our photoexcited regions as a perfect electric conductor that is infinitely thin in the z direction, which is reasonable since the penetration depth of the incident pump beam (11μm for our 800nm light [78]) is much smaller than our THz wavelengths. Note that this approach ignores absorptive losses in the silicon plasma. To maximize transmission, polarization perpendicular to the slit is chosen.

We solve the Fresnel diffraction integral[1] [76]

$$U(x) = \frac{e^{ikz}}{i\lambda z}\int_{-\infty}^{\infty} U(\xi)e^{\frac{ik}{2z}(x-\xi)^2}d\xi \tag{4.1}$$

for the wavelengths inside silicon and then consider the resultant diffraction pattern at a distance equal to our silicon wafer thickness (115μm), where ξ runs parallel to x (Fig. 4.1) along the surface of the silicon and $U(\xi)$ describes the field distribution at this plane. The experimental geometry and choice of polarization allows us to define an electric field of amplitude zero at the boundary of the conducting region and unity everywhere else, which is described by the function

$$U(\xi) = 1 - \left(\text{rect}\left(\frac{\xi - a}{w_p}\right) + \text{rect}\left(\frac{\xi + a}{w_p}\right)\right), \tag{4.2}$$

where rect is the rectangle function, a is the stripe separation parameter (center to center distance is $2a$) and w_p is the stripe width as shown in Fig. 4.1.

Fig. 4.2a) shows how the normalized intensity, $|U(x)|^2$, at a point equidistant from the stripes ($x = 0$), in a parallel plane 115μm away, varies with frequency and a. For small stripe separations we see a minimum in the THz field. As the stripe separation is increased, we observe successive constructive and destructive interference maxima and minima. Each subsequent maxima occurs with lower intensity and shorter periods of a due to the increasing propagation distance. The other features criss-crossing these maxima and minima are dependent on the stripe width and hence are associated with the finite dimensions of the stripes.

[1] We use the numerical solvers built into Mathematica 9.

Although we now know which frequencies should be enhanced and diminished due to the near field interference from the waves scattered by our stripes, these Fresnel calculations can only serve as an initial guide to experiment and as an explanation of the underlying physics, since they do not account for the Fabry-Perot resonances within the silicon and they inadequately treat the evanescent fields.

4.1.2 Evanescent Contributions in Scalar Diffraction

To account for the evanescent near-fields, we modify the calculations in Ref. [77] (shown in §2.2.1) for our field distribution given by equation (4.2).

In Fig. 4.2b) we plot the normalized intensity, $|U(x)|^2$, as in a), but using the more rigorous considerations of Ref. [77] which take into account the evanescent fields. Comparing the two plots, we see agreement in the first maximum, however the separations between the subsequent maxima and minima are very different. The large number of maxima and minima in the Fresnel calculation in a) arise from the highly oscillatory Fresnel integrals, which are not present in the calculation of Fig. 4.2b) due to the more rigorous treatment of the near fields.

However, even this more rigorous calculation does not account for multiple scattering or the Fabry-Perot type resonances in the silicon, hence in the following section we describe a full wave solution to Maxwell's equations to account for all the relevant physics.

4.1.3 Method of Modal Matching

We develop a full wave modal matching solution in order to describe our system. Note that we omit the time (t) dependent components of the fields. We begin by splitting our sample into 5 regions with respect to z-axis, Fig. 4.3. Region I extends to the half space on the incident side the sample. Using the angular spectrum representation [76, 77] we have a normally incident plane wave and a reflected component that is a superposition of plane waves propagating away from the sample, written

$$E_{1x} = e^{i(0x+k_z(0)z)} + \int_{-\infty}^{\infty} R(u_x) e^{-ik_z(u_x)z} e^{iu_x x} \mathrm{d}u_x, \tag{4.3}$$

where u_x is the directional wavevector in x, $R(u_x)$ is a spectral amplitude function and $k_z(u_x) = \sqrt{k_0^2 - u_x^2}$. In the photoexcited space (region II) our fields are represented

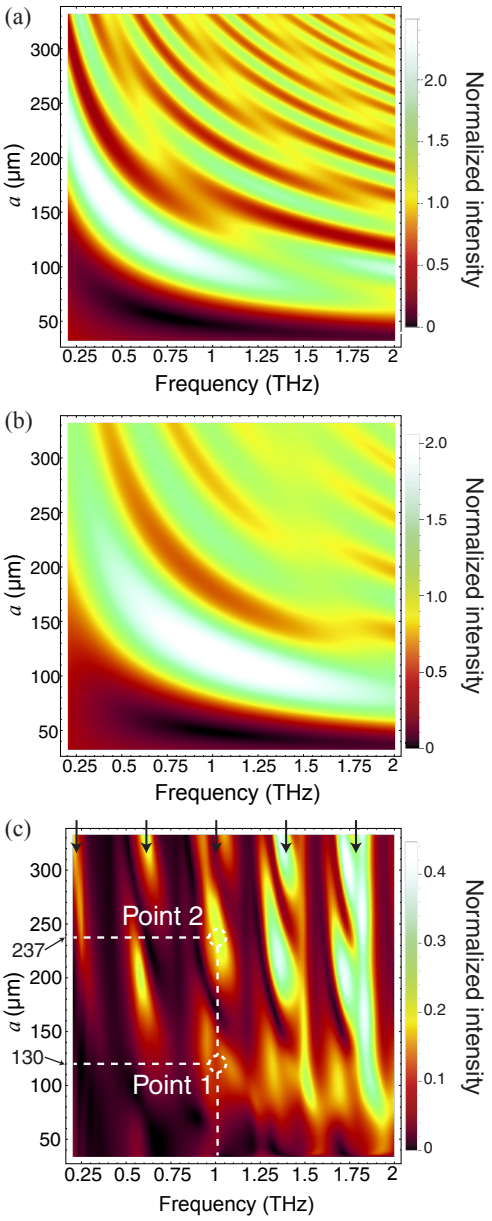

Figure 4.2: (a) Fresnel diffraction intensity distribution at $x = 0$ with varying stripe separation, a, as calculated at a distance of $z = 115\mu$m. (b) is the same diffraction pattern as part a), but including the homogeneous and evanescent contributions from Sec. 4.1.2. (c) is the absolute value of the propaging components at the exit side of our system squared, as calculated using the modal matching model in Sec. 4.1.3. The black arrows indicate the Fabry-Perot type resonances of the silicon. $w_p = 64\mu$m in all calculations. Note that the intensities in a) and b) are not comparable with c) because c) takes into account the transmittance of the slit as well as absorptive and reflective losses from the silicon which are neglected in the other two calculations.

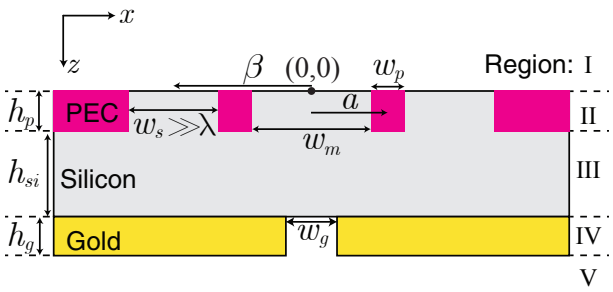

Figure 4.3: Schematic showing the variable definitions used in the modal matching calculations of Sec. 4.1.3. $h_p = 11\mu m$ is the penetration depth of our 800nm pump light [78], $h_{si} = 104\mu m$ is the thickness of our silicon wafer minus h_p, $h_g = 250nm$ is the thickness of our gold film. PEC stands for perfect electrical conductor.

by the modes of the cavity between the parallel conducting stripes. Since we choose polarization perpendicular to our stripes the electric field parallel to the conductor will be zero. Boundary conditions will thus dictate that the fundamental mode between our stripes is described by a rectangle function [1]. Unlike the Fresnel calculation, we are not able to directly take into account an expansion into an infinite x space, but instead approximate by considering one cavity in the middle and two on either side whose width tends to infinity in the final calculation [2]. This is written

$$E_{2x}^{(m)} = \left(P_1^{(m)} e^{iq_{si,z}z} - P_2^{(m)} e^{-iq_{si,z}z}\right) \text{rect}\left(\frac{x}{w_m}\right) \tag{4.4a}$$

$$E_{2x}^{(p)} = \left(P_1^{(p)} e^{iq_{si,z}z} - P_2^{(p)} e^{-iq_{si,z}z}\right) \text{rect}\left(\frac{x+\beta}{w_s}\right) \tag{4.4b}$$

$$E_{2x}^{(n)} = \left(P_1^{(n)} e^{iq_{si,z}z} - P_2^{(n)} e^{-iq_{si,z}z}\right) \text{rect}\left(\frac{x-\beta}{w_s}\right), \tag{4.4c}$$

where $q_{si,z} = n_{si}k_0$ is the wave vector inside the cavities, $w_m(w_s)$ is width of middle (side) cavity and β is the displacement parameter for the side cavities as shown in Fig. 4.3. The superscript in parentheses denotes the cavity (m is middle slit, p is for $+\beta$ and n is for $-\beta$). In the silicon (region III) we have two sets of plane wave

[1] For larger stripe separations, $\sim 200\mu$m, the cavity between our stripes becomes multimodal and thus our rectangle function description is an approximation. However, since the higher order modes are oscillatory, giving rise to a smaller overlap integral with the incident field, the fundamental mode will dominate even for larger stripe separations

[2] In the final calculation we add a small amount of loss ($n_{si} = 3.415 + 0.05i$) in the silicon to further eradicate any artefacts that may arise from the 3 slit approximation.

superpositions travelling in opposite z directions, written

$$E_{3x} = \int_{-\infty}^{\infty} S_1(u_x) e^{ik_{si,z}(u_x)z} e^{iu_x x} \mathrm{d}u_x - \int_{-\infty}^{\infty} S_2(u_x) e^{-ik_{si,z}(u_x)z} e^{iu_x x} \mathrm{d}u_x, \tag{4.5}$$

where $k_{si,z}(u_x) = \sqrt{(n_{si}k_0)^2 - u_x^2}$. In region IV we describe our fields in the lower cavity region with a variable displacement parameter b:

$$E_{4x} = \left(B_1 e^{iq_z z} - B_2 e^{-iq_z z}\right) \mathrm{rect}\left(\frac{x-b}{w_g}\right), \tag{4.6}$$

where q_z is the wavevector inside the cavity. Finally, in region V we have a transmitted component that is a superposition of plane waves propagating away from the sample in the positive z direction:

$$E_{5x} = \int_{-\infty}^{\infty} T(u_x) e^{ik_z(u_x)z} e^{iu_x x} \mathrm{d}u_x. \tag{4.7}$$

All E_y components are zero due to sample geometry and choice of incident polarization. From the free space Maxwell's equations $\nabla \cdot \mathbf{E} = 0$ and $\nabla \times \mathbf{E} = -\mu_0 \partial \mathbf{H}/\partial t$ we obtain the z electric field components, and also the subsequent expressions for the magnetic $\mathbf{H}$-fields.

These equations are then solved in the same reasoning as those solved in §2.2.2.

In Fig. 4.2c) we plot the square of the absolute value of the electric field in region V given by eq. (4.7), taking into account only propagating field components integrated over our slit width i.e. u_x varies between $-k_0$ and k_0 (for values where $|u_x| > k_0$, $k_z = \sqrt{k_0^2 - u_x^2}$ is imaginary and thus the waves become evanescent and not measurable by our experiment). This gives the transmitted intensity in the far field normalized by the incident field intensity. The downward pointing arrows in Fig. 4.2c) show the maxima due to the Fabry-Perot type resonances within the silicon. The increase in transmitted components with increasing frequency (decreasing wavelength) is expected for the transmittance through a sub-wavelength slit. For small stripe separations, a, the transmission through the slit is minimal. With increasing a, we start to see the Fabry-Perot interferences in the silicon as well as the near field interference due to scattering from the conducting stripes. Strong maxima occur when these two interference conditions coincide.

Comparing all models in Figure 4.2, we see that to obtain the constructive inter-

ference conditions it is absolutely essential to carry out the full wave solution in c). These interference conditions depend on the wafer thickness (115μm in our case) and will have to be recalculated should the thickness be changed. Note, the first order interference condition marked at point 1 will result in a relatively simple field pattern, while the higher order condition marked by point 2 will give a more complex field distribution. We return to this later.

4.2 Experimental Setup and Sample fabrication

An 800nm (90fs) Ti-Sapphire femtosecond laser is used to generate our THz pulses using optical rectification in a ZnTe crystal §3.1.2.1. The 800nm pulses also provide the pump excitation beam for the silicon wafer. Our experiment is illustrated in Fig. 4.4, where a pump pulse is spatially modulated via a digital micromirror device (DLP3000 with the DLP Lightcrafter from Texas Instruments) so as to project a pair of thin lines on the surface of the silicon sample, and coordinated with a collimated THz beam. The THz transmitted through the sample is gathered and measured using electro-optic sampling in a second ZnTe crystal §3.1.2.2. The lateral position of the stripes is controlled with a precision of $18\mu m$, which is set by the magnification of our pump beam optics and the dimensions of the individual micromirrors.

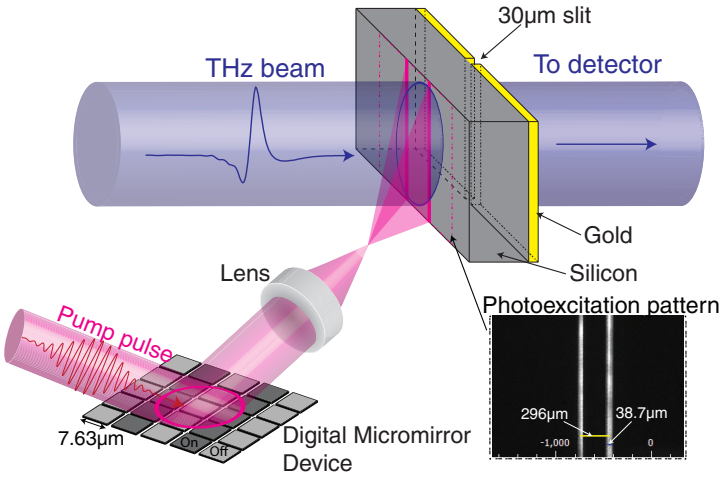

Figure 4.4: Experimental setup. A pump pulse is spatially modulated so as to project a pair of thin lines on the surface of the silicon sample, coordinated with the THz beam path through the 30μm slit. The spatially modulated intensity pattern of the pump beam, measured at the plane of the sample, is shown as recorded by a beam profiler.

For the sample, a $115\mu m$ thick $1000\Omega \cdot cm$ silicon wafer has a $250nm$ thin gold film deposited via thermal evaporation on one side. A $5nm$ layer of chrome acts as the adhesion agent between the silicon and the gold. A $30\mu m$ wide slit is wet etched in the gold layer using a photolithographic mask.

4.3 Results & Discussion

In experiment, we measure the electric field of the THz pulses in the time domain, Fig. 4.5a). The solid line shows the electric field transmitted through our sample. After an initial signal at $\sim 2ps$, representative of our incident pulse, we see a number of repeating signals at $\sim 4.5ps$ & $\sim 7.5ps$ which represent the Fabry-Perot type interferences within our silicon wafer. The dashed line shows the transmitted field measured after the photoexcitation of the silicon wafer, using homogeneous (unpatterned) 800nm $92\mu J/cm^2$ pulses. This energy is enough to significantly alter the conductivity of the silicon, effectively turning it into a conductor §3.3 and reducing the field transmission by $\approx 85\%$. The solid dotted line shows the change in transmission, $\Delta E = E_{mod} - E_{ref}$.

In Fig. 4.5b) we plot $\Delta E(t)$ when the photoexcitation pattern takes the form of two conducting stripes with a fixed center to center separation distance of $468\mu m$ ($a = 234\mu m$). The horizontal axis represents the displacement of the two photoexcited lines along the surface of the silicon. The reference signal in part a) is also plotted on the left of the greyscale plot. There are three main features in this graph. For displacement values around $200\mu m$ and $675\mu m$, we essentially see the negative of the reference signal. This corresponds to a large decrease in THz signal arising from shadowing due to a photoexcited line situated directly above our slit. From these two features, diagonal lines arise due to the scattering of our stripes. These lines then intersect at $450\mu m$, when the stripes are symmetrically placed with respect to the slit. At this point we observe additional features in the transmitted field due to the interferences of the scattered fields.

In order to distinguish the frequency dependence of the interferences, we take the Fourier transforms of the measured fields at each individual displacement value. Note that an increase in transmission occurs when the absolute value of the modulated signal divided by the reference is greater than one ie. $|E_{mod}/E_{ref}| > 1$. For a decrease in transmission, one observes $|E_{mod}/E_{ref}| < 1$. In Fig. 4.6 we compare the frequency

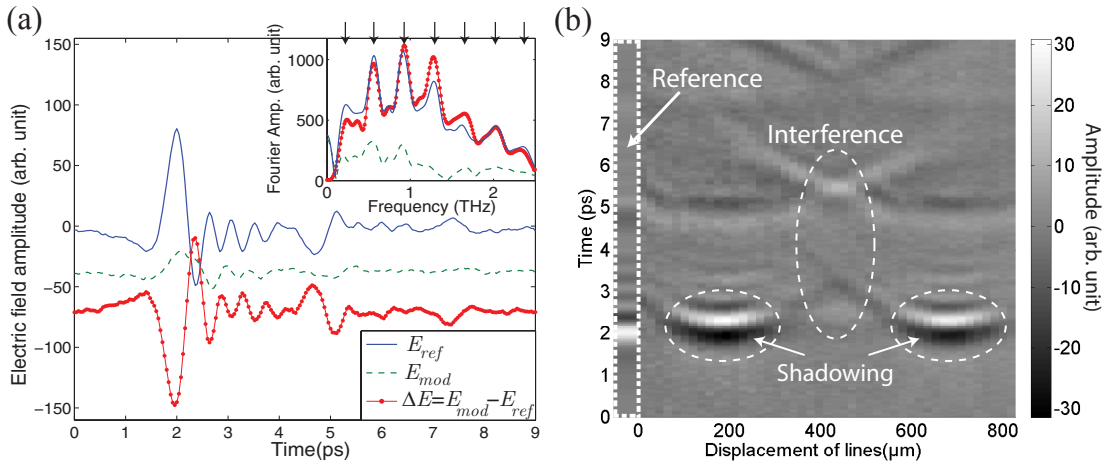

Figure 4.5: (a) THz Pulses detected through our slit measured in the time-domain. Solid line is the reference signal, dashed line is the signal when the entire silicon surface is photo-modulated and dotted solid line is the differential signal ie. the difference between the other two. Note that the data has been offset for visual purposes. Fourier spectrums of the pulses are given in the inset, with Fabry-Perot type resonances indicated by downward pointing arrows. (b) Differential time signal when a pair of 72μm photoexcited lines are displaced along the surface of the silicon with a center to center separation of $468\mu m$ ($a = 234\mu m$). The reference signal is highlighted by dashed rectangle.

spectra measured in experiment to those predicted by our modal matching calculations, corresponding to points 1 and 2 in Fig. 4.2c). Note that the model assumes perfectly defined conductive regions, whereas the experimentally photoexcited stripe edges are blurred by the diffraction[1]. Furthermore, our model neglects absorption within the photoexcited plasma, which results in lower transmission in experiment, and higher order modes within the cavities of region II in Fig. 4.3. Nevertheless, we still detect clear enhancements in transmission corresponding to the constructive interference conditions. We also see that for large stripe separations (a=234μm) one observes multiple interference fringes, while for small stripe separations (a=126μm) we see a single interference fringe.

In Figure 4.7 we take a horizontal slice through Fig. 4.6 at a single frequency of $f = 1.05$THz (the Fabry-Perot resonance nearest the central frequency of our free space pulses). This signal is a convolution between the scattered field and the slit width, and so is essentially a THz image. We look at our resolution with two definitions. First, we look at the steepness of the edge. Using the 90%-10% criterion

[1]The Rayleigh resolution criterion of our optics is $5.3\mu m$

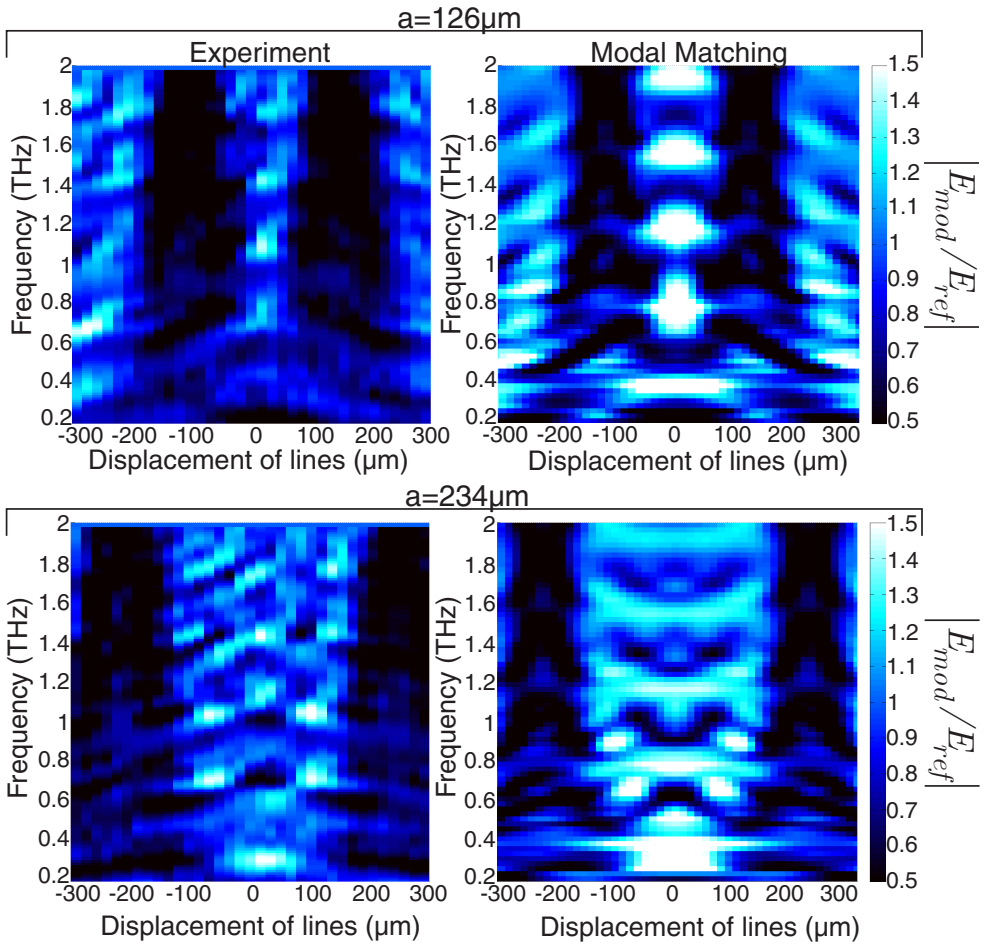

Figure 4.6: Comparison plots of the absolute value of the modulated signal divided by the reference $|E_{mod}/E_{ref}|$. Any value above 1 corresponds to enhanced transmission at that frequency. Top: $a = 126\mu$m Bottom: $a = 234\mu$m, with experiment on the left and modal matching on the right.

we obtain a resolution of $47.8\mu m$. Second, we look at the full width half maximum of our peak. Here we find a resolution of $65.7\mu m$. Since both definitions give numbers smaller than our free space wavelengths we have sub-wavelength resolution: for a=126μm at $\lambda_0 = 285\mu$m the full width half maximum is $\sim\lambda/4$ (note that the image resolution will be dependent on the wavelength, but we choose 285μm as the dominant wavelength in our spectral transmission). This resolving power is due to a narrow field confinement for the Point 1 condition in Fig. 4.2c). If one selects a much larger stripe separation of a=234μm (Point 2), the complex interference leads to a much more complex field pattern, and sub-wavelength imaging is not possible. This highlights the requirement for a single interference fringe.

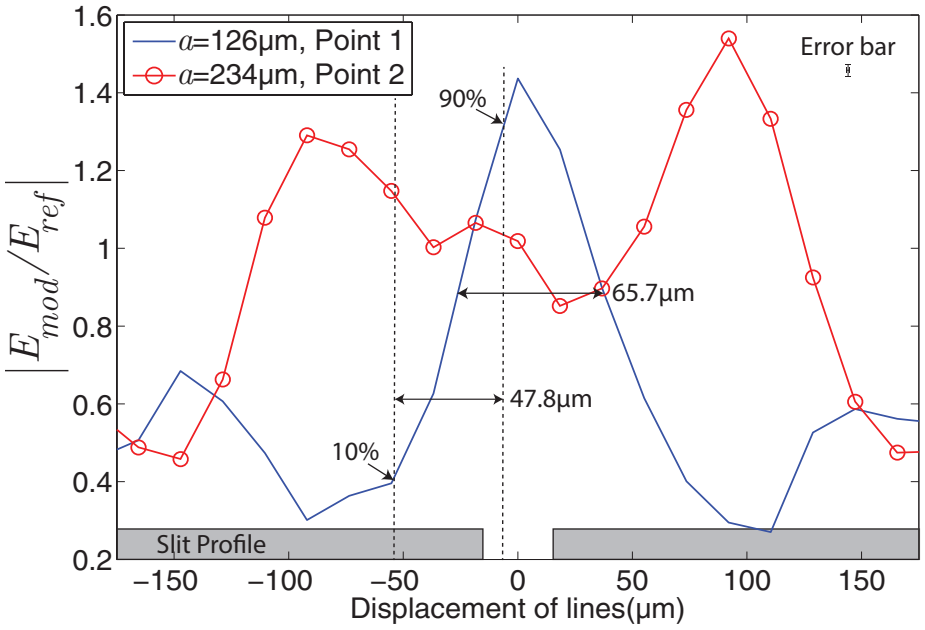

Figure 4.7: Absolute value of the modulated transmission divided by the reference signal as a function of stripe displacement at $f = 1.05\,THz$ ($\lambda_0 = 285\mu m$) for two different stripe separation values. Error bar is shown in top-right corner

4.4 Conclusions

By photoexciting and modelling a pair of line scatterers, we show that optically induced conduction in semiconductors can enhance THz transmission through a sub-wavelength slit. More over, we demonstrate that this same phenomenon can be used to obtain a profile of the same slit with $\lambda/4$ resolution. Our technique is completely non-invasive, unlike conventional near-field scanning microscopy. It is interesting to note that the upper limit for resolution in this technique is set by the optical pattern. Therefore, if engineering challenges can be overcome, one could in principal achieve a THz image with resolution at the optical diffraction limit.

Chapter 5

Photomodulator thickness and polarization

The first part of this chapter demonstrates how the resolution is affected by diffraction caused by the THz propagating through the photomodulator. The second part shows polarization effects and the possibility of using of polarization to detect subwavelength objects through a silicon wafer.

5.1 Imaging technique

Our imaging set up is illustrated in figure 5.1. A more detailed schematic is shown in figure 3.1 along with our THz pulses (0.2 - 2THz). A THz pulses is generated via optical rectification in ZnTe, see §3.1.2.1. To spatially modulate our THz beam, we shine a coincident $800nm$, $100fs$ pump pulse onto a highly resistive silicon wafer. The pump pulse itself is structured into binary spatial intensity patterns by a standard digital micromirror device [101]. When these patterns are projected onto the silicon wafer, the photoexcited regions are rendered conductive (see §3.3) and thus also opaque to the coincident THz radiation [74]. Moreover, because we record the THz transmission immediately following photoexcitation, before processes such as electron diffusion take place (see §3.3), the spatial pattern encoded in the $800nm$ pulse is directly transferred to the THz pulse without smearing or broadening of spatial features. The patterned THz pulse then propagates through the silicon before interacting with a sample positioned on the hidden side of the wafer, after which we record the far-field transmission with our ZnTe detector (see §3.1.2.2). As explained

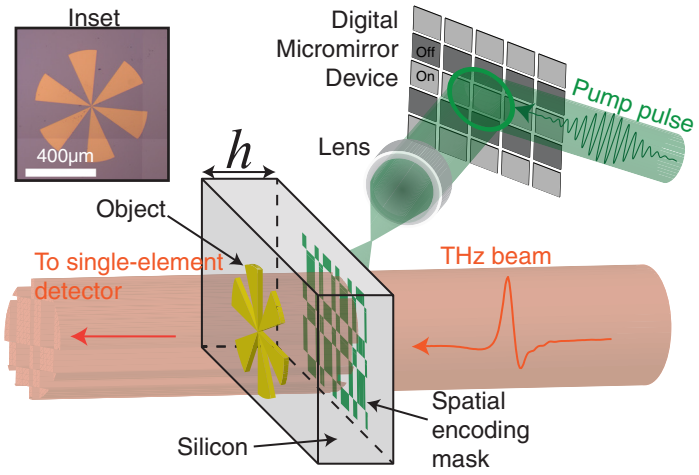

Figure 5.1: Illustration of imaging setup: using a digital micromirror device and a lens, a pump pulse is spatially structured and projected onto a silicon wafer. This spatially modulates a coincident THz pulse. This THz pulse then passes through an object and measured on a single-element THz detector. Inset is an optical image of a resolution test target (cartwheel) manufactured from gold on a 6μm thick silicon wafer.

in §3.4, by spatially encoding a beam of THz radiation with binary intensity patterns, an image can be formed by analyzing the THz radiation transmitted or scattered by an object using a single pixel detector [92, 95] (see §3.4).

5.1.1 Image formation example

Here we show a typical set of measurements made in our system to form an image with a Hadamard encoding scheme (§3.4.2.2). Consider a spatially encoded beam of radiation incident upon an object with some spatial transmission profile. The total transmitted light will be the dot product of the object and the encoding mask. Our single-element detector measures this total transmitted light. These measurements for different Hadamard masks are shown in the bottom panel of fig. 5.2, where the vertical axis is our detector readout and mask number is along the horizontal axis (we show the first 500 masks of out the 4096). Here, we also show six Hadamard masks above the right hand-side of the signal plot, where white and black are values of 1 and -1 respectively. After we have completed our measurements for the full set of 4096 masks, we can perform an inverse Hadamard transform to obtain an image of our object. This image is shown above the left hand-side of the signals plot.

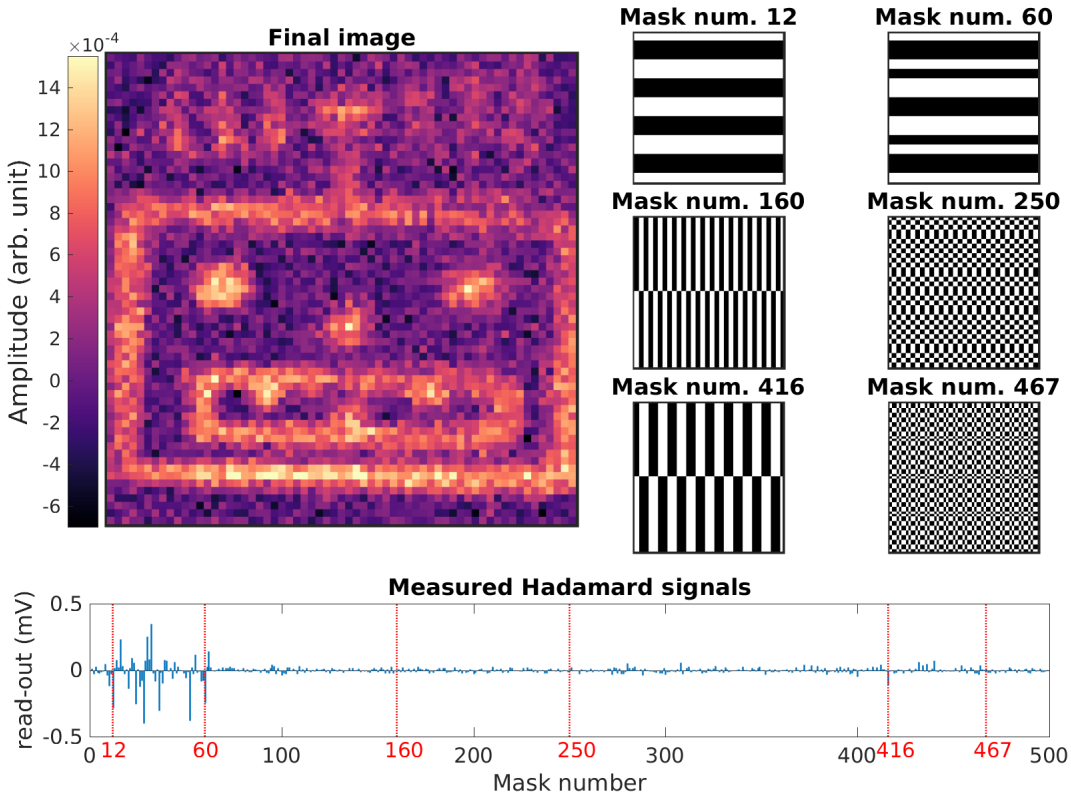

Figure 5.2: ***Hadamard Signals:*** *Top left panel, a* 64×64 *image taken in our system using Hadamard transform imaging. On the right are six Hadamard encoding masks (obtained via the Sylvester construction §3.4.2.2) used in the measurement of the image. Bottom graph shows the first 500 signals measured in experiment. The red dashed lines show the number of the example Hadamard masks.*

5.2 Resolution and photomodulator thickness

In near field imaging approaches, subwavelength resolution can be achieved due to the presence of near fields in the interaction with the object. However, near fields decay exponentially with distance. Furthermore, the propagating fields diffract as they propagate further decreasing resolution. In figure 5.3 we plot the diffraction pattern of a single stripe scatterer ($40\mu m$ wide) at different distances from the stripe. We use the mathematics in §2.2.1 at a single frequency $(1THz)$ for a world filled with a refractive index of 3.42. Here it can be seen that the shadow cast by the stripe widens as the light propagates further away from the stripe. One can also see that the shadow decrease in amplitude contrast. For imaging, this results says the closer you can get to the object the better resolution you can obtain.

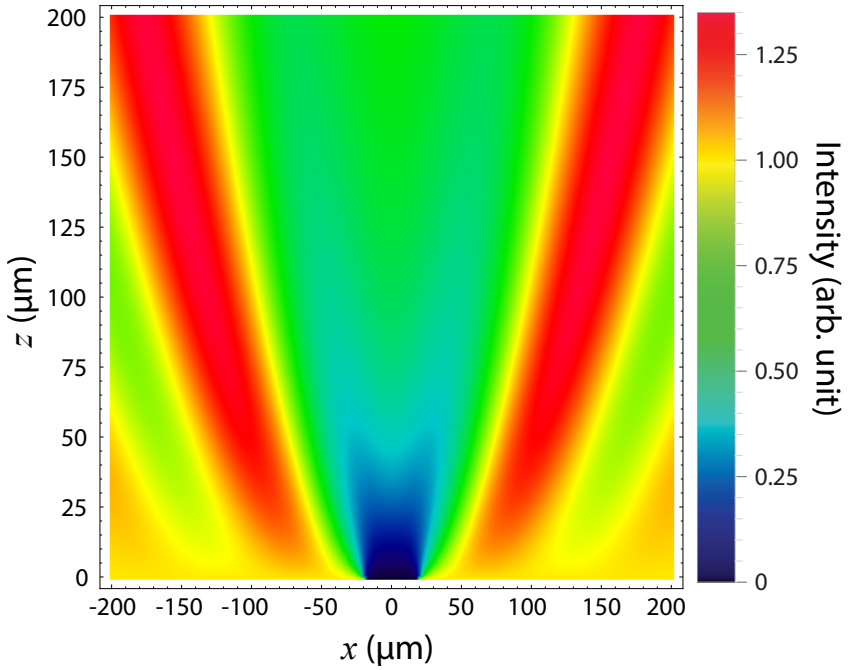

Figure 5.3: Diffraction pattern from a single stripe of width $40\mu m$. Intensity distribution (horizontal axis) from the stripe as it is propagated further away from the stripe (vertical axis). We plot the sum total intensity at a single frequency ($1THz$) for a world filled a refractive index of 3.42 (that of silicon at THz frequencies). Refer to §2.2.1 for mathematical details.

5.2.1 Resolution in our system

In our approach, the thickness of the modulator sets a practical limit to how close we can get to our object. Therefore, it can be expected to play an important role in determining the ultimate resolution of our THz images. To investigate this, this we image a subwavelength sized, metallic resolution target through a silicon photomodulator of varying thickness h. Our resolution target is a metallic cartwheel, shown in inset of fig. 5.1. We pick a cartwheel pattern since it contains an increasing amount of spatial frequencies towards its center. This allows us to estimate a resolution as follows; if one blurs this pattern, the individual cartwheel arms in the center will merge together becoming indistinguishable from one another. However, the arms at the edges will be discernible from each other (provided the blurring is not too great). Thus, there will be a point between the center and the edge where cartwheel arms become distinguishable. By denoting the distance between the arms at this point, one obtains an estimate for the resolution.

In Fig. 5.4 we show our THz images taken through silicon wafers of thickness h=400, 110 and 6μm. For a relatively thick modulator (h=400 μm, of the order of the THz wavelength), we see that very few of the subwavelength features of the cartwheel are evident in the resulting image (see fig. 5.4a). One can understand the resulting image by considering the diffracted field expected for the object when propagated through a thickness h of silicon (refractive index = 3.42), plotted in figure 5.4d using scalar diffraction theory [77] (see §2.2.1 for details). While agreement is imperfect (discussed in the next paragraph), we see similar blurring to the cartwheel edges, particularly for the high spatial frequency components towards the centre of the cartwheel, completely distorting the final image. If we reduce the thickness of the photomodulator to 110 μm, we obtain the images of figs. 5.4b and 5.4e. We see an image resembling a cartwheel, with only the centre of the image being distorted. Only when we reduce the thickness of the modulator to 6 μm do we finally recover a reasonably complete image of the cartwheel, see figs. 5.4c and 5.4f. The overall trend here is clear: as the thickness of the modulator is reduced, the images sharpen. Hence, due to the varying spatial frequencies of the cartwheel, as discussed in the previous paragraph, we can estimate our obtained resolution by evaluating the minimal distance for which the cartwheel arms are distinguishable. This leads to resolution values of 154 μm, 100 μm and 9 (± 4) μm for h = 400 μm, 110 μm and 6 μm, respectively.

We note that there are two main reasons for the discrepancies between the top and bottom rows of fig. 5.4. Firstly, the polarization of the THz field is important, while our scalar diffraction calculations neglect this. This leads to the breaking of rotational symmetry in the experimental images. Indeed, the effect of polarization can be observed explicitly when we vary the orientation of certain objects (see next section). Secondly, our model assumes an infinitely thin conducting sheet, where as in experiment the optical pump light has a finite penetration depth in silicon of 12μm for our 800nm pump light [78]. Whilst an infinitely thin sheet is reasonable for the low-frequency components our THz pulses, it not justifiable for most of our spectrum due to the large silicon refractive index (n=3.42 [73]). Therefore, the pump light will influence the diffracted field. Importantly, this effect sets a practical limit in terms operational efficiency. This is because reducing the modulator thickness further would cause leakage of the optical pump and reduce the modulation efficiency. Thus investigations with direct bandgap photo-modulators are required in order to

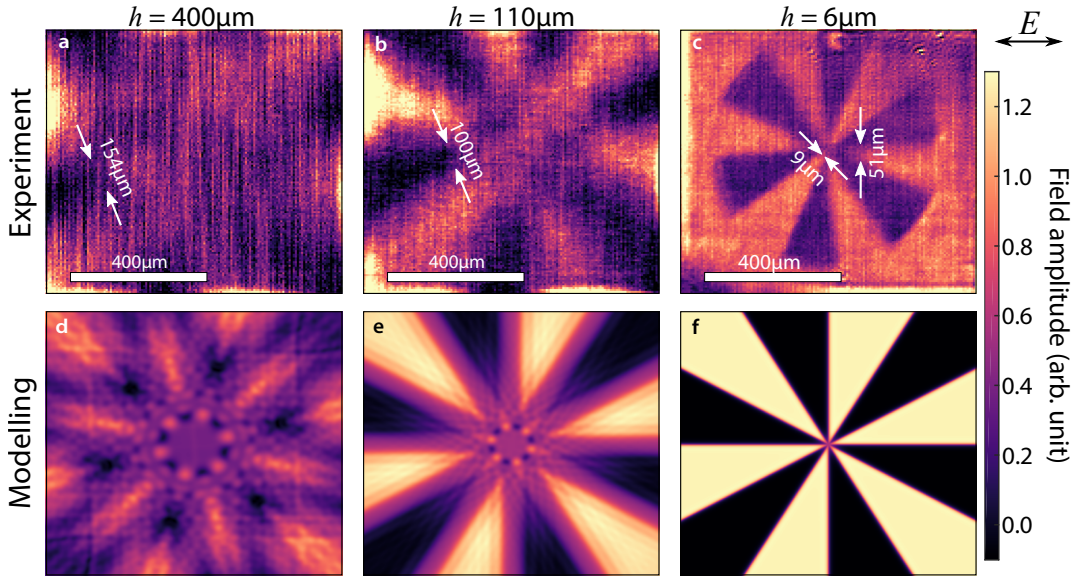

Figure 5.4: ***a, b, c:*** *THz images (horizontal polarization) of the cartwheel shown in inset of Fig. 5.1 taken through* $400, 110, 6\mu m$ *thick silicon wafers respectively. Note, the cartwheels in* ***a, b*** *have diameters larger than the field of view. Further, the origin of the vertical lines in* ***a*** *is discussed later.* ***d, e, f:*** *Calculated diffracted fields of a cartwheel as propagated through* $400, 110, 6\mu m$ *thicknesses of silicon respectively.*

improve the THz image resolution. Further, direct band-gap semiconductors have shorter carrier-lifetimes, therefore allowing for quicker repetition rate lasers to used thus improving the acquisition rate. However, the ultimate resolution limit in this technique is the pump-light diffraction limit. Therefore, using shorter wavelength pump light is perhaps more desirable since penetration depth in silicon decreases with smaller wavelengths.

Origin of vertical lines in Fig 5.4a

We begin with an empirical observation of how to eradicate the vertical lines. Moving the silicon wafer out our lens focus increases the amplitude of the vertical lines. This was first observed in the $6\mu m$ thick Si wafer, with the results shown in Fig. 5.5. Here, the cartwheel pattern is moved out of focus in the top row going left to right. Strong vertical lines appear as one of moves out of focus. The bottom row are the first 350 measurements of the corresponding image above. It can be seen that the out of focus image contains periodically occurring masks with abnormally high values. We now proceed to explain these preliminary observations.

Consider imaging a perfectly homogeneous beam with Hadamard multiplexing [1]. The first mask has values of +1 everywhere, ie. every pixel is turned on. Therefore this mask will measure to the total light transmitted through our object. However, every other mask has equal numbers of +1s as -1s. Since we are imaging a perfectly homogeneous beam, these masks will have a detector readout of zero. However, due to projecting these patterns with a $+5cm$ lens, some $+ve$ and $-ve$ mask pairs might not be perfect inverses of each other. These mask pairs will have a reading on the detector. The strength of the value will depend on how well the mask pair cancel each other. For more out of focus projections we expect the cancellation to be less efficient. Hence, why the signals in the out of focus image have the largest values. Finally, we believe these masks occur in a periodic manner due to the Paley type-I Hadamard sampling matrix, namely in that it uses a cyclical permutation in its method of construction.

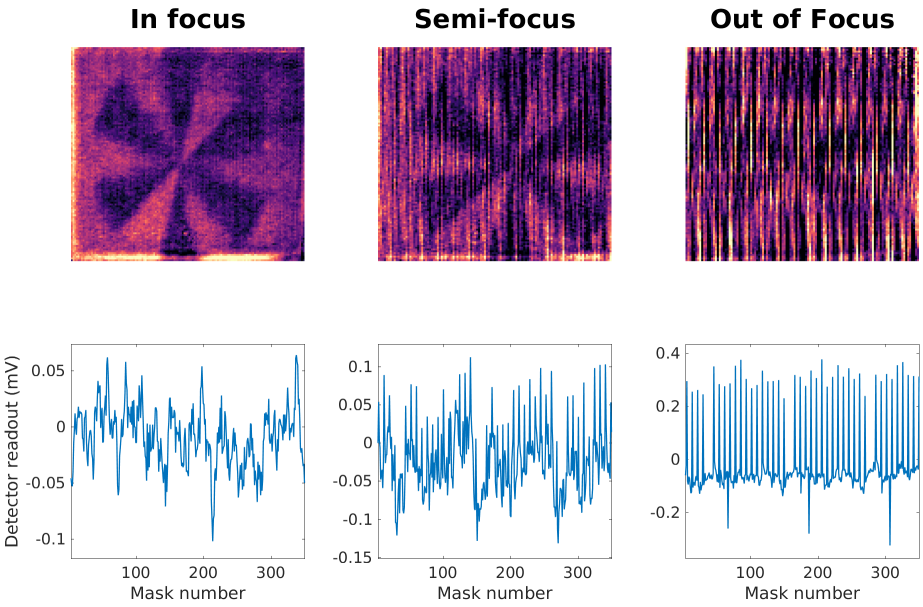

Figure 5.5: Left to right; THz images of the cartwheel as the silicon wafer is moved out of the focus of our projection lens. Top row are the images with the corresponding Hadamard signals below. Semi-focus (Out of focus) is defined as when the object is moved by ∼40(80)μm out of the focal plane.

[1] The same method that was used to obtain the images in Figs. 5.4**a-c**

5.3 Polarization

Our THz source is linearly polarized, thus we can expect effects due to the polarization boundary conditions (stated in §2.1.0.1). In particular, the electric field inside a perfect electrical conductor (PEC) is zero, §2.5 of ref. [102], therefore the electric field component parallel to the interface of the conductor must approach zero as well. In order to contemplate polarization effects on imaging, we consider the field distributions inside a slit in a PEC sheet for electric fields polarized parallel, $E_{\parallel}$, and perpendicular, $E_{\perp}$, to the conducting interface as illustrated in fig. 5.6. If the slit width is $\lambda/4$, then $E_{\parallel}$ can not satisfy the boundary conditions with a propagating solution[1]. On the contrary, $E_{\perp}$ can provide propagating solution of $\mathrm{rect}(\frac{x}{\lambda/4})$. This is because the only the field component parallel to the conductor, which for $E_{\perp}$ is always non-existent, needs to go to zero at the conducting interface. The first propagating solution for $E_{\parallel}$ is found when the slit width is $\lambda/2$. Then one can fit half a wavelength causing the electric field to go to zero at the boundary. Increasing the slit width increases the number of solutions satisfying the polarization boundary conditions. Therefore, polarization effects are particularly prominent in subwavelength sized conductive features.

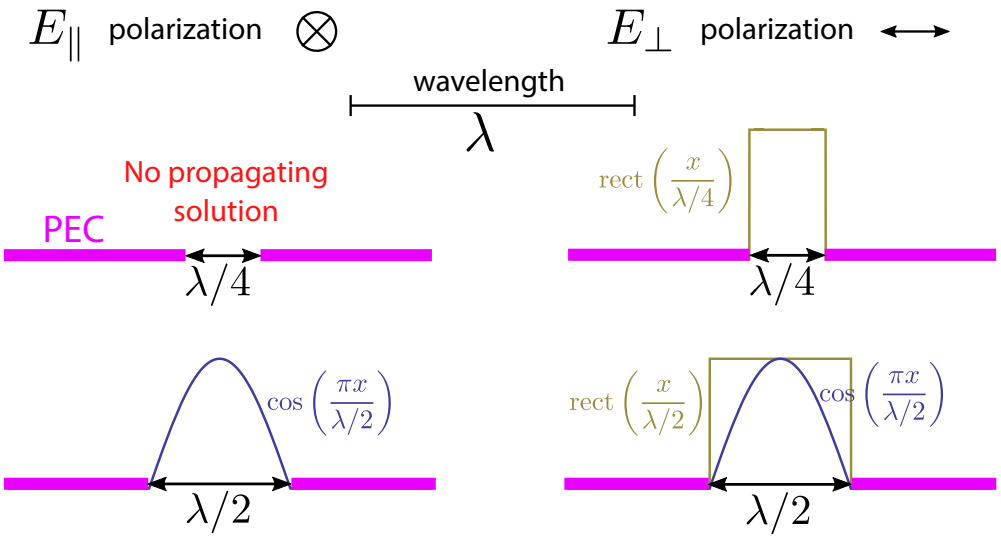

Figure 5.6: Schematic of the electric field distributions allowed for slits (going into the page) in a PEC sheet with varying slit size. Left hand side is for an electric field polarized into the page. Right hand side the electric field polarized horizontally in the plane of the page. PEC sheet is indicated by the purple colour.

[1] From waveguide theory, the electric field frequency is below the aperture cut-off frequency.

5.3.1 Experimental results

Our images contain conductive features smaller than the wavelength. In Fig. 5.4**c** one can argue that we observe a lower resolution, of 51 μm, depending on which cartwheel arms one evaluates. This effect arises from polarization boundary conditions. Namely, geometry does not render the electric-field component parallel to the to interface of a conductor to be zero, hence the reduction of transmission adjacent to the conductor. This effect can be better seen when imaging a sub-wavelength triangle with two perpendicular polarizations. This is shown in figs. 5.7**b** and 5.7**c**: the lines perpendicular to the polarization show larger transmission for the reasons discussed in the previous section.

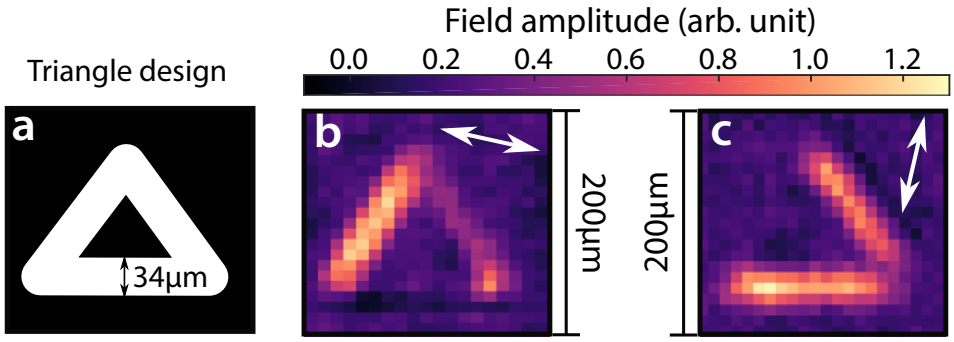

Figure 5.7: ***a:*** *Triangle design, white is transmissive and black opaque.* ***b, c:*** *THz images of a sub-wavelength triangle in* ***a*** *manufactured on 6μm thick Si wafer with horizontal and vertical polarization respectively.*

To further investigate polarization effects, on the exit side of a $115\mu m$ thick silicon wafer we manufactured a circuit board with the design shown in fig. 5.8**a** (the thickness of the conducting wires is 50μm and the separation between the individual wires at some locations is 30μm). In Fig. 5.8**b** we show a THz image of the circuit board in 5.8**a** as measured with vertical THz polarization. We see that the subwavelength conducting wires are more clearly observed when the THz radiation is parallel to the wires. The biggest difference is seen in the conducting tracks emerging from the large 500μm square in the bottom left corner, figs. 5.8**c** and **d**. Here, the small separation of the wires resembles a wire grid polarizer, with the transmission lowest (and image contrast highest) when the polarization is parallel to the wires. While such effects may be seen as a disadvantage, for example by limiting the resolving capacity for some metallic features, we discuss below how one can use polarization

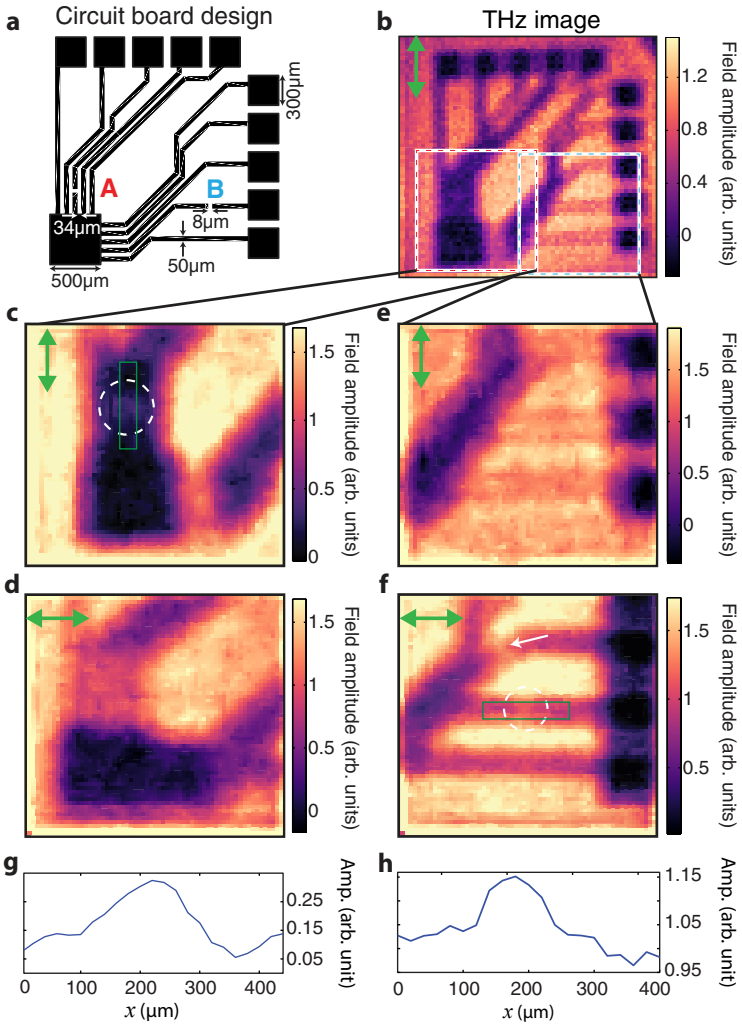

Figure 5.8: ***a****, The circuit board design, where black indicates conducting, metallic regions. 8μm breaks are marked by the letters A and B.* ***b*** *64×64 THz image of circuit board in* ***a*** *with vertical polarization. Pixels are 40μm. We see that the contrast of each of the individual wires in the circuit depends on the THz polarization, with the highest contrast seen for polarization parallel to the wires.* ***c****-****f****, 64 × 64 images of the square regions in part* ***b****. Polarization is shown by the green arrow in the top left corner of each picture. Pixel size is 20μm, and images have been denoised using the algorithm in ref. [103]. The subwavelength breaks (marked by circles in parts* ***c*** *and* ***f****) give rise to transmissive regions in the THz image when the THz polarization is parallel to the wire. In* ***f****, the diagonally orientated wire (indicated by the white arrow) also shows low contrast. Every image has been obtained via a full set of Hadamard masks.* ***g*** *(****h****), Line plot through the 8μm gaps in part* ***c*** *(****f****) with amplitude and space on the vertical and horizontal axis respectively. The spatial co-ordinates of the plot is indicated by the green rectangle in part* ***c*** *(****f****).*

sensitivity to our advantage by employing it to detect very subwavelength features. To this end, we have introduced very small ($\leq 8\mu m$) fissures in wires at two points marked by A and B in circuit diagram in Fig. 5.8**a**. In Figs. 5.8**c** and **f**, these fissures appear as marked increases in the THz transmission amplitudes at the points identified by dashed circles. Note that, in order to better distinguish these subwavelength features, Figs 5.8**c**-**f** have been denoised using the algorithm outlined in ref. [103]. It should be noted that the observed increase in THz transmission is considerably larger than one would expect solely from the reduced coverage of gold, and arises from a relaxation in the parallel field boundary condition due to the presence of the fissure. The subwavelength fissures are not visible when the polarization is perpendicular to the wires, as shown in Figs. 5.8**d** and **e**. One can therefore not only identify the orientation of the wiring using our approach, but also detect extremely subwavelength defects in circuitry hidden beneath optically opaque silicon.

5.3.2 Photoexcited gratings

The Hadamard masks constructed from the Sylvester construction technique (§3.4.2.2) have structures alike periodic gratings, as can be seen in the example masks shown in fig. 5.2. Further more, the field of view in many of our images is around $1mm$. This means that masks can appear like a diffraction grating with pitch anywhere from $10\mu m$ to $400\mu m$. This fact combined with the broad frequency spectrum of our THz pulses (fig. 3.2) implies that some masks are expected to have a resonant feature somewhere in our spectrum due to the periodicity[1] of the masks.

In order to investigate how the apparent periodicity of the different Hadamard masks affects our measured signals, on a silicon wafer ($1000\Omega \cdot cm$ resist, $115\mu m$ thick) we photoexcite diffraction gratings (energy per pulse $120\mu J/cm^2$) aligned perpendicular and parallel to our THz radiation with varying pitch and a half fill factor. Our raw temporal measurement of the transmitted waveforms is shown in fig. 5.9. Here on the horizontal and vertical axis we have grating pitch and time respectively with the colourscale indicating the electric-field strength of the transmitted waveform. On the left of the colourmaps we show the measurement for a homogeneous excitation profile (highlighted by the green rectangle). At $3.5ps$ one can see the main THz pulse arriving, then at $6.2, 9.1$ and $11.5ps$ one can see the first, second and third Fabry-Perot pulses respectively. As the pitch is increased one observes an increase

[1] The most masks are not actually strictly periodic gratings, however they are quite close.

in the field-strength of the main THz pulse. We return to this point later. Another interesting result is the fact that the small pitches (below 60μm) give signals of similar size to the homogeneous excitation profile despite decreasing the total excitation power by half[1] Whilst interesting, we are concerned with the frequency response of the system.

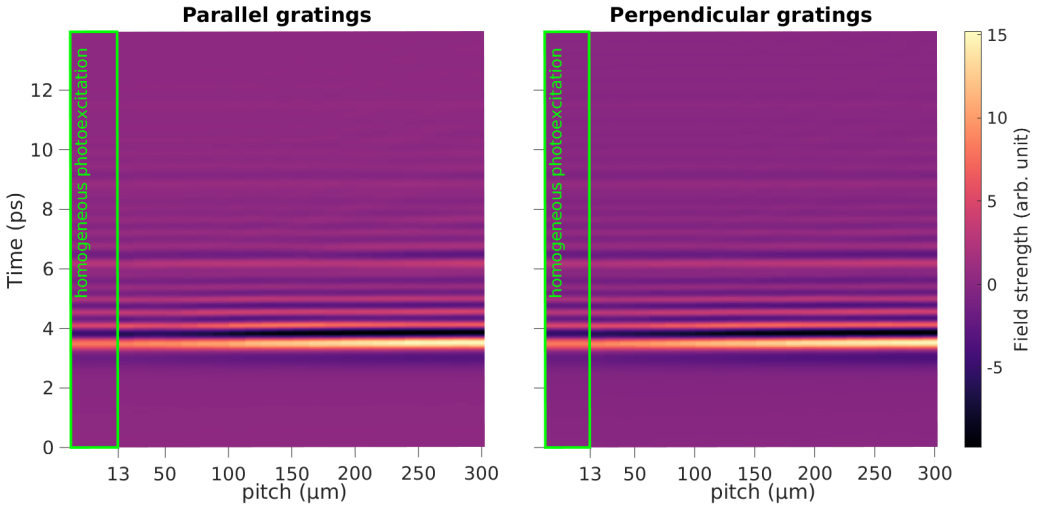

Figure 5.9: THz fields transmitted through gratings (50% fill fraction) photoexcited on a 115μm thick silicon wafer. Time and pitch on the vertical and horizontal axis respectively. The left (right) plot is when the gratings are aligned parallel (perpendicular) to the incoming THz radiation. On the left of each plot is a green rectangle, this is the field transmitted through our system when the photo-excitation profile is homogeneous.

In figure 5.10 we plot the Fourier spectrum of the pulses transmitted through the various gratings normalized to the homogeneous excitation response. The most obvious features are the horizontal lines appearing at 0.59, 0.95, 1.29, 1.66, 2.05 and 2.4THz. These coincide with the minima of the Fabry-Perot resonances in our 115μm thick silicon wafer. It can be seen that the parallel gratings are more transmissive than the perpendicular gratings for frequencies between 1.5 and 0.5THz and pitches greater than 150μm. Note that the biggest enhancements are observed at the Fabry-Perot minima. This is because the presence of the gratings modifies the boundary conditions. Namely, more evanescent field components are expected in the parallel gratings due to the orientation, for reasons similar to those mentioned in beginning

[1]The power within each photoexcited region is 120$\mu J/cm^2$ per pulse, however since the gratings have a 50% fill fraction the total power incident onto the entire silicon wafer is halved.

of §5.3. As the cavity size is increased, compared to the wavelength, the evanescent fields will decrease and thus reduce their effects on the boundary conditions. This is why the parallel and perpendicular gratings have very similar values around $2.2THz$. A frequency dependent feature can be observed just below the $\lambda_{si} = 2a$ line for both grating orientations. A few other frequency dependent features can also be observed. The fine details of these features differ for the two grating orientations. Whilst one can write pages on the phenomena of diffractive gratings and plasmonics [104], our primary concern is how they affect our imaging technique. Therefore, due to their weakness we can ignore these diffractive effects.

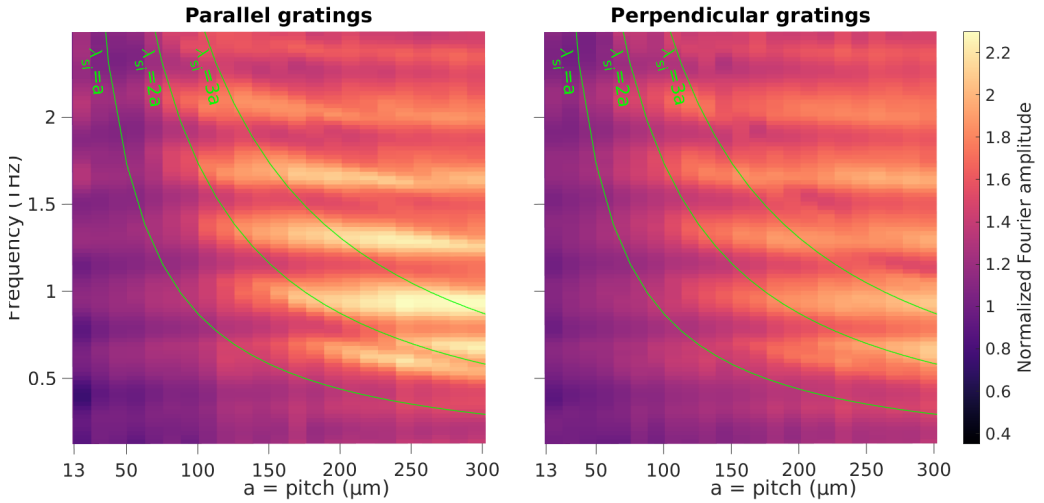

Figure 5.10: Fourier spectra of the THz transmission through gratings (50% fill fraction) photoexcited on a 115μm thick silicon wafer. The left (right) plot is when the gratings are aligned parallel (perpendicular) to the incoming THz radiation. Frequency and pitch on the vertical and horizontal axis respectively. Note, the spectra have been normalized to when the silicon was homogeneously photoexcited. The three green lines show when the silicon wavelength equals 1,2 and 3 times the grating pitch.

In the frequency spectrum we see that the major difference between the two grating orientations arises in the Fabry-Perot minima. Our imaging technique measures the peak field-strength of our THz pulse (i.e. at $3.5ps$ in fig. 5.9) and not the consequent Fabry-Perot pulses. Therefore, these differences in the Fabry-Perot minima are of little concern to us. However, the THz peak value does increase with pitch. This is of great concern as it implies that Hadamard masks with low spatial frequencies are more transmissive than those with high spatial frequencies. Next we outline a way of

overcoming this phenomena.

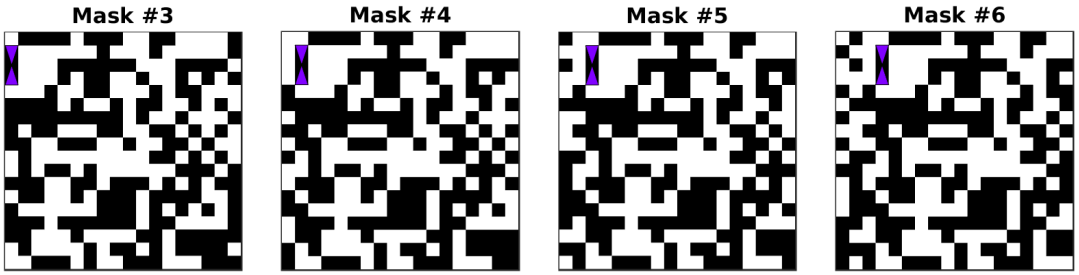

Figure 5.11: Four consecutive imaging masks constructed from a Paley type II Hadamard matrix. The blue triangles are there only as a guide to indicate how the pixels shift with each consecutive mask.

Since the transmission of the diffraction gratings depends on the spatial frequency of the grating, we are interested in having the same spatial frequencies for all our imaging masks. As can be seen in the example masks of fig. 5.2, this can not be accomplished with Sylvester Hadamard matrices. However, Paley type-II Hadamard matrices are constructed differently which results in the creation of cyclic imaging masks. Such masks are named so since the i^{th} mask is obtained by shifting all the apertures from the $(i-1)$ mask to the right[1]. This means that the spatial frequencies of all the masks are similar. This will reduce the effects observed when photoexciting subwavelength structures.

To demonstrate this we measure the transmission through different sub-wavelength masks constructed via the Sylvester and Paley type-II construction techniques[2]. The projected masks are set to have pixel sizes of $20\mu m$, hence some masks will have similar spatial frequency content to a grating with $40\mu m$ pitch. Our results are shown in fig. 5.12. Note, the signals here have been normalized to the transmission through homogeneous photo-excitation. It can be seen that some Sylvester masks have a factor of two more transmission than other masks. The Paley type-II masks however do not have such large discrepancies. This demonstrates that when sub-wavelength

[1] This arises from the cyclic permutation used in constructing a Paley type-II Hadamard matrix. See §3.4.2.2 for construction details. Further, this rule does not apply to the first mask since it has all of its apertures open.

[2] Note, only the transmission through a positive set of masks was measured. Further more, we measure the peak-field strength of our THz pulse (see fig. 3.2) since that was done for most imaging experiments in this thesis.

dimensions are utilized Paley type-II masks are preferable than Sylvester ones for the reasons in the previous paragraph.

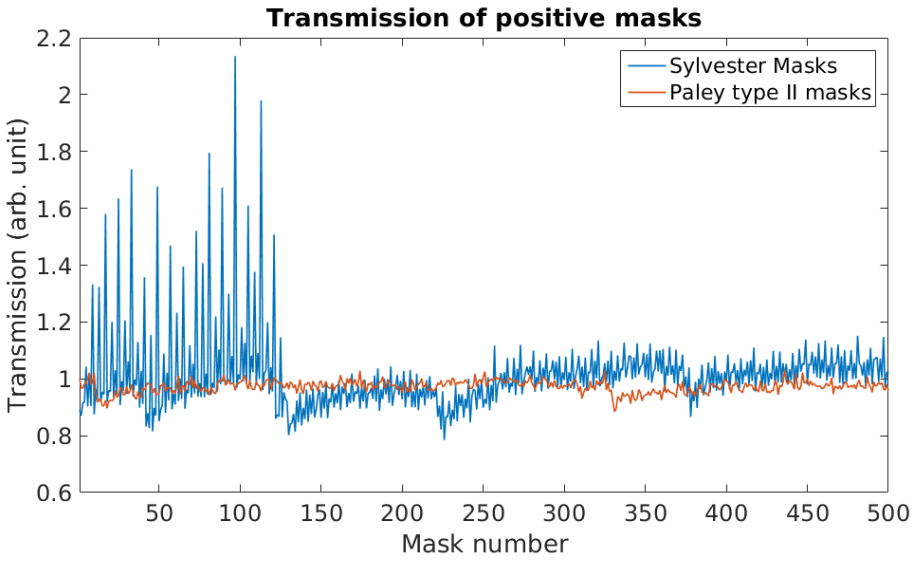

Figure 5.12: The THz field transmission through through the first 500 masks, from an $H_{64\times64}$ matrix, constructed via the Sylvester (Paley type-II) technique in blue (red). The masks were photoexcited on a 115μm thick silicon wafer (1000$\Omega \cdot cm$ resist). The individual aperture size in each mask was 20μm, meaning an image with 20μm spatial resolution would be commuted from the full set of measurements.

Conclusions

This chapter starts by showing a typical set of Hadamard measurements made in order to obtain an image. Next we consider the resolution limit in our imaging approach. We explicitly show that the image resolution is determined by the thickness of the photo-modulator used. By the using an ultra-thin (6μm) silicon wafer we demonstrate THz imaging with 9μm ($\lambda/45$ at 0.75THz) spatial resolution. At sub-wavelength resolutions polarization effects become important, hence the final section concerns it self with polarization. In particular, we demonstrate a possible application: we use polarization resolved imaging to detect sub-wavelength breaks in electronic circuits hidden behind optically opaque silicon. The chapter concludes by concerning itself with how do polarization effects, in the masks, affect our imaging technique. It is shown that when structural dimensions around the wavelength are present one can expect negative effects. We discuss a way of minimizing such effects.

Chapter 6

Noise and under-sampled images

This chapter is an investigation of how noise affects the image quality when fully sampling and under-sampling the image. Further, when under-sampling we investigate how different reconstruction algorithms perform.

6.1 Noise in the THz-TDS photomodulator imaging system

Detector noise is commonly defined as the values that the detector shows with no light incident upon it. Source noise arises from the amplitude fluctuations of the device emitting light. The noise in this type of imaging system is probably unlike any other imaging system. The reason for this is that the THz source, THz modulator and THz detector are all powered from the same Ti:Sapphire laser system, as shown in fig. 3.1a. Therefore, noise in the Ti:Sapphire laser will transfer itself onto the source, modulator and detector components. Further, since this technique relies on the temporal synchronization between the THz, optical pump and optical detection pulses, all this noise is correlated. However, since the generation and detection techniques used here rely on non-linear optical phenomena (see ch. 3), the correlation is difficult to model. Regarding the silicon photomodulator, the powers used to photoexcite the Si wafer are well into the saturation regime, hence a 5% drop in pump power will not result in a 5% drop in modulation efficiency. Therefore noise from the modulator is expected to be the smallest contributor to the degradation of image quality.

In Fig. 6.1 we show the two main sources of noise in our system. Our detector

noise is around 4 orders of magnitude smaller than the peak of our THz pulse[1]. In general this type of noise hinders raster scanning techniques. The source noise, amplitude fluctuations in our THz peak, can be seen to have two main components to it. First, low frequency oscillations with a period of around 20 minutes. These were found to be due to changes in the humidity levels[2] caused by the lab air-conditioning systems, hence could be switched off or controlled. Second, there is a high frequency noise with RMS of around 5% from the mean. This noise is inherited from the regenerative amplified Ti:Sapphire laser system. Finally, this noise is also affected by the alignment on the balanced diodes used for THz detection (see §3.1.2.2 for detection details).

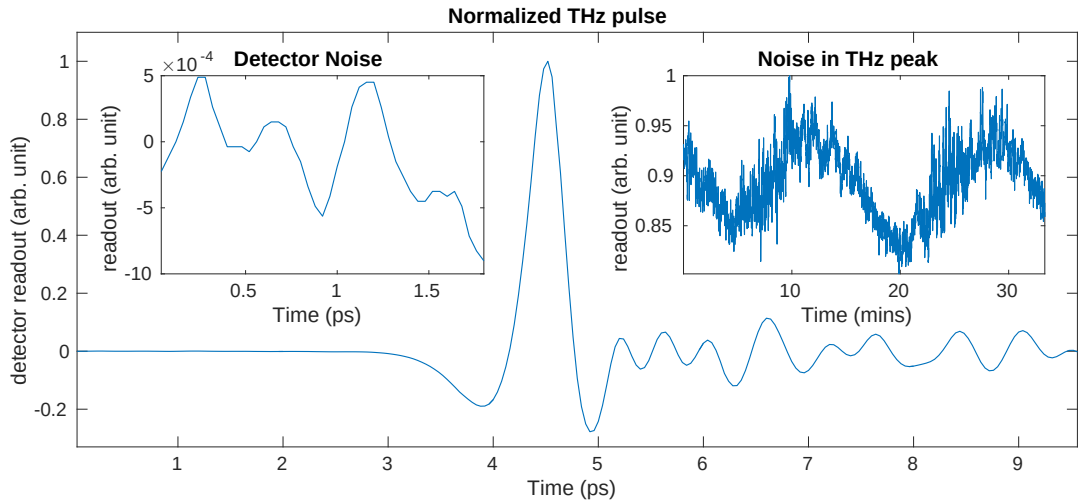

Figure 6.1: Normalized THz pulse. Left inset: The first 1.75ps of the THz pulse zoomed in. Right inset: The value of the THz peak over a period of 35 minutes.

6.2 Results

6.2.1 Minimizing low-frequency source noise

If one is not able to eradicate low-frequency amplitude oscillations in their light source, one can minimize this unwanted source of noise. This is achieved by the using spatial encoding masks constituted by +1s and -1s as opposed to 1s and 0s, see §3.4.1 for the details of experimental implementation. In fig. 6.2, we compare the difference

[1] We measure the peak of our THz pulse as the detector readout for each mask (see §3.1.2).
[2] Water vapor strongly absorbs THz radiation.

between using encoding masks derived from Hadamard matrices with [1, -1] and [1, 0] values. Here we can see that the image constructed from [1, 0] measurement has some artifacts created from low frequency THz source oscillations (indicated by the arrows), whereas the [1, -1] measurement have eliminated most of this type of artifact.

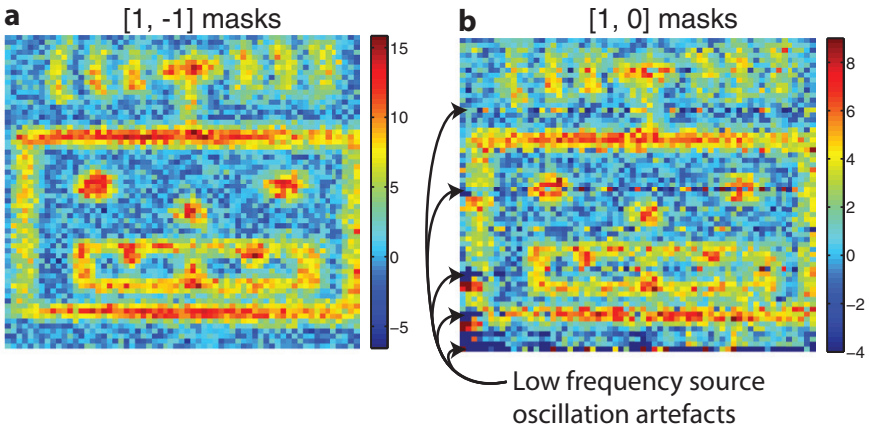

Figure 6.2: ***[1, -1] vs [1, 0] masks.*** 64×64 *Images obtained using Hadamard masks with values of [1, -1] in* ***a*** *and [1, 0] in* ***b****. Total number of measurements is 16384 for both pictures.*

The reason masks with elements of [1, -1] are less affected by slow amplitude source oscillations than those with elements of [1, 0] is now explained. Consider imaging a perfectly homogeneous beam. If we have two different [1, 0] masks where half the elements are 1s and the other half 0s, they would have the same detector readout of half the total beam intensity in a world with no noise. However, if they are taken at different phase points in the source noise oscillation cycle, then our detector will display different values. Now consider the same perfectly homogeneous beam, however we now have two different [1, -1] masks where half the elements are 1s and the other half -1s. The detector readout will be zero for both of them in a world with no noise. Now if measure our masks at different phase points in the source noise oscillation cycle, then the detector readout will still be zero for both masks since we are measuring half the beam intensity minus the other half. Therefore since these masks have the same readout they are not affected our low-frequency source noise. Although, in our experimental implementation (see 3.4.1), it needs to be pointed out that this argument only holds true should the positive and negative masks are measured on a time scale much quicker than the period of the source oscillations.

6.2.2 Raster, Random and Hadamard masking schemes

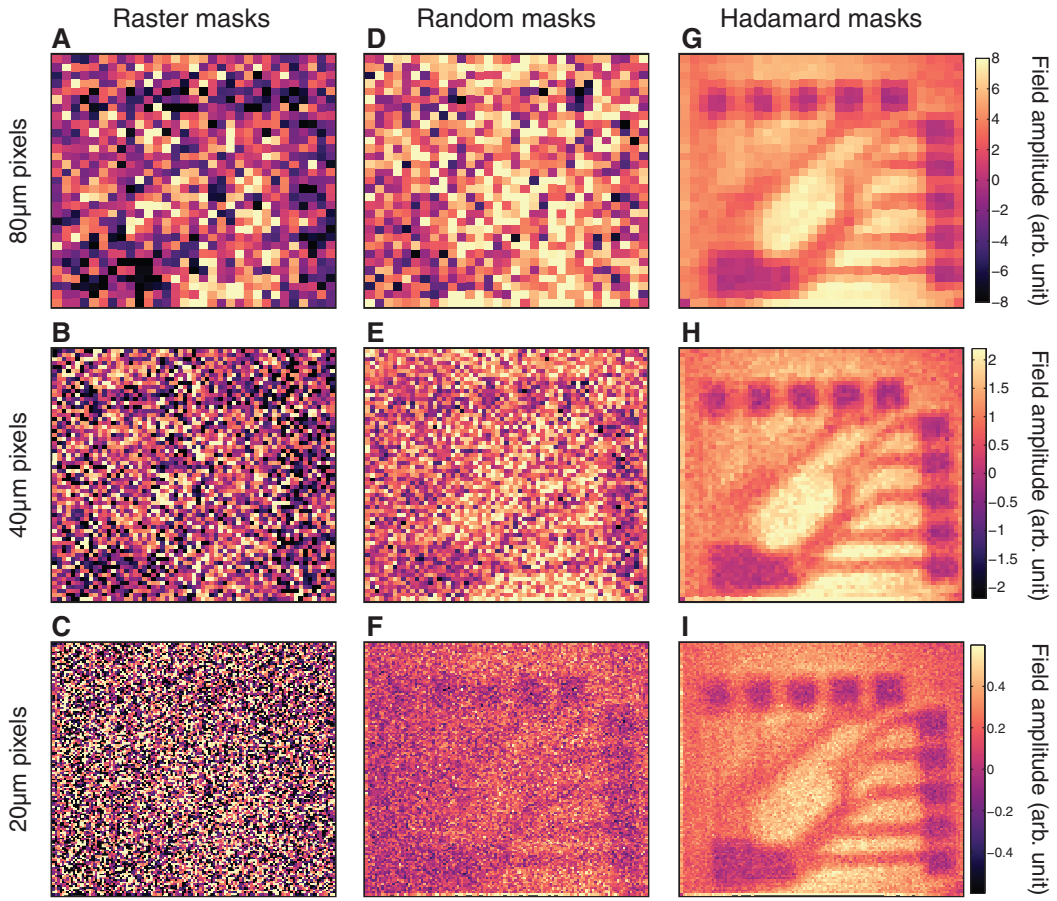

Figure 6.3: Increasing image size. ***A*****-****C***, *Images obtained using raster masks with increasing number of pixels from* 32×32 *to* 64×64 *and* 128×128, *respectively.* ***D*****-****F** **(G-I)**, *Images obtained using random (Hadamard) masks as number the of pixels is increased from* 32×32 *to* 64×64 *and* 128×128, *respectively. The vertical lines seen in part* ***C*** *are associated with periodic changes in lab environment. Note* ***A***, ***B***, *&* ***C*** *have been scaled by 0.9, 0.25 & 0.1, respectively, so as to be plotted on the same scale as all other images.*

Here we investigate how experimental noise affects the three different masking schemes, outlined in §3.4.2, as the number of pixels in the image is increased. For this, we take images under identical conditions (one after the other) of the circuit board in Fig 5.8**a** with increasing number of pixels. Our results are shown in Fig. 6.3. Hadamard masks have the most superior signal to noise followed by random masks and then by raster scanning. This is true for all image sizes. Raster scanning is most

affected by detector noise due to the small signals emanating from a single aperture. On decreasing the aperture size, and increasing the number of pixels, image noise clearly increases. This effect is less significant for the multi-pixel approaches as these have larger associated signals. While multi-pixel patterns clearly have the benefit of increased signal to noise, the continual increase in the number of pixels leads to increased image noise, even for Hadamard imaging. This is because the signal from each individual pixel decreases as the number of pixels increase, and even though Hadamard matrices minimize the mean square error in each image pixel [95] they do not completely remove all noise. One should also note that we have noise in our THz source which further degrades image quality as the number of measurements required to form the image increases. Interestingly, random masks seem to fare best as the number of pixels increases. It can easily be shown that is an artefact caused by the simple for-loop reconstruction algorithm employed. The performance of random masks can be improved by using more complex image recovery algorithms.

In figs. 6.4**A** and **B** we compare the level of noise in images, obtained with a random sampling matrix, as recovered by a simple for-loop and a total variation minimization algorithms (eq. 3.23) respectively. It can be clearly seen that the total variation algorithm has superior performance. Further, in fig. 6.4**C** we plot the image obtained with Hadamard masks. We see that orthogonal masks are still superior. This is partly due to the fact that Hadamard matrices minimize the mean square error in each image pixel [95] and partly due to the value of our relaxation parameter. In other words, we could further improve the quality of our random mask image with more careful considerations of our value for γ in eq. 3.23. However, the Hadamard reconstruction uses a simple for-loop algorithm, the same as fig. 6.4**A**, where as the total variation algorithm is more complicated (taking us $\sim 100s$ as opposed to $\sim 10ms$).

6.2.3 Under-sampling with a random matrix

In this section we investigate how different compressed sensing algorithms perform in our experimental system when we under-sample our object. Our results are shown in fig. 6.5, where we take 72×72 images of $\nabla \cdot \mathbf{E} = 0$ and $\nabla \cdot \mathbf{B} = 0$[1] as we decrease the number of measurements with the top, middle and bottom rows respectively

[1]Using photo-lithographically, we manufactured "$\nabla \cdot \mathbf{E} = 0$" and "$\nabla \cdot \mathbf{B} = 0$" out of gold onto the exit interface of our silicon wafer.

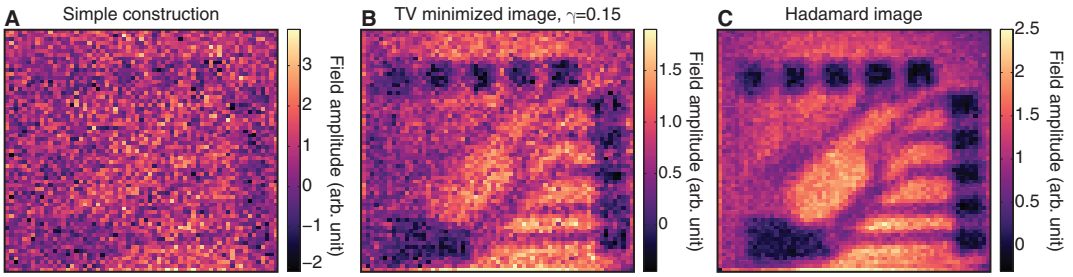

Figure 6.4: 64×64 *images of a circuit board where* ***A*** *and* ***B*** *have been obtained using random masks except* ***A*** *was constructed using our simple algorithm and* ***B*** *has be constructed via a total variation minimization algorithm from the same data.* ***C;*** *image of the same circuit board obtained via Hadamard masks.*

using 75%, 50%, 35% the number of measurements as the number of pixels. The first column uses the simple for-loop image reconstruction and the next three columns respectively use the problems of eqs. 3.21, 3.22 and 3.23. For all algorithms, the image is visible when the number of measurements is 75%. In this top row, the best images are parts **D** and **G** followed by **J** and finally **A**. However, we decrease the number of measurements to 50% then parts **E, H** and **K** become similar in image clarity with **B** performing the worst. In bottom row, the best image is part **L** with **F** and **I** being equal with **C** performing the worst again. The performance of the for-loop reconstruction is expected to be the worst given that it also incurs a false reconstruction in noise free simulations[1]. The similar performance of the second and third columns is expected since they both minimize the $L1$-norm. Although, the third column has an extra parameter, γ, to improve the image quality, this parameter was found mostly to affect the amplitude all of the points. This is because the $L1$-norm is the sum of all absolute values of a vector. Therefore this can be minimized by just dividing all the values by a constant value. We believe this is what algorithm did as γ was varied. Hence an improved way of solving the problem of eq. 3.22 should mitigate this, or perhaps a minimization of the $L0$-norm with a relaxation parameter would mitigate this. Regarding the fourth column, this algorithm uses the for-loop image as an initial guess, hence its superiority over the for-loop method. Further, many image denoising methods perform a total variation minimization [98, 103]. Comparing the $L1$-norm algorithms to the total variational one, the inferior performance of the TV-

[1]The matrix doesn't satisfy $AA^T = NI_N$, hence this is not a solution satisfying the original problem

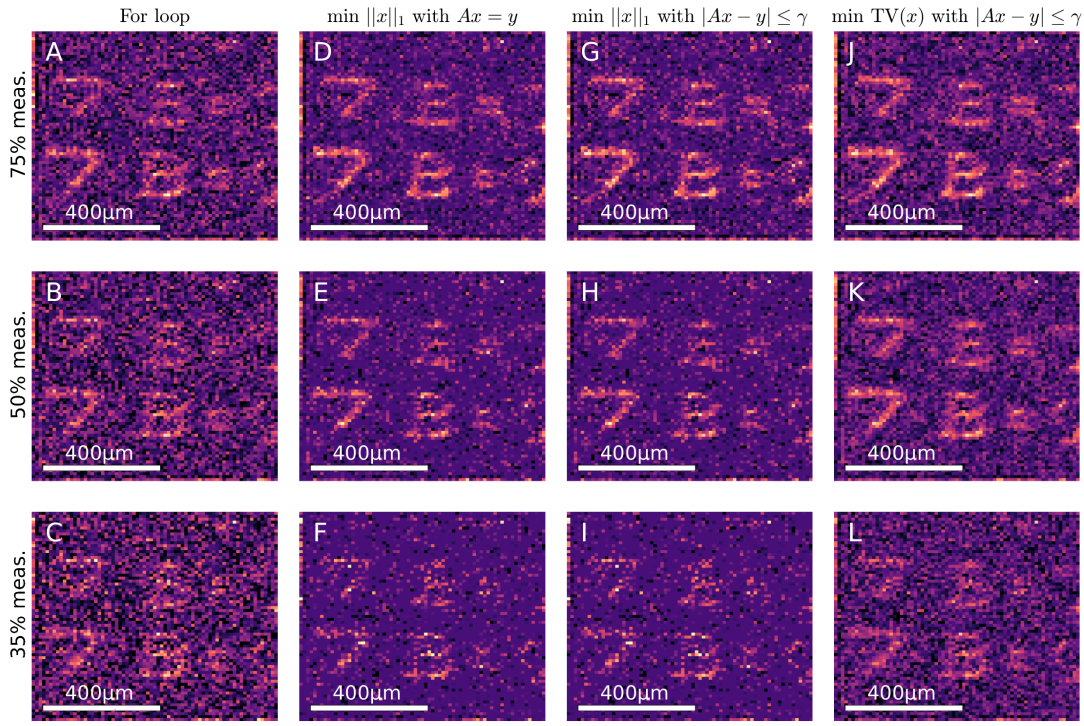

Figure 6.5: 72×72 Images of $\nabla \cdot \mathbf{E} = 0$ and $\nabla \cdot \mathbf{B} = 0$ reconstructed via different Compressed sensing algorithms. The top, middle and bottom rows respectively have 75%, 50% and 35% number of measurements as the total number of pixels. The first, second, third and fourth columns respectively use a for-loop, eq. 3.21, eq. 3.22 and eq. 3.23 image reconstruction algorithms. Note each image has been plotted on a colourscale that best shows the image.

min at 75% number of measurements and its superior performance at 35% number of measurements is explained as follows. Increasing γ in the TV algorithm has the effect of reducing noise by smoothing out the image, however it also reduces the sharpness of edges as well. Therefore, an optimal value of γ will strike a balance between noise removal and image preservation. In parts **D** and **G**, the large number of measurements are sufficient in number to allow the $L1$-norm algorithms to determine the object with reasonable accuracy, where as our optimal value of γ prevents further noise removal in part **J**. As we decrease the number of measurements, all algorithms have more difficulty in obtaining the relevant solution. However, the total variational algorithm fairs best due to lack of image features yielding greater freedom in regards to the value of γ.

6.2.4 Adaptive imaging

In this section, we investigate two strategies to reconstruct images using undersampled sets of measurements: *adaptive sampling* and *compressed sensing*.

Using adaptive sampling, we first measure a low resolution image and then sample regions of interest with progressively higher resolution. The regions to sample are determined using a single-tier 2D Haar wavelet decomposition. The Haar wavelet transform is a hierarchical structure that highlights the presence of edges in an image at a series of progressively finer scales [105].

This can be used to compressively sample an object by making use of the assumption that high values of wavelet coefficients at coarse scales are highly correlated with high values at finer scales [100]. This is a reasonable assumption which can be understood by considering that sharp edges are represented by non-zero Fourier components across a wide spectral range. Therefore, identification of coarse edges from an initial low resolution image then determines where to sample at a higher resolution. After each resampling phase, the process is repeated until the required resolution is reached. A more detailed description of the algorithm used is given in §3.4.3. Using adaptive sampling the solution is straight-forward to recover, however the reconstruction possesses an uneven distribution of pixel sizes.

Figure 6.6 compares reconstructed images of a transmissive object depicting two of Maxwell's equations as the number of measurements for both adaptive compression and compressive sensing are reduced. On the top row, we see a homogeneous spatial distribution of noise. This renders the image less obvious. On the bottom row, we can see that there are different sized pixels, hence an uneven distribution of the noise. The main features of the image are clearly seen for all measurement amounts. Further, we see an increase in the noise level as the number of measurements is increased.

Comparing the two, we observe that the adaptive sampling approach out performs the compressive sampling approach in this specific case. Although we note that our image recovery algorithms are not designed to take into account the level of noise in our measurements. Further, here we have kept our assumptions about the object under investigation quite general: simply that wavelet tree truncation is reasonable, and that the objects are sparse when expanded in the Fourier basis. We aim to demonstrate the feasibility of these techniques rather than optimize the sampling and reconstruction algorithms to suit the object under tests and measurement conditions. We anticipate improved results should one develop an algorithm taking into account

specific prior knowledge of the object combined with knowledge of the measurement noise.

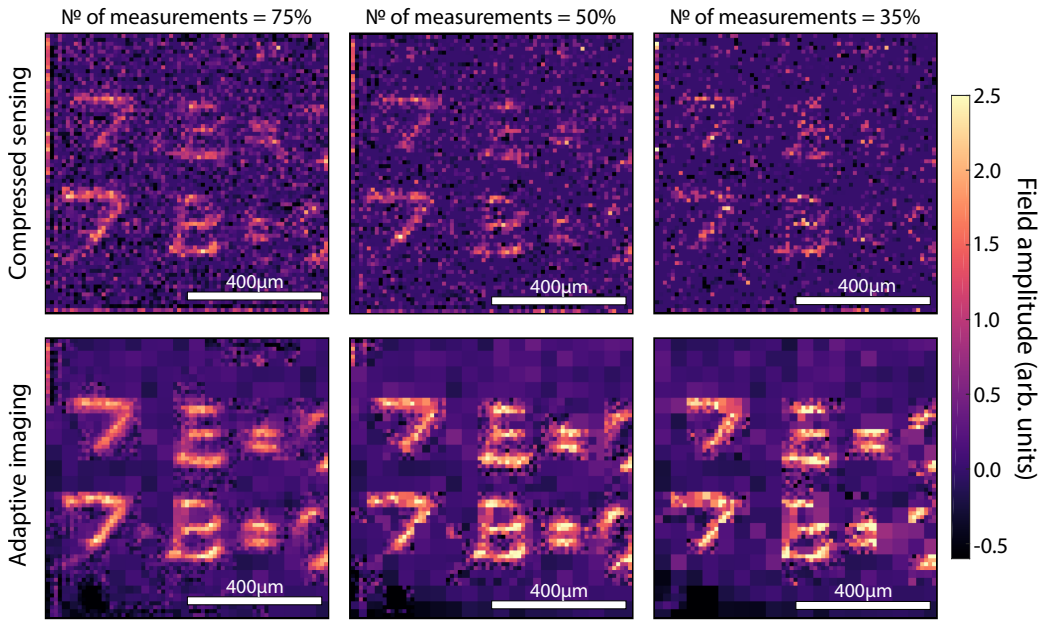

Figure 6.6: Compressive 72×72 THz images of $\nabla \cdot \mathbf{E} = 0$ and $\nabla \cdot \mathbf{B} = 0$ with decreasing number of measurements, where the top, middle and bottom columns respectively use 75%, 50% and 35% measurements as the number of pixels. Top row: compressed sensing. Bottom row: adaptive sampling.

Conclusions

Here we have shown the type of noise that is present in our THz-TDS system. Namely, there exists detector noise 4 order of magnitude smaller than our THz peak, source noise with low frequency (period is about 20 minutes) amplitude oscillations and a high frequency source noise with an root-mean-squared value deviating from the mean of about 5%. Then we show how to minimize the low frequency source noise using masks with elements of 1s and -1s. Then we show how different masking schemes perform is our system, with orthogonal masks performing best. We demonstrate how undersampling with a random matrix and adaptive imaging perform in our experimental system. We find adaptive imaging to outperform sampling with a random matrix. It should be noted that undersampling at sub-wavelength resolution is has not yet been demonstrated in any other spectral regime.

Chapter 7

Subwavelength THz imaging of Graphene Photoconductivity

Summary

Using a spatially structured, optical pump pulse with a THz probe pulse, we are able to determine spatial variations of the THz photoconductivity in a planar graphene sample with sub-wavelength resolution ($75\mu m \approx \lambda/5$ at $0.75THz$). We compare our results to Raman spectroscopy and correlate the existence of the spatial inhomogeneities between the two measurements. We find a strong correlation with doping inhomogeneity. This demonstrates the importance of eliminating inhomogeneities in electron density during CVD growth and fabrication for photoconductive devices.

7.1 Graphene

The unique opto-electronic properties of graphene have received a lot of attention [106]. For example, ultrafast carrier relaxation[107–111], highly tunable doping levels[112], theoretical mobilities in excess of 150,000 $cm^2V^{-1}s^{-1}$ [112], and high thermal conductivity [113] all lend themselves to a number of interesting device applications. However, the large scale manufacturing of this 2D material, usually through chemical vapour deposition (CVD), is not yet perfected and it is well established that there are a number of sources of quality degrading, spatial inhomogeneities such as charge puddles, grain boundaries, substrate induced strain variations, surface impurities, multilayer nucleation sites and fabrication residues [114–117]. Raman

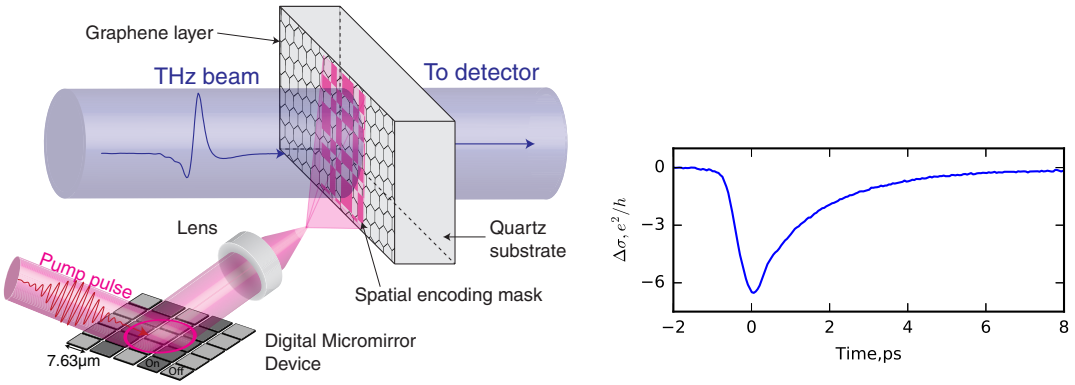

Figure 7.1: ***Right:*** *The imaging setup; a patterned 800nm pump beam is used to photoexcite a graphene sample on quartz substrate (from graphene supermarket). The graphene is then probed with a THz pulse* $(\lambda_0 = 400\mu m, FWHM = 750\mu m)$. ***Left:*** *Spatially averaged photoconductivity as a function of time delay after photoexcitation. Arrow shows the point at which the photoconductivity maps are measured.*

spectroscopy and imaging has emerged as an important characterisation tool here, due to its sensitivity to layer number [118], strain[117], carrier concentration[119] and defects[120–123]. However, the conductivity, a critical quantity for many opto-electronic applications, including photodetectors [124, 125], cannot be explicitly determined directly in Raman, due to the limited number of observable quantities.

Given the relevance of the conductivity to many opto-electronic applications of graphene, optical-pump THz-probe spectroscopy has attracted considerable interest in the literature in recent years [126–130]. This experiment can determine the ultrafast photoconductivity of graphene, an important quantity which is now understood to have a complex dependence on mobility, electron concentration and relaxation rate[129–131]. However, due to the large THz spot sizes ($\approx mm$) used in these experiments, they typically provide spatially averaged information, and are therefore ignorant of the small spatial inhomogeneities typical in CVD graphene.

In this study, we devise a technique able to directly image how these spatial inhomogeneities affect the local photoconductive THz response of graphene. This is achieved via spatial patterning of the optical pump beam, allowing us to selectively sample our graphene, and thereby building a THz photoconductivity map of our CVD sample. We compare the spatially dependent THz photoconductivity to Raman spectral maps and find there to be various correlated features. We find that small regions of graphene with low electron density display a strongly suppressed photoconductivity on ultrafast timescales. Since the resolution of our measurement is determined by the

patterned optical pump pulse, we are able to observe these small regions of suppressed THz photoconductivity on markedly sub-wavelength length scales ($75\ \mu m \approx \lambda/5$ at 0.75 THz).

DMD Phase front correction Note that for this experiment to work one needs to eradicate the phase front distortion induced by the DMD as shown in §3.4.1.1.

7.1.1 THz measurements of graphene

We use the setup outline in §3.1.2 to generate and measure our THz field. We measure the electric field, E, of a single cycle THz pulse (0.1-2THz see §3.1) transmitted through our sample. Note that, in all the data presented in this chapter, we discuss only changes in the peak of the transmitted THz pulse, as in ref. [130]. This gives a spectrally averaged measurement weighted to the spectral peak of our THz pulse (0.75THz). The femtosecond laser system also provides a third pump beam used to photoexcite the graphene. Our raw measurement of the temporal photoexcitation dynamics of graphene are shown on the left of figure 7.1 where we plot ΔE, defined as

$$\Delta E = E_{\text{Pump On}} - E_{\text{Pump Off}}, \tag{7.1}$$

as we vary the arrival time of the optical pump beam. Here, the photoexcitation pulse can be seen to arrive at $\sim 0ps$. We see a fast, sub-picosecond carrier rise time followed picosecond relaxation times (associated with cooling to acoustic phonons) as observed previously in refs. [126, 127, 129, 130]. From this measurement one can extract the photoconductivity, $\Delta\sigma$, via the relation [109]

$$\Delta\sigma = -\frac{1+n_{\text{sub}}}{Z_0}\frac{\Delta E}{E_{\text{Pump Off}}}, \tag{7.2}$$

where $E_{\text{Pump Off}}$ is the transmitted THz field before photoexcitation, Z_0 the impedance of free space and $n_{\text{sub}} \approx 1.9$ is the refractive index of the quartz substrate. From the data on left in fig. 7.1, it is clear that we have a negative photoconductivity (i.e. a conductivity which decreases on photoexcitation). This is typical for graphene with an intrinsic Fermi level greater than 120meV [132] (from Raman measurements [117], we estimate the intrinsic Fermi level of our sample to be 800meV). However, it is important to note that this is a spatially averaged result: due to the restrictive diffraction limit for THz radiation, THz photoconductivity can typically only be

determined with mm spatial resolution.

To overcome this resolution limit, we introduce spatial modulation in the optical pump beam, as illustrated on the right of figure 7.1. In short, we employ Hadamard matrices, see §3.4.2.2, as our sampling matrix. We spatially measure the photomodulation induced in the graphene, as opposed to ch. 5 where we use photomodulation (in silicon) to image another object. In this experimental design, the theoretical imaging resolution is limited by the Rayleigh criterion for our pump beam. However, in practice the image resolution is dictated by the signal to noise ratio in experiment [133]. We find that a resolution of 75 μm is sufficient to resolve most of the conductivity features in our sample. Note, the DMD induces a phase front in the optical excitation beam, which needs to be removed as shown in §3.4.1.1.

7.1.2 Comparison to other THz imaging techniques

It must be noted that this is not the only near-field THz imaging technique usable for looking into graphene. The other main techniques use near-field apertures or probe-tips [134–137]. These techniques differ from ours in that they directly measure the near-field THz radiation, as opposed to how photoexcitation affects the THz transmission. Using a near-field aperture allows one to perform THz spectroscopy on sub-wavelength graphene structures [134]. From this one can directly observe how sub-wavelength antennas and gratings perform. The near-field probe scatters [135–137] do something else. Graphene supports surface plasmons in the mid-infrared to THz frequency regime [138, 139], therefore the tip-scatterer launches THz plasmons that propagate along the graphene surface. Here one can directly detect the surface plasmon and measure both its propagation length and wavelength. It should be noted that THz plasmons on graphene are confined to spaces 50 times less than free-space THz wavelength [139]. This allows for the creation of highly sub-wavelength plasmonic sensors, which would be best inspected by tip-scattering techniques.

As a comparison, all these near-field THz imaging techniques (including ours) detect growth inhomogeneities. However, using our technique to measure the response of a plasmonic structure is rendered difficult as one has to also launch the THz plasmon. Further, we are not directly measuring the surface charge oscillation and therefore we would have to make assumptions about how it affects our measurement. However, the other two techniques require would require major modifications to measure the photo-conductive response, a quantity needed for photo-detectors.

They are also inherently limited to raster scanning.

7.2 Results

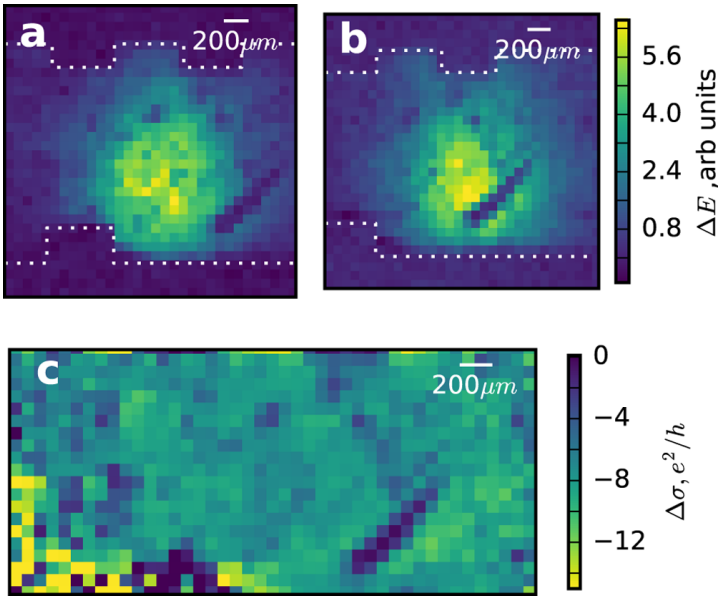

Figure 7.2: ***A*** *ΔE measured at $x = 0\mu m$ showing the graphene response convoluted with the THz probe spot (white dotted lines shows gold alignment markers)* ***B:*** *ΔE measured with a shift of 450 μm with respect to* ***A****.* ***C:*** *ΔE normalised to the spatial average of ΔE showing the graphene response without the THz beam profile.*

The imaging results are shown in figure 7.2. We measure at the time overlap between the pump and THz beams. Figures 7.2**A** and **B** are images showing the spatial dependence of ΔE as recorded with our single-element imaging scheme. The THz probe beam profile can be observed in the centre of both images, with a number of additional features inside the spot. In order to separate the spatial response of the sample from any spatial inhomogeneities of the THz and optical pump beams, an averaging technique is employed, where the sample is laterally scanned with respect to the pump and probe beams. This allows us to extract any intensity variations associated with the graphene sample itself. In figures 7.2**A** and **B** the sample has been laterally offset by $x = 450\mu m$. As the sample translates left to right, we use gold markers (square features at top and bottom) to track its movement. The full set of results are shown in supplementary materials as video S1. The average beam

profile is then extracted by the taking mean of all N images in the stack;

$$\Delta E_{\text{beam}}(x,y) = \frac{1}{N}\sum_{i=0}^{N} \Delta E_i(x,y). \tag{7.3}$$

where ΔE_i is the i^{th} image in the stack of images. The response of the graphene itself is then obtained by averaging the resultant stack of images, accounting for the mechanical shift of the sample (x_i) using

$$\frac{\Delta E}{E_{\text{Pump Off}}} = \frac{1}{MN}\sum_{i=1}^{N} \frac{\Delta E_i(x-x_i,y)}{\Delta E_{\text{beam}}(x,y)}, \tag{7.4}$$

where M is a normalization factor which equates the spatially average photoconductivity to the photoconductivity measured in fig. 7.1. The photoconductivity is then obtained via eq. 7.2.

In figure 7.2**C** we plot the normalised THz photoconductivity of our sample. We see a predominance of a negative photoconductivity across the sample, as expected for graphene with a Fermi level $\gg 120meV$ [131]. However, we also see a number of regions in the image where the photoconductivity is more than a factor five lower than the spatial average. Below, we try to understand the origin of these features using Raman microscopy.

Raman spectroscopy measures inelastic scattering from optical phonon modes in the graphene. A typical spectrum is shown in figure 7.3, with three peaks corresponding to phonon modes: the zone center mode G and the first and second harmonics of the D zone edge phonon. We obtain a spectral Raman map of the area of our sample. Then we fit each of the three spectral peaks single Lorentzians in order to extract central frequencies, intensities and widths at each individual graphene pixel. Note that, due to the mismatch in resolution between Raman and THz imaging approaches, multiple Raman spectra were recorded within each 75μm area in order to give an indication of the average response of each pixel and minimize disparity between the measurements. It is important to note that the

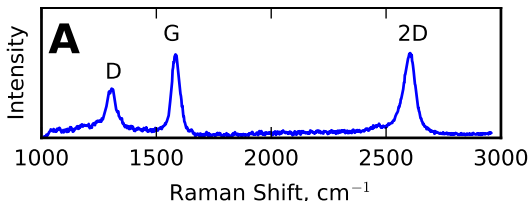

Figure 7.3: Typical Raman spectra showing the three main graphene peaks.

D peak does not conserve momentum and is therefore a defect activated peak. As discussed later, we observe a distribution of defects in our Raman images, as expected for CVD graphene [120–123]. Finally, by looking at the exact frequencies and the widths of the G and 2D peaks one can calculate the graphene carrier concentration, however the details of this procedure have been omitted from this thesis and the reader is pointed to the actual publication of ref. [140]. Here we only present the final result.

In figure 7.4 we compare the spatial dependence of the THz photoconductivity, **A**, against spatial maps of the Raman defect peak intensity, **B**, and electron concentration, **C**. In order to make fair comparison between the Raman and the THz images we have averaged the Raman signals using a spatial filter. In all four images we observe a feature to the bottom right of the imaged region, indicating a small tear in the graphene. However, the correlations to some of the more subtle features in Fig. 7.4A are less obvious - we discuss here in more detail.

Firstly, figure 7.4**B** is obtained by plotting the defect peak intensity, normalized by the intensity of the G peak - this results in a spatial map of localized defects in the graphene. From this image, it is clear that these local defects are arranged along distinct lines, possibly resulting from folding during during growth, or possibly resulting during transfer. Irrespective, there is little or no correlation to the THz photoconductivity observed in fig. 7.4**A**. This is symptomatic of the *local* conductivity, sensitive to motion on the ultrafast timescales, typically observed in THz measurements [141], which is unaffected by these boundaries.

In figure 7.4**C** we plot the spatial dependence of the carrier concentration. This shows a much more clear cut correspondence to the THz photoconductivity plotted in figure 7.4**A**. We see very low THz photoconductivity, around a factor of five lower than the spatial average, in regions of low doping compared to the high doping regions. The clear correlation between Raman and ultrafast photoconductivity constitutes one of the major findings of our work, and suggests that the steady state electron density plays a crucial role in determining the photoconductivity [127, 129, 130, 132], a quantity of crucial importance for any photo-detection applications.

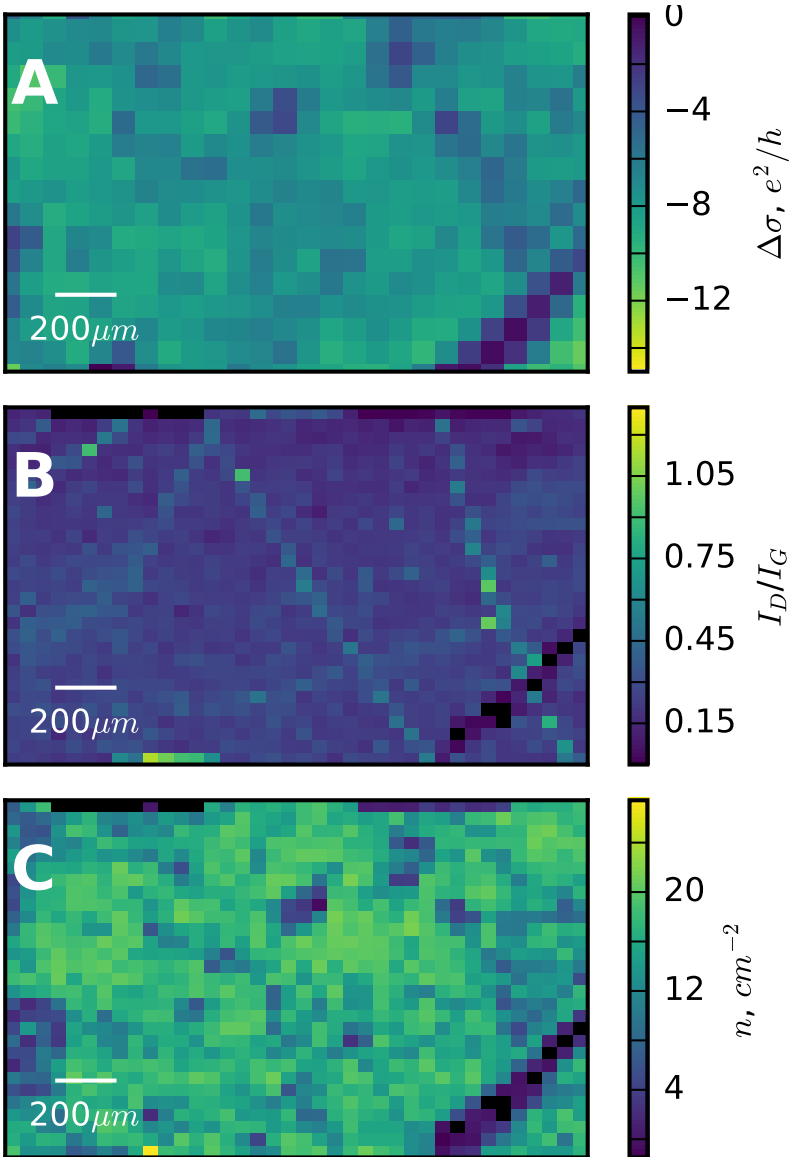

Figure 7.4: ***A:*** *Graphene photoconductivity map showing the region of interest also covered by the Raman map* ***B:*** *Normalised intensity map of defect peak showing the relative spacial intensity of the D peak. Averaged to the same pixel size as* ***A****.* ***C*** *Spatial map of carrier concentration, Averaged to same pixel size as* ***A****.*

Optical Image of the Sample

Figure 7.5: Optical image of the graphene sample.

In Fig. 7.5 we show a white light reflection image of our graphene sample area taken with a x20 objective on the Renishaw inVia system (the Raman spectrometer). This shows the graphene rip in the lower right corner, also observed in our Raman and THz images. Note that the field of view in the reflection measurements is rather small, and the repeating pattern seen is an artifact caused by stitching of separate images. This effect has been minimized by overlapping individual images and applying a background subtraction tool (WIRE software).

The sample was bought from graphene supermarket deposited on a quartz substrate via chemical vapor deposition. Nothing else was done to the graphene. The gold markers were created via photo-lithographic techniques.

Conclusions

To conclude, we present a new experimental method for imaging the THz photoconductivity of graphene on small length scales. By selectively photoexciting regions of the graphene and then measuring the photoconductive terahertz response, we can observe variations with sub-wavelength resolution (currently 75 μm $\approx \lambda/5$ at 0.8 THz, though a fundamental limit approaching 1μm, set by the optical diffraction limit, should in principle be possible). By comparing our images to Raman maps, we find a strong correlation with strain and electron concentration. We attribute the causation of this correlation to doping inhomogeneity. This demonstrates the importance of eliminating these strain and doping inhomogeneities during CVD growth and fabrication for photoconductive devices.

Chapter 8

Subwavelength hyperspectral THz imaging of articular cartilage

This chapter demonstrates hyperspectral polarization-resolved THz imaging on biomater. We show that the THz permittivity of a sample, articular cartilage, can be extracted with 65μm $(\lambda/6)$ spatial resolution. We observe that the permittivity varies on a sub-wavelength scale and find it correlated with the structure of our sample.

The main motivation behind this chapter is that near-field THz imaging techniques compatible with biological matter are nearly non-existent. As with all the previous chapters, we employ a time-varying optical pattern projected onto a 6μm-thin silicon wafer to achieve near-field modulation of a co-incident THz pulse. We image using a Hadamard encoding scheme as outlined in §3.4.2.2. Further, by measuring the temporal evolution of the THz field in the imaged field of view the THz permittivity of a sample can be extracted, via the methods in §3.2.1, with 65μm spatial resolution. We present the first application of this new approach to articular cartilage, where our sample and silicon wafer are encapsulated by two plastic coverslips to maintain sample hydration and structural integrity. We show that the THz permittivity in this material varies progressively from the superficial zone to the deep layer, and that this correlates with a change in orientation of the collagen fibrils that compose the structure of the tissue. Our approach enables direct interrogation of the biophysical properties of the sample, in this case concerning the structure and permittivity of collagen fibrils and their anisotropic organisation in connective tissue.

Here, we take images, using the Hadamard encoding scheme §3.4.2.2, at each temporal point resulting in a hypertemporal stack of images. These stacks are shown

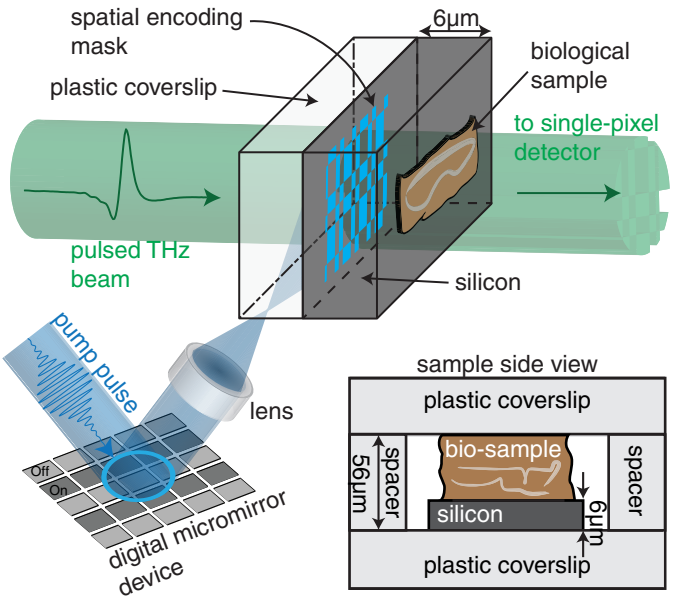

Figure 8.1: An optical pump pulse is spatially modulated and used to photoexcite a thin silicon wafer, which, in turn, transfers the spatial encoding mask onto a coincident THz pulse. The subsequent THz pulse is then passed through a biological sample onto a time-gated, single-element detector. By varying the arrival time of the electro-optic sampling pulse, we measure the full temporal trace of our THz waveform.

in videos V2 and V3 where we present the raw data used to extract the permittivity of the cartilage sample for horizontal and vertical polarization, respectively. A pair of still images from the two videos are shown in Fig. 8.2. A technical note is that we cannot assume a homogenous beam. For this reason, our reference is recorded for each pixel, performing the same measurement on the same system without the sample in place. After Fourier transformation of the time axis, one can divide signal by reference to obtain the frequency dependent amplitude transmission coefficients. These are then equated to the transmission functions of the system, calculated using the transfer matrix method, §3.2.1.

8.1 Plane wave analysis

A standard approach to analyzing THz-TDS spectra is to extract the complex permittivity (or equivalent) via analysis of the Fresnel transmission equations [86] (see §3.2.1). However, this approach assumes a plane wave approximation, something that is questionable for the near field. In this section, we test the validity of such an

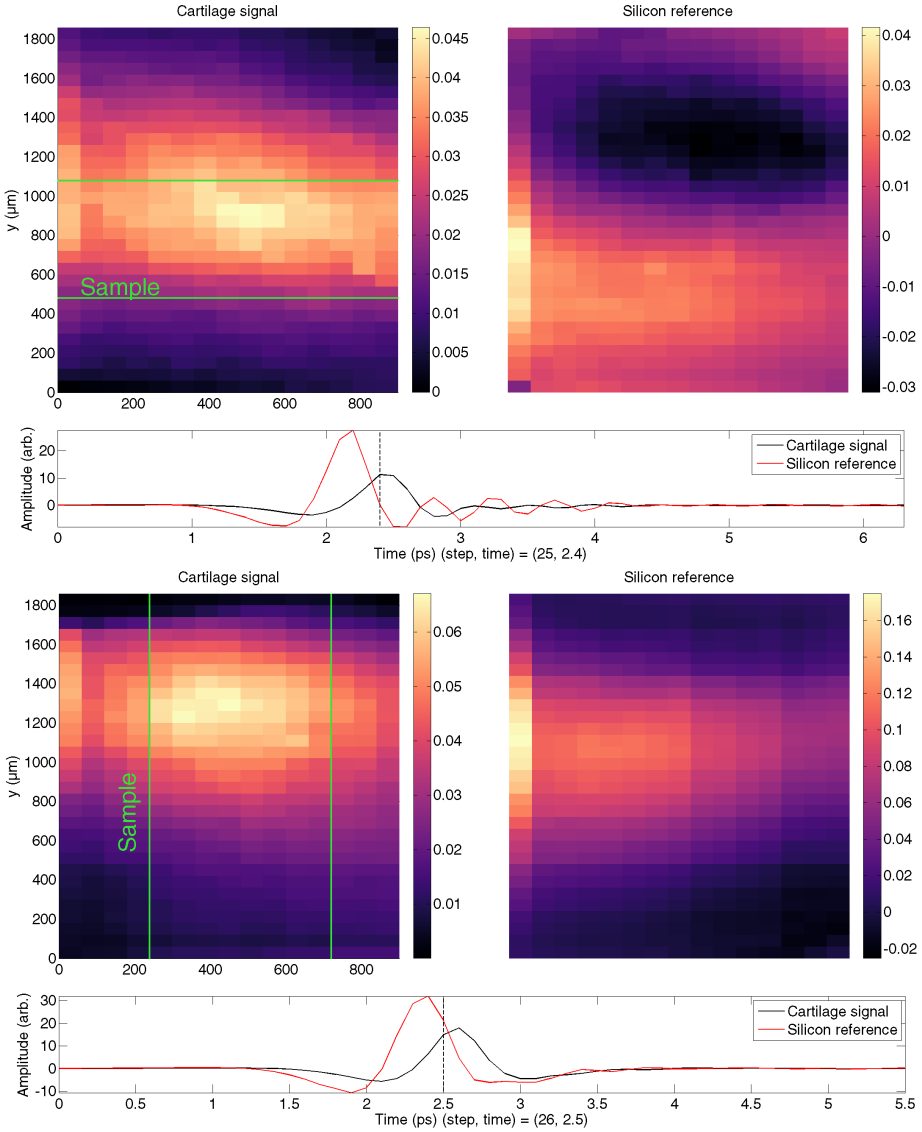

Figure 8.2: Still images from supplementary videos S1 and S2 on the top and bottom, respectively. In both cases, a temporal trace of our averaged signals is shown below the two colourmaps. A vertical dashed line shows the time at which the above colourmaps have been taken at $(\sim 2.5ps)$. The location of the sample is indicated by the green lines on left colourmap. Each image takes 31 minutes to acquire. The total measurement time was 50 hours.

approximation to our experimental approach.

We analytically model a system similar to that in our experiment (full mathematical details §2.2.2). In brief, we analyze the transmission through a single aperture in a conducting film in contact with a lossy dielectric layer of thickness h, as represented

in Fig. 8.3a. Here, the region with the aperture is tailored to have similar transmissive properties to those of the experimental photomodulator, while the lossy dielectric is given a permittivity ε. We set the permittivity of the incident and transmitted regions to $\varepsilon_s = 2.5$, i.e. similar to that of the plastic coverslips encapsulating our sample. Using a modal matching model §2.2.2 which assumes an incident THz plane wave, we simulate experiment by finding the transmitted far field for the two cases where $\varepsilon = 7.5 + 2i$ (i.e. similar to our cartilage sample discussed below) and $\varepsilon = 1$ (representing our reference). To replicate the multi-aperture approach used in our experiment, we carry out a complex summation of fields transmitted through different sized apertures. This is also emulated in the model by calculating the transmission for a discrete range of values of aperture sizes (w ranges between 40μm and 700μm) and then carrying out the complex summation of these fields. The final field is then processed in the same manner to the experimentally measured fields, as described in §3.2.1, so as to extract a frequency dependent permittivity of the sample layer. By comparing the extracted permittivity to that introduced in the model, we can assess the validity of the plane wave approximation.

In Fig. 8.3b, we plot the real and imaginary parts of the recovered permittivity versus frequency for three different sample thicknesses. We see that at higher frequencies, the recovered permittivity is generally very close to the input value used in the model. However, a greater discrepancy is found at lower THz frequencies, pronounced in both real and imaginary parts of the permittivity. This discrepancy arises from the presence of near fields, which are neglected in the plane wave approximation made to extract the permittivity. The longer decay lengths of the low frequency evanescent field components [77] lead to a greater discrepancy than the high frequency fields. We also see that the thin samples exhibit greater discrepancy: for thinner samples, the amplitude of evanescent field components at the exit interface is larger.

To further understand the shortcomings of the far-field approximation, in Figs. 8.4a) & b) we plot the relative error of the recovered permittivity, defined as $|(\varepsilon_{\text{recov}} - \varepsilon_{\text{input}})/\varepsilon_{\text{input}}|$, for our frequency range as we vary aperture size and sample height respectively. These plots show that the permittivity extraction procedure becomes more applicable as aperture size and sample thickness are increased. In Fig. 8.4a) we see two frequency independent maxima centered around 0.6 and 1.4THz, the strengths of which decrease with aperture size. In part b) we see the frequency of these same maxima changing with sample height. These maximal errors arise at the

Fabry-Perot resonances of the system. The far-field approximation used in permittivity extraction miscalculates these resonant frequencies due to the presence of evanescent fields, which change the impedance of each interface.

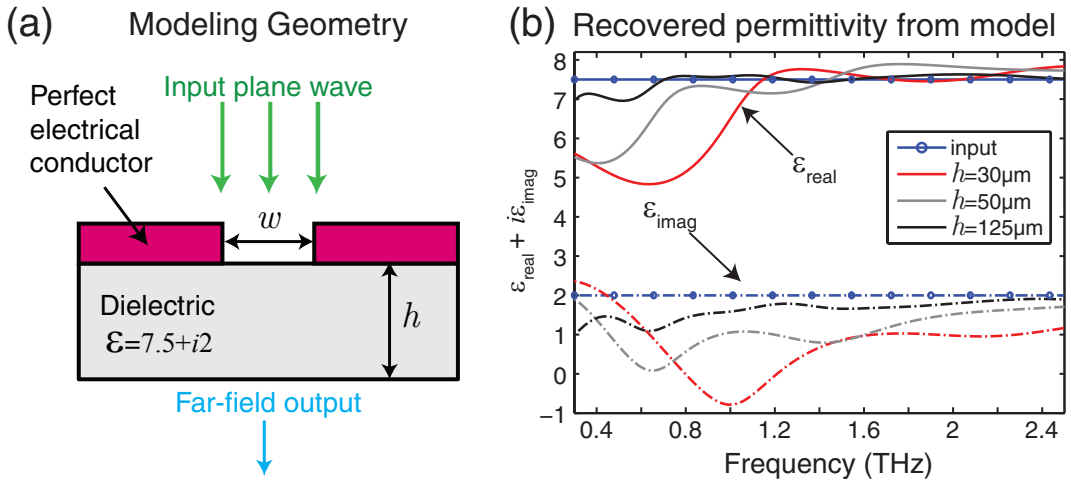

Figure 8.3: ***a*** *Side view of the modelling geometry; a plane wave is incident upon a single aperture placed on top of a dielectric.* ***b*** *The permittivity recovered from our model for three different dielectric thicknesses of 30, 50 and 125μm. We calculate the far-fields transmitted through apertures of sizes from 40 to 700μm, then we perform the complex summation of these fields. This is then inputted into our permittivity extraction procedure.*

One should note that discrepancies due to the plane wave approximation are expected to be less severe in our experiment, owing to the much lower, finite conductivity of the photomodulator [133, 142], which will act to relax the aperture boundary conditions [143] and reduce the amplitude of evanescent field components. Nevertheless, for sample thicknesses on the order of μm (such as those used in the experiment), one has to question the validity of the plane wave approximation at low THz frequencies. For this reason, we do not consider the very low frequency part of our spectra, below $\sim 0.6THz$. Note that for higher resolution images or thinner samples, one needs to develop a more elaborate analysis procedure, incorporating all near field effects, in order to reliably extract values of local permittivity.

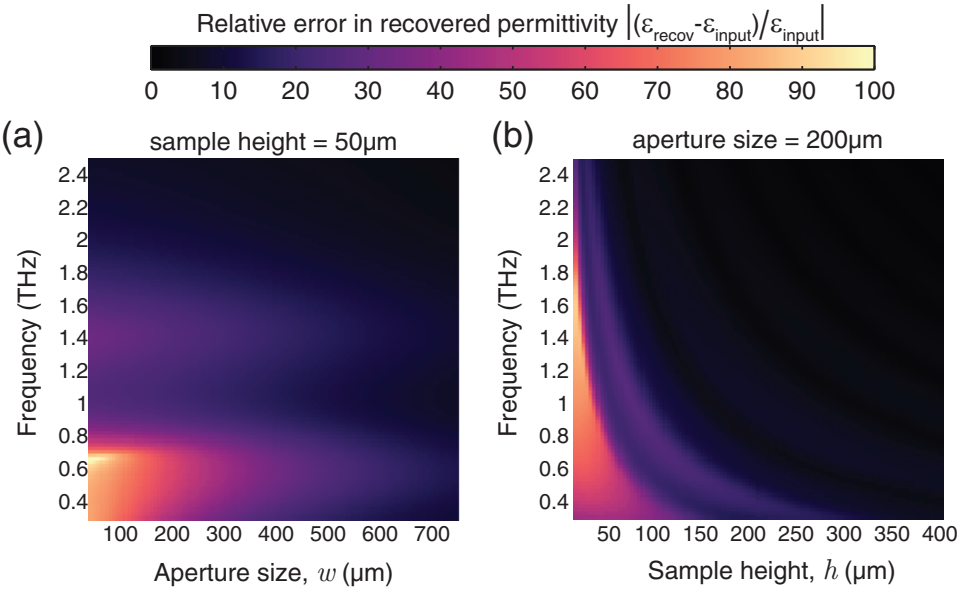

Figure 8.4: (a) & (b) Colour plots of the percentage error in the recovered permittivity over our frequency regime. In part a) we vary aperture size and keep sample height constant at 50μm, where as in part b) we vary sample height for an aperture size of 200μm.

8.2 Sample

Articular cartilage is a connective tissue composed of a dense extracellular matrix (ECM) rich in water, collagen and proteoglycans, with sparse specialised cells called chondrocytes [144]. It provides a smooth and lubricated surface for articulation and facilitates the transmission of loads through the distinctive regional orientation of the collagen fibrils, showing a change in fibril alignment going from the articular surface through to deeper within the tissue. For this reason, cross-sections of articular cartilage are suitable candidates to test the capabilities of the THz imaging technique with polarization resolution. The thin superficial zone is made primarily of collagen fibrils aligned parallel to the articular surface, whilst the middle zone is composed of thicker collagen fibrils with an oblique alignment, and the deep zone consists of collagen fibrils aligned orthogonal to the articular surface [145]. Clinical conditions such as osteoarthritis are characterized by degradation of the cartilage matrix, resulting in a disruption of the organised collagen structure [146]. Techniques that are able to detect changes in structure at the fibril level have potential for diagnosis of these pathologies.

Sample preparation

Bovine metacarpophalangeal joint cartilage was obtained from a local abattoir and washed in phosphate-buffered saline (PBS; pH 7.4) before cryosectioning. A cartilage segment was immersed in Bright cryo-m-bed compound and frozen before cryosections were cut. Cross-sections of cartilage were cut perpendicular to the articular surface and analyzed. The geometry of the section was recorded in polarized light microscope images, obtained using a 10X objective on a standard polarized light microscope and a CCD camera (QImaging Retiga 2000R).

8.3 Results and Discussion

Fig. 8.5a shows a photomicrograph of a cross-section of our articular cartilage sample taken with a polarized visible light microscope. The sample contains three main regions with distinct orientations of the collagen fibrils, similar to samples studied previously with other imaging techniques [147, 148]. In the superficial zone, collagen fibrils are aligned parallel to the articular surface. In the middle zone, the fibrils have an oblique arrangement, then ending orthogonal to their starting alignment in the deep zone, which presents high intensity of the transmitted polarized light. While articular cartilage has a collagen ultrastructure with spatial dimensions $\sim 100nm$ [149] which cannot be resolved here, we concern ourselves primarily with resolving orientation of the collagen fibrils which also occurs on a subwavelength scale for THz radiation.

Figs. 8.5b-e show the subwavelength THz response of cartilage measured with polarization parallel and perpendicular to the articular surface. Measurements were performed at discrete locations, from the superficial through to the deep zone, encompassing the different orientations of the collagen fibrils indicated in Fig. 8.5a. As a comparison, we also plotted the permittivity of the sample measured in the far field (i.e. a spatial average measured through the entire sample) and the permittivity of pure water (taken from ref. [50]). Note that water alone accounts for nearly 80% of the wet weight of articular cartilage [144], and that, due to the THz diffraction limit, the far-field spatially averaged measurement is carried out over a sample length of $\sim 0.5mm$, a length scale over which both the protein concentration and fibril orientation can be expected to vary substantially, owing to the heterogeneity of the biological sample on a micro-scale. The water spectral response shows a decreasing

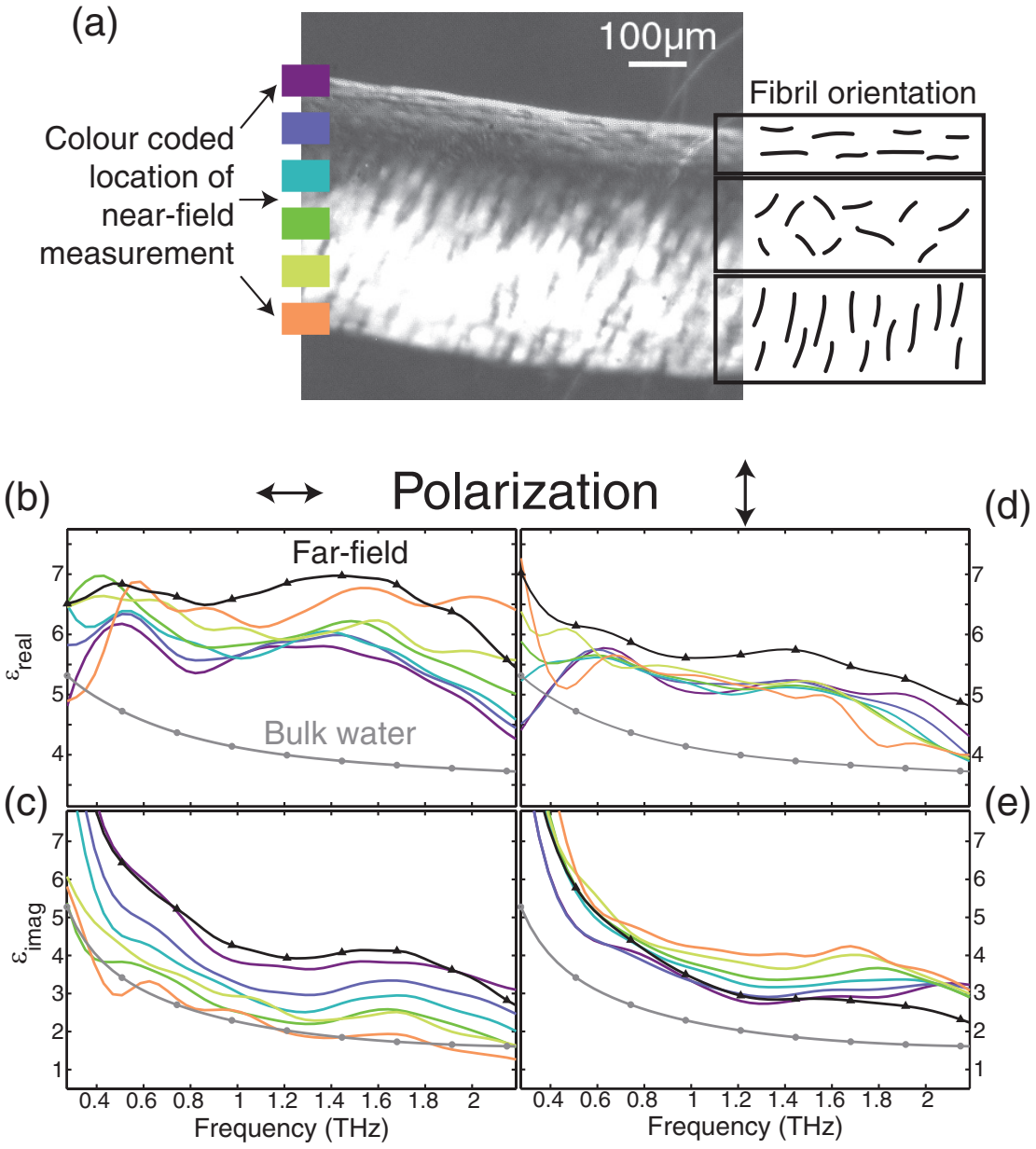

Figure 8.5: ***a*** *Photomicrograph and schematic diagram of a cross-section of bovine articular cartilage taken with polarization microscope (Nikon Elclipse E200) at* 45° *to the articular surface. Boxes of different colour indicate locations from which THz measurements were taken.* ***b*** *&* ***c*** *(****d*** *&* ***e****) Real and imaginary part, respectively, of the sample's dielectric function for horizontally (vertically) polarized incident THz beam. Bulk water data from fit parameters of Ref. [50]. The raw THz data can be seen in the supplementary videos.*

permittivity with increasing frequency [50]. However, both the spatially averaged and subwavelength THz response at all points across the depth of the cartilage exhibit broad features that are not apparent in the spectrum of pure water. Here, the broad peak at $\sim 1.5THz(50cm^{-1})$ in the real part of the permittivity spectrum ($\sim 1.7THz$ in the imaginary part) is not due to bulk water and hence, is a feature associated with hydration water and the fibrils themselves (note that the smaller oscillatory peaks in the spectrum are artefacts of the finite Fourier transform used in the analysis, depending on the temporal length of the THz measurement).

When we compare the cartilage's local permittivity, measured as a function of the distance from the superficial zone to the deep layer, to the spatially averaged measurement, we see a number of striking traits. Firstly, for horizontal THz polarization (Figs. 8.5b-c), the real part of the THz permittivity *increases* going from the superficial to the deep zone (top to bottom in Fig. 8.5a), whilst the imaginary part *decreases*. This indicates that the sample is most polarizable when the THz field is oriented along the fibril direction, i.e. in the superficial zone, and suggests that the collagen fibrils have a THz frequency dipole moment oriented along their principal axis. This assignment is corroborated by measurements with THz polarization rotated by 90 degrees (Figs. 8.5d-e): here the spatial dependence of the permittivity is essentially reversed and the sample is most polarizable at a deep location where the THz field is oriented along the fibril axis. It has been shown that proteins have low-frequency vibrational modes in the far-IR region [150], as well as coupled solute–solvent modes from the solvated solute [151]. For a biological tissue such as cartilage, both fibrous type-II collagen and water in proximity to the protein (i.e. hydration water), may contribute to the total THz response. Markelz et al. have shown that collagen (lyophilised powder) has a rapidly increasing absorbance with increasing frequency in the range 0.3 to $\sim 1.25THz$ [19]. Our data are in line with those findings, and we speculate that this broad absorption band is associated with the intermolecular structure of collagen. The strong dependence of the spectral response upon the THz field polarization, which is stronger when the fibrils are aligned parallel to one another, is yet to be explained. Further studies of the localized polarization-sensitive THz response observed here could provide greater insight in regards to the dynamics of this system.

Conclusions

We have demonstrated for the first time subwavelength hyperspectral THz imaging of articular cartilage using the photoconductive properties of a silicon photomodulator. We study articular cartilage, composed of collagen which is the most abundant structural protein in the human body, and find that its THz dielectric function varies on a sub-THz wavelength scale depending on collagen fibril orientation, which indicates the presence of a THz dipole moment along the primary axis of the fibril. We point out that such a detailed observation is impossible to deduce from far-field measurements, demonstrating the value of this subwavelength approach in regards to the diagnosis of pathologies that alter the collagen structure. It is interesting to note that, since the fundamental imaging resolution limit of our measurement is determined by diffraction of the optical pump pulse, we believe that our approach, where visible resolution may even be possible, holds promise as a future microscopy tool with potential for applications in the biomedical sciences, even on subcellular scales. Furthermore, this technique can be applied to sectioned tissue samples for THz diagnosis of diseases, such as cancer [16], with the sub-wavelength resolution would allowing detection of the disease at an earlier smaller stage.

Chapter 9

Conclusions and future work

This thesis demonstrates how spatial modulation of THz radiation can be induced with photoconductivity and then be used for near-field imaging. Chapter 1 deals with the properties of THz radiation that render it an interesting research topic nowadays. From non-destructive inspections of space shuttle panels and complex electronic circuits to non-ionizing medical diagnosis capabilities and the identification of chemicals, the potential uses of THz radiation are vast. However, as outlined in ch. 1, our THz generation and detection technologies are still too cumbersome and expensive for many applications to be realized effectively. Chapter 2 deals with background electromagnetic theory needed to understand this thesis; from a Fabry-Perot resonance and the Drude model of conduction to the THz material response of common matter and the diffraction theories used for modeling in the latter chapters. Chapter 3 outlines the experimental setup, a THz-TDS using a pair of ZnTe crystals for generation and detection, and how to image with a single element detector. Further, it also gives the background theory of imaging with a single-element detector and how to implement this is our setup. Chapter 4 is where the work of this thesis begins; near-field imaging of a 1D system, a sub-wavelength slit. We use a pair of photoexcited stripes to create a near-field interference pattern at our sub-wavelength slit. Under certain conditions we show the transmission through the slit can be enhanced or diminished. This shows that optically generated conductive patterns in silicon can be used to manipulate the THz near-fields. Chapter 5 demonstrates that the thickness of photomodulator limits the resolution of our imaging system, and that by reducing the thickness we can achieve $\lambda/45$ resolution. Further, we demonstrate how polarization effects can be used to one's advantage by imaging $8\mu m$ breaks in circuit board hidden by $115\mu m$ of

silicon. Chapter 6 concerns itself with the type of noise in this system. An evaluation of how different spatial encoding schemes perform under our experimental conditions is carried out. Further, some spatial encoding schemes allow for under-sampling of the scene to performed, hence we carry out a investigation of how different methods perform when the number of measurements is fewer than the number of pixels. Note this is experimentally performed with sub-wavelength objects, and undersampling with near-field resolution is quite unusual. Chapter 7 shows an interesting application of mapping out the photoconductivity of a graphene sample with 75μm resolution, however note that the fundamental resolution limit is set by visible-light diffraction. We compare our THz photoconductivity maps with Raman spectroscopy and find there to be a correlation between carrier density and THz photoconductivity. We believe this is due to inhomogenouties and defects created during the manufacturing process. Measuring the photoconductivity is an important characteristic for opto-electronic applications. However, extracting it from Raman spectroscopy is a difficult post-processing procedure where as our technique performs a direct measurement of it. Chapter 8 is, perhaps, the ultimate culmination of this imaging technique; hyperspectral THz imaging of biological matter with sub-wavelength resolution. Our sample is articular cartilage made of long collagen fibrils that change their orientation on a sub-THz wavelength scale. We find that the permittivity changes through our sample and sub-THz wavelength scale and find it correlated with orientation of the collagen fibrils. Note that although successful, the current THz permittivity extraction procedures assume a plane-wave approximation. We show this to be invalid for some parts of our spectrum but it is valid for the most part.

Whilst successful, there is a major problem that needs to be eradicated in order to make the measurements demonstrated in this thesis to be easily accessible for others. High optical pump powers are needed to make silicon an efficient photo-modulator for THz radiation. This necessitates the use of a high-power amplified Ti:sapphire laser system. This system has a lot of noise and its low-repetition rate both combine to create slow acquisition rates, hours for a single image. It is also exceedingly expensive. Therefore cheaper efficient THz photo-modulators are needed as well as stable THz sources and detectors. Furthermore, the temporal synchronization between optical pump and THz probe pulse must not be lost else carrier diffusion will limit the achievable resolution, and the ability to study picosecond dynamics at broadband spectral ranges is also highly desired. This renders continuous-wave

sources unusable.

Recent work by prof. MacPherson's group [152] has shown how a conductive interface in a total internal reflection geometry can be exploited to achieve high modulation over a broadband THz range. Further, this modulation technique requires optical fluencies a few orders of magnitude less than those used in this thesis. Hence, the next step will be to combine the imaging techniques presented in ch. 5 with the modulation geometry of reference [152]. This will create a practical, cost-effective THz modulator for imaging. The next thing will be to use the total internal reflection geometry in a near-field configuration. Since much smaller excitation powers are needed the use of cheaper, high-rep rate fibre coupled femtosecond laser systems is possible. These systems are more robust, have less noise and allow of the detection of a picosecond THz pulse. Such lasers will improve the acquisition rate, retain the temporal synchronization between all pulses and allow for the investigations of picosecond dynamics with broadband spectral ranges. Another curiosity is that ref. [152] predicts that the amplitude reflection coefficient in a total internal reflection geometry can be +1 and -1. This discards the need for a Lock-In amplifier to achieve an orthogonal measurement, as discussed in §3.4.2.2, thereby halving the total number of masks that need to be projected.

Appendix A

Modal Matching

Below is the full modal matching script used for calculations of §2.2.2 as printed out by Wolfram Mathematica 9.

Note that the script is written for a periodic system as opposed to a single slit as it outlined in §2.2.2. This means the integrals over wavevector become a Fourier-Floquet sum. In other words,

$$\int_{-\infty}^{\infty} A(u_x) e^{ik_z(u_x)z} e^{iu_x x} \mathrm{d}u_x \rightarrow \sum_{m=-\infty}^{\infty} A^m e^{ik_z^m z} e^{i\frac{2\pi m}{d}x}, \tag{A.1}$$

where d is the pitch and $k_z^m = \sqrt{k_0^2 - \left(\frac{2\pi m}{d}\right)^2}$. Intuitively, making the period tend to infinity and summing over large values of m (including many diffracted orders), then the behavior of the periodic system becomes the same as the single slit case. Alternatively, one can think of this as evaluating the integral via a Riemann sum where the lengths of the different intervals between every consecutive point is given by $\frac{2\pi m}{d}$, hence increasing the pitch increases the number of rectangles. There are two reasons we have evaluated our integrals this way. First, periodic structures are very easily modeled in finite element software packages, such as COMSOL, hence this gives a way of checking our calculations. Second, this method was found to be very quick and efficient compared to other numerical integral evaluation techniques. Further, it gave the same values as other the evaluation techniques built into Mathematica 9.

```
(***Fields***)
ClearAll["Global`*"]

(*Incoming plane wave*)
Ex1 := Ex Exp[i kz[0] z] + Rx[n] Exp[i 2 π n / d x] Exp[-i kz[n] z];
Ey1 := 0; (*Is zero*)
Ez1 = ∫ (-D[Ex1, x] - D[Ey1, y]) dz;
Hx1 = FullSimplify[-1/(i * ω) * Expand[(D[Ez1, y] - D[Ey1, z])]]
Hy1 = FullSimplify[-1/(i * ω) * Expand[(D[Ex1, z] - D[Ez1, x])]]
```

0

$$\frac{1}{d^2\,\omega\,kz[n]}e^{-i\,z\,kz[n]}\left(-d^2\,e^{i\,z\,(kz[0]+kz[n])}\,Ex\,kz[0]\,kz[n]+e^{\frac{2\,i\,n\,\pi\,x}{d}}\left(4\,n^2\,\pi^2+d^2\,kz[n]^2\right)Rx[n]\right)$$

$$\frac{1}{d^2\,\omega\,kz[n]}e^{-i\,z\,kz[n]}\left(-d^2\,e^{i\,z\,(kz[0]+kz[n])}\,Ex\,kz[0]\,kz[n]+e^{\frac{2\,i\,n\,\pi\,x}{d}}\left(4\,n^2\,\pi^2+d^2\,kz[n]^2\right)Rx[n]\right)$$

```
(***Field Description***)
wm := 2 a - wp;
β := a + wp / 2 + ws / 2;
a = 2;
wp = 1;
ws = 4;
Plot[UnitBox[x/wm], {x, -10, 10}]
Clear[wm, β, a, wp, ws]
```

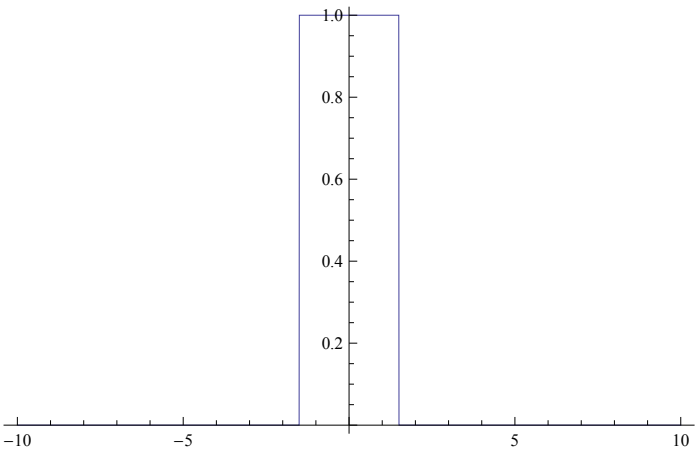

```
(*Middle Slit*)
Ex2m = ( Bm1 Exp[i kzsi1 z] - Bm2 Exp[-i kzsi1 z]) UnitBox[x/wm];
Ey2m = 0;
Ez2m = 0 ∫(-D[Ex2m, x] - D[Ey2m, y]) dz;
Hx2m = -1/(i * ω) Simplify[(D[Ez2m, y] - D[Ey2m, z])]
Hy2m = -1/(i * ω) * Simplify[(D[Ex2m, z] - D[Ez2m, x])]
```

```
0
```

$$-\frac{1}{\omega}e^{-i\,kzsi1\,z}\left(Bm2+Bm1\,e^{2\,i\,kzsi1\,z}\right)\,kzsi1\,UnitBox\left[\frac{x}{wm}\right]$$

```
(*Silicon Region*)
Ex3 = Si1[n] Exp[i 2 π n/d x] Exp[i kzsi[n] (z - hp)] +
    Si2[n] Exp[i 2 π n/d x] Exp[-i kzsi[n] (z - hp)];
Ey3 = 0;
Ez3 = ∫(-D[Ex3, x] - D[Ey3, y]) dz;
Hx3 = -1/(i * ω) * Simplify[(D[Ez3, y] - D[Ey3, z])]
Hy3 = -1/(i * ω) * Simplify[(D[Ex3, z] - D[Ez3, x])]
```

```
0
```

$$-\left(e^{i\left(\frac{2\,n\,\pi\,x}{d}+(-hp+z)\,kzsi[n]\right)}\left(4\,n^2\,\pi^2+d^2\,kzsi[n]^2\right)\left(Si1[n]-e^{2\,i\,(hp-z)\,kzsi[n]}\,Si2[n]\right)\right)\Big/\left(d^2\,\omega\,kzsi[n]\right)$$

```
(*Transmitted space*)
Ex4 = Tx[n] Exp[i 2 π n/d x] Exp[i kz[n] (z - hp - hsi)];
Ey4 = 0;
Ez4 = ∫(-D[Ex4, x] - D[Ey4, y]) dz;
Hx4 = -1/(i * ω) * Simplify[(D[Ez4, y] - D[Ey4, z])]
Hy4 = -1/(i * ω) * Simplify[(D[Ex4, z] - D[Ez4, x])]
```

```
0
```

$$-\frac{1}{d^2\,\omega\,kz[n]}e^{\frac{2\,i\,n\,\pi\,x}{d}-i\,(hp+hsi-z)\,kz[n]}\left(4\,n^2\,\pi^2+d^2\,kz[n]^2\right)\,Tx[n]$$

(***Matching E-Fields*****)**

z = 0;

Ex1

Ey1

Ex2m

Ey2m

$$Ex + e^{\frac{2 i n \pi x}{d}} Rx[n]$$

$$0$$

$$(Bm1 - Bm2)\ UnitBox\left[\frac{x}{wm}\right]$$

$$0$$

$$\mathbf{Ex + e^{\frac{2 i n \pi x}{d}} Rx[n] = (Bm1 - Bm2)\ UnitBox\left[\frac{x}{wm}\right];}$$

$$\mathbf{Ex\ d\ \delta[n] + d\ Rx[n] = (Bm1 - Bm2)\ Qm[n]}$$

(*Where*)

$$\mathbf{Qm[n] := \int_{-\infty}^{\infty} UnitBox\left[\frac{x}{wm}\right] Exp\left[-i\ \frac{2\ \pi\ n}{d}\ x\right] dx;}$$

z = hp;

Ex3

Ey3

Ex2m

Ey2m

$$e^{\frac{2 i n \pi x}{d}} Si1[n] + e^{\frac{2 i n \pi x}{d}} Si2[n]$$

$$0$$

$$\left(-Bm2\ e^{-i\ hp\ kzsi1} + Bm1\ e^{i\ hp\ kzsi1}\right) UnitBox\left[\frac{x}{wm}\right]$$

$$0$$

$$\mathbf{d\ (Si1[n] + Si2[n]) = \left(-Bm2\ e^{-i\ hp\ kzsi1} + Bm1\ e^{i\ hp\ kzsi1}\right) Qm[n];}$$

z = hp + hsi;

Ex4

Ey4

Ex3

Ey3

$$e^{\frac{2 i n \pi x}{d}} Tx[n]$$

0

$$e^{\frac{2 i n \pi x}{d} + i\, hsi\, kzsi[n]} Si1[n] + e^{\frac{2 i n \pi x}{d} - i\, hsi\, kzsi[n]} Si2[n]$$

0

$$e^{\frac{2 i n \pi x}{d}} Tx[n] = e^{\frac{2 i n \pi x}{d} + i\, hsi\, kzsi[n]} Si1[n] + e^{\frac{2 i n \pi x}{d} - i\, hsi\, kzsi[n]} Si2[n]$$

$$\int_{-d/2}^{d/2} e^{\frac{2 i n \pi x}{d}} dx$$

$$\frac{d\, Sin[n \pi]}{n \pi}$$

$$Tx[n] = e^{i\, hsi\, kzsi[n]} Si1[n] + e^{-i\, hsi\, kzsi[n]} Si2[n]$$

(***** Matching Fields are Middle Slit *******)**

z = 0;

Hx1

Hy1

Hx2m

Hy2m

0

$$\frac{1}{d^2\, \omega\, kz[n]} \left(- d^2\, Ex\, kz[0]\, kz[n] + e^{\frac{2 i n \pi x}{d}} \left(4\, n^2\, \pi^2 + d^2\, kz[n]^2 \right) Rx[n] \right)$$

0

$$- \frac{(Bm1 + Bm2)\, kzsi1\, UnitBox\left[\frac{x}{wm} \right]}{\omega}$$

$$\mathbf{Ex\,kz[0]\,wm - \sum_n Hm[n]\,\frac{(4\,n^2\,\pi^2 + d^2\,kz[n]^2)}{d^2\;kz[n]}\,Rx[n] = (Bm1 + Bm2)\,kzsi1\,wm}$$

(*Where*)

$$\mathbf{Hm[n] = \int_{-\infty}^{\infty} UnitBox\left[\frac{x}{wm}\right] Exp\left[i\,\frac{2\,\pi\,n}{d}\,x\right] dx;}$$

z = hp;
Hx3
Hy3
Hx2m
Hy2m

0

$$-\left(e^{\frac{2\,i\,n\,\pi\,x}{d}}\,\left(4\,n^2\,\pi^2 + d^2\,kzsi[n]^2\right)\,(Si1[n] - Si2[n])\right) \Big/ \left(d^2\,\omega\,kzsi[n]\right)$$

0

$$-\frac{1}{\omega}e^{-i\,hp\,kzsi1}\,\left(Bm2 + Bm1\,e^{2\,i\,hp\,kzsi1}\right)\,kzsi1\,UnitBox\left[\frac{x}{wm}\right]$$

$$\mathbf{\sum_n Hm[n]\,\frac{(4\,n^2\,\pi^2 + d^2\,kzsi[n]^2)}{d^2\;kzsi[n]}\,(Si1[n] - Si2[n]) =}$$
$$\mathbf{e^{-i\,hp\,kzsi1}\,\left(Bm2 + Bm1\,e^{2\,i\,hp\,kzsi1}\right)\,kzsi1\,wm}$$

(*Matching Silicon and Transmisted Space*)
z = hp + hsi;
Hx3
Hy3
Hx4
Hy4

0

$$-\left(e^{i\,\left(\frac{2\,n\,\pi\,x}{d} + hsi\,kzsi[n]\right)}\,\left(4\,n^2\,\pi^2 + d^2\,kzsi[n]^2\right)\,\left(Si1[n] - e^{-2\,i\,hsi\,kzsi[n]}\,Si2[n]\right)\right) \Big/ \left(d^2\,\omega\,kzsi[n]\right)$$

0

$$-\frac{e^{\frac{2\,i\,n\,\pi\,x}{d}}\,(4\,n^2\,\pi^2 + d^2\,kz[n]^2)\,Tx[n]}{d^2\,\omega\,kz[n]}$$

$$\mathbf{e^{\frac{2\,i\,n\,\pi\,x}{d}}\,\frac{(4\,n^2\,\pi^2 + d^2\,kz[n]^2)}{d^2\;kz[n]}\,Tx[n] =}$$
$$\mathbf{e^{\frac{2\,i\,n\,\pi\,x}{d}}\,\frac{e^{i\,(hsi\,kzsi[n])}\,(4\,n^2\,\pi^2 + d^2\,kzsi[n]^2)}{d^2\;kzsi[n]}\,\left(Si1[n] - e^{-2\,i\,hsi\,kzsi[n]}\,Si2[n]\right)}$$

$$\int_{-d/2}^{d/2} e^{\frac{2 i n \pi x}{d}} dx$$

$$\frac{d \, \text{Sin}[n \pi]}{n \pi}$$

$$\frac{(4 n^2 \pi^2 + d^2 kz[n]^2)}{d^2 \, kz[n]} Tx[n] = \frac{(4 n^2 \pi^2 + d^2 kzsi[n]^2)}{d^2 \, kzsi[n]} \left(Si1[n] \, e^{i (hsi \, kzsi[n])} - e^{-i \, hsi \, kzsi[n]} \, Si2[n]\right)$$

```
(***** Finding the Solution *****)

(* (* (* E-fields *) *) *)
Ex d δ[n] + d Rx[n] = (Bm1 - Bm2) Qm[n];

(*Rearragned top Eqn for Rx[n]*)
Rx[n] = ((Bm1 - Bm2) Qm[n] / d - Ex δ[n]);

d (Si1[n] + Si2[n]) = (-Bm2 e^(-i hp kzsi1) + Bm1 e^(i hp kzsi1)) Qm[n];

Tx[n] = (e^(i hsi kzsi[n]) Si1[n] + e^(-i hsi kzsi[n]) Si2[n]);

(* H-fields *)
Ex kz[0] wm - Σ_n Hm[n] (4 n^2 π^2 + d^2 kz[n]^2) / (d^2 kz[n]) Rx[n] = (Bm1 + Bm2) kzsi1 wm;

Σ_n Hm[n] (4 n^2 π^2 + d^2 kzsi[n]^2) / (d^2 kzsi[n]) (Si1[n] - Si2[n]) =
  e^(-i hp kzsi1) (Bm2 + Bm1 e^(2 i hp kzsi1)) kzsi1 wm;
```

$$\frac{(4\,n^2\,\pi^2 + d^2\,kz[n]^2)}{d^2\;kz[n]}\,Tx[n] =$$
$$\frac{(4\,n^2\,\pi^2 + d^2\,kzsi[n]^2)}{d^2\;kzsi[n]}\left(Si1[n]\,e^{i\,(hsi\,kzsi[n])} - e^{-i\,hsi\,kzsi[n]}\,Si2[n]\right)$$

```
(*

(*Simplified Equations with Si1[n] from E-fields substituded into H-fields,
that need be solved*)
(*And also from the E & H continuity
  equations at the exit surface of the silicon Si2[n]=0,
hence we end up with 6 equations we need to solve*)
```

$$Ex\;kz[0]\,wm - \sum_n Hm[n]\,\frac{(4\,n^2\,\pi^2+d^2\,kz[n]^2)}{d^2\;kz[n]}\left((Bm1-Bm2)\,\frac{Qm[n]}{d} - Ex\;\delta[n]\right) = (Bm1+Bm2)\;kzsi1\;wm;$$

$$\sum_n Hm[n]\,\frac{(4\,n^2\,\pi^2+d^2\,kzsi[n]^2)}{d^2\;kzsi[n]}\left(-Bm2\;e^{-i\,hp\,kzsi1} + Bm1\;e^{i\,hp\,kzsi1}\right)\,\frac{Qm[n]}{d} =$$
$$e^{-i\,hp\,kzsi1}\,\left(Bm2 + Bm1\;e^{2\,i\,hp\,kzsi1}\right)\;kzsi1\;wm;$$

$$\frac{(4\,n^2\,\pi^2+d^2\,kz[n]^2)}{d^2\;kz[n]}\,Tx[n] = \frac{(4\,n^2\,\pi^2+d^2\,kzsi[n]^2)}{d^2\;kzsi[n]}\left(Si1[n]\,e^{i\,(hsi\,kzsi[n])}\right);$$

```
(*Coefficient Definitions*)
```

$$HQ := \sum_n Hm[n]\,\frac{(4\,n^2\,\pi^2+d^2\,kz[n]^2)}{d^2\;kz[n]}\,\frac{Qm[n]}{d};$$
$$HQsi := \sum_n Hm[n]\,\frac{(4\,n^2\,\pi^2+d^2\,kzsi[n]^2)}{d^2\;kzsi[n]}\,\frac{Qm[n]}{d};$$

```
(*Eqs*)
```

$$2\;Ex\;kz[0]\,wm - HQ\,(Bm1-Bm2) = (Bm1+Bm2)\;kzsi1\;wm;$$
$$HQsi\left(-Bm2\;e^{-i\,hp\,kzsi1} + Bm1\;e^{i\,hp\,kzsi1}\right) = e^{-i\,hp\,kzsi1}\,\left(Bm2 + Bm1\;e^{2\,i\,hp\,kzsi1}\right)\;kzsi1\;wm;$$

```
*)
```

$$FullSimplify\left[Solve\left[\left\{\frac{(4\,n^2\,\pi^2 + d^2\,kz[n]^2)}{d^2\;kz[n]}\,Tx == \frac{(4\,n^2\,\pi^2 + d^2\,kzsi[n]^2)}{d^2\;kzsi[n]}\left(Si1\,e^{i\,(hsi\,kzsi[n])} - e^{-i\,hsi\,kzsi[n]}\,Si2\right),\; Tx == \left(e^{i\,hsi\,kzsi[n]}\,Si1 + Si2\,e^{-i\,hsi\,kzsi[n]}\right)\right\},\; \{Si1,\; Si2\}\right]\right]$$

$$\left\{\left\{Si1 \to \left(e^{-i\,hsi\,kzsi[n]}\,Tx\,(kz[n]+kzsi[n])\,\left(4\,n^2\,\pi^2+d^2\,kz[n]\,kzsi[n]\right)\right)\Big/\left(2\,kz[n]\,\left(4\,n^2\,\pi^2+d^2\,kzsi[n]^2\right)\right),\right.\right.$$
$$\left.\left.Si2 \to \left(e^{i\,hsi\,kzsi[n]}\,Tx\,(-kz[n]+kzsi[n])\,\left(-4\,n^2\,\pi^2+d^2\,kz[n]\,kzsi[n]\right)\right)\Big/\left(2\,kz[n]\,\left(4\,n^2\,\pi^2+d^2\,kzsi[n]^2\right)\right)\right\}\right\}$$

$$\mathbf{Si1 = \left(e^{-i\,hsi\,kzsi[n]}\,Tx[n]\,(kz[n]+kzsi[n])\,\left(4\,n^2\,\pi^2+d^2\,kz[n]\,kzsi[n]\right)\right)\Big/\left(2\,kz[n]\,\left(4\,n^2\,\pi^2+d^2\,kzsi[n]^2\right)\right);}$$

$$\mathbf{Si2 = \left(e^{i\,hsi\,kzsi[n]}\,Tx\,[n]\,(-kz[n]+kzsi[n])\,\left(-4\,n^2\,\pi^2+d^2\,kz[n]\,kzsi[n]\right)\right)\Big/\left(2\,kz[n]\,\left(4\,n^2\,\pi^2+d^2\,kzsi[n]^2\right)\right);}$$

```
FullSimplify[Si1 + Si2 ]
FullSimplify[Si1 - Si2 ]
```

$$\left(Cos[hsi\,kzsi[n]]-\left(i\,\left(4\,n^2\,\pi^2+d^2\,kz[n]^2\right)\,kzsi[n]\,Sin[hsi\,kzsi[n]]\right)\Big/\left(kz[n]\,\left(4\,n^2\,\pi^2+d^2\,kzsi[n]^2\right)\right)\right)\,Tx[n]$$

$$\left(\left(Cos[hsi\,kzsi[n]]\,\left(4\,n^2\,\pi^2+d^2\,kz[n]^2\right)\,kzsi[n]\right)\Big/\left(kz[n]\,\left(4\,n^2\,\pi^2+d^2\,kzsi[n]^2\right)\right)-i\,Sin[hsi\,kzsi[n]]\right)\,Tx[n]$$

```
(*Rearragned top Eqns for Rx[n] and Tx[n]*)
Rx[n] = ((Bm1 - Bm2) Qm[n]/d - Ex δ[n]);
```

$$d\left(\text{Cos}[\text{hsi}\,\text{kzsi}[n]] - \left(i\left(4n^2\pi^2 + d^2\,\text{kz}[n]^2\right)\text{kzsi}[n]\,\text{Sin}[\text{hsi}\,\text{kzsi}[n]]\right)\Big/ \left(\text{kz}[n]\left(4n^2\pi^2 + d^2\,\text{kzsi}[n]^2\right)\right)\right)\text{Tx}[n] = \left(-\text{Bm2}\,e^{-i\,\text{hp}\,\text{kzsi1}} + \text{Bm1}\,e^{i\,\text{hp}\,\text{kzsi1}}\right)\text{Qm}[n];$$

$$\text{Tx}[n] = \left(-\text{Bm2}\,e^{-i\,\text{hp}\,\text{kzsi1}} + \text{Bm1}\,e^{i\,\text{hp}\,\text{kzsi1}}\right)\frac{\text{Qm}[n]}{d}\left(\text{Cos}[\text{hsi}\,\text{kzsi}[n]] - \left(i\left(4n^2\pi^2 + d^2\,\text{kz}[n]^2\right)\text{kzsi}[n]\,\text{Sin}[\text{hsi}\,\text{kzsi}[n]]\right)\Big/ \left(\text{kz}[n]\left(4n^2\pi^2 + d^2\,\text{kzsi}[n]^2\right)\right)\right)^{-1};$$

```
(* H-fields *)
```

$$\text{Ex}\,\text{kz}[0]\,\text{wm} - \sum_{\text{hn}} \text{Hm}[n]\,\frac{\left(4n^2\pi^2 + d^2\,\text{kz}[n]^2\right)}{d^2\,\text{kz}[n]}\left((\text{Bm1} - \text{Bm2})\,\frac{\text{Qm}[n]}{d} - \text{Ex}\,\delta[n]\right) = (\text{Bm1} + \text{Bm2})\,\text{kzsi1}\,\text{wm};$$

$$\sum_{\text{hn}} \text{Hm}[n]\,\frac{\left(4n^2\pi^2 + d^2\,\text{kzsi}[n]^2\right)}{d^2\,\text{kzsi}[n]}\left(\left(\text{Cos}[\text{hsi}\,\text{kzsi}[n]]\left(4n^2\pi^2 + d^2\,\text{kz}[n]^2\right)\text{kzsi}[n]\right)\Big/\left(\text{kz}[n]\left(4n^2\pi^2 + d^2\,\text{kzsi}[n]^2\right)\right) - i\,\text{Sin}[\text{hsi}\,\text{kzsi}[n]]\right)\text{Tx}[n] = e^{-i\,\text{hp}\,\text{kzsi1}}\left(\text{Bm2} + \text{Bm1}\,e^{2\,i\,\text{hp}\,\text{kzsi1}}\right)\text{kzsi1}\,\text{wm};$$

```
FullSimplify[
  ((Cos[hsi kzsi[n]] (4 n^2 π^2 + d^2 kz[n]^2) kzsi[n])/(kz[n] (4 n^2 π^2 + d^2 kzsi[n]^2)) -
     i Sin[hsi kzsi[n]]) *
   (Cos[hsi kzsi[n]] - (i (4 n^2 π^2 + d^2 kz[n]^2) kzsi[n] Sin[hsi kzsi[n]])/
       (kz[n] (4 n^2 π^2 + d^2 kzsi[n]^2)))^-1]
```

$$\left(\text{Cos}[\text{hsi}\,\text{kzsi}[n]]\left(4n^2\pi^2 + d^2\,\text{kz}[n]^2\right)\text{kzsi}[n] - i\,\text{kz}[n]\left(4n^2\pi^2 + d^2\,\text{kzsi}[n]^2\right)\text{Sin}[\text{hsi}\,\text{kzsi}[n]]\right)\Big/\left(\text{Cos}[\text{hsi}\,\text{kzsi}[n]]\,\text{kz}[n]\left(4n^2\pi^2 + d^2\,\text{kzsi}[n]^2\right) - i\left(4n^2\pi^2 + d^2\,\text{kz}[n]^2\right)\text{kzsi}[n]\,\text{Sin}[\text{hsi}\,\text{kzsi}[n]]\right)$$

$$\sum_{n} Hm[n] \frac{\left(4\,n^2\,\pi^2 + d^2\,kzsi[n]^2\right)}{d^2\,kzsi[n]}$$
$$\left(\left(Cos[hsi\,kzsi[n]]\,\left(4\,n^2\,\pi^2 + d^2\,kz[n]^2\right)\,kzsi[n] - i\,kz[n]\,\left(4\,n^2\,\pi^2 + d^2\,kzsi[n]^2\right)\right.\right.$$
$$\left.\left.Sin[hsi\,kzsi[n]]\right) \Big/ \left(Cos[hsi\,kzsi[n]]\,kz[n]\,\left(4\,n^2\,\pi^2 + d^2\,kzsi[n]^2\right) - i\,\left(4\,n^2\,\pi^2 + d^2\,kz[n]^2\right)\,kzsi[n]\,Sin[hsi\,kzsi[n]]\right)\right)$$
$$\left(-Bm2\,e^{-i\,hp\,kzsi1} + Bm1\,e^{i\,hp\,kzsi1}\right)\,\frac{Qm[n]}{d} = e^{-i\,hp\,kzsi1}\,\left(Bm2 + Bm1\,e^{2\,i\,hp\,kzsi1}\right)\,kzsi1\,wm;$$

```
(*Coefficient Definitions*)
```

$$HQ := \sum_{n} Hm[n]\,\frac{\left(4\,n^2\,\pi^2 + d^2\,kz[n]^2\right)}{d^2\,kz[n]}\,\frac{Qm[n]}{d};$$

$$HQsi := \sum_{n} Hm[n]\,\frac{\left(4\,n^2\,\pi^2 + d^2\,kzsi[n]^2\right)}{d^2\,kzsi[n]}$$
$$\frac{Qm[n]}{d}\,\left(\left(Cos[hsi\,kzsi[n]]\,\left(4\,n^2\,\pi^2 + d^2\,kz[n]^2\right)\,kzsi[n] - i\,kz[n]\,\left(4\,n^2\,\pi^2 + d^2\,kzsi[n]^2\right)\,Sin[hsi\,kzsi[n]]\right) \Big/ \left(Cos[hsi\,kzsi[n]]\,kz[n]\,\left(4\,n^2\,\pi^2 + d^2\,kzsi[n]^2\right) - i\,\left(4\,n^2\,\pi^2 + d^2\,kz[n]^2\right)\,kzsi[n]\,Sin[hsi\,kzsi[n]]\right)\right);$$

```
(*Eqs*)
```

$$2\,Ex\,kz[0]\,wm - HQ\,(Bm1 - Bm2) = (Bm1 + Bm2)\,kzsi1\,wm;$$
$$HQsi\,\left(-Bm2\,e^{-i\,hp\,kzsi1} + Bm1\,e^{i\,hp\,kzsi1}\right) = e^{-i\,hp\,kzsi1}\,\left(Bm2 + Bm1\,e^{2\,i\,hp\,kzsi1}\right)\,kzsi1\,wm$$

```
FullSimplify[Solve[{2 Ex kz[0] wm - HQ (Bm1 - Bm2) == (Bm1 + Bm2) kzsi1 wm,
    HQsi (-Bm2 e^(-i hp kzsi1) + Bm1 e^(i hp kzsi1)) == e^(-i hp kzsi1) (Bm2 + Bm1 e^(2 i hp kzsi1)) kzsi1 wm},
  {Bm1, Bm2}]]
```

$$\left\{\left\{Bm1 \to -\frac{2\,Ex\,wm\,(HQsi + kzsi1\,wm)\,kz[0]}{e^{2\,i\,hp\,kzsi1}\,(HQ - kzsi1\,wm)\,(HQsi - kzsi1\,wm) - (HQ + kzsi1\,wm)\,(HQsi + kzsi1\,wm)},\right.\right.$$
$$\left.\left.Bm2 \to \frac{2\,e^{2\,i\,hp\,kzsi1}\,Ex\,wm\,(-HQsi + kzsi1\,wm)\,kz[0]}{e^{2\,i\,hp\,kzsi1}\,(HQ - kzsi1\,wm)\,(HQsi - kzsi1\,wm) - (HQ + kzsi1\,wm)\,(HQsi + kzsi1\,wm)}\right\}\right\}$$

$$\text{Qm[n]} = \left\{\int_{-wm/2}^{wm/2} \text{Exp}\left[-i\,\frac{2\pi n}{d}\,x\right] dx,\ \int_{-wm/2}^{wm/2} \text{Exp}\left[-i\,\frac{2\pi 0}{d}\,x\right] dx\right\}$$

$$\text{Hm[n]} = \left\{\int_{-wm/2}^{wm/2} \text{Exp}\left[i\,\frac{2\pi n}{d}\,x\right] dx,\ \int_{-wm/2}^{wm/2} \text{Exp}\left[i\,\frac{2\pi 0}{d}\,x\right] dx\right\}$$

$$\left\{\frac{d\,\text{Sin}\left[\frac{n\pi wm}{d}\right]}{n\pi},\ wm\right\}$$

$$\left\{\frac{d\,\text{Sin}\left[\frac{n\pi wm}{d}\right]}{n\pi},\ wm\right\}$$

```
ClearAll["Global`*"]
```

```
(* (* (* * * *   Calculations   * * * *) *) *)
(* (* (* Comparison with Comsol*) *) *)
```

```
nmax := 16;
Ex := 1;
d := 150 * 10^-6;
wm := 0.499 d;
c := 3 * 10^8;
hp := 1 * 10^-6;
hsi := 50 * 10^-6;
k0 := (2 π f * 10^12)/c;
z := hp + hsi + 0 * 10^-6;
eps := 1 + 0 i;
```

$$\text{kz[n\_]} := \sqrt{k0^2 - \left(\frac{2n\pi}{d}\right)^2}\ ;$$

$$\text{kzsi[n\_]} := \sqrt{eps * k0^2 - \left(\frac{2n\pi}{d}\right)^2}\ ;$$

$$\text{kzsi1} := \sqrt{eps * k0^2}\ ;$$

$$Qm[n\_] := If\left[n == 0,\ wm,\ \frac{d\ Sin\left[\frac{n\,\pi\,wm}{d}\right]}{n\,\pi}\right];$$

$$Hm[n\_] := If\left[n == 0,\ wm,\ \frac{d\ Sin\left[\frac{n\,\pi\,wm}{d}\right]}{n\,\pi}\right];$$

$$HQ := N\left[\sum_{n=-nmax}^{+nmax} Hm[n]\ \frac{(4\,n^2\,\pi^2 + d^2\,kz[n]^2)}{d^2\ kz[n]}\ \frac{Qm[n]}{d}\right];$$

$$HQsi := N\left[\sum_{n=-nmax}^{+nmax} Hm[n]\ \frac{(4\,n^2\,\pi^2 + d^2\,kzsi[n]^2)}{d^2\ kzsi[n]}\ \frac{Qm[n]}{d}\right.$$
$$\left((Cos[hsi\,kzsi[n]]\ (4\,n^2\,\pi^2 + d^2\,kz[n]^2)\ kzsi[n] - i\,kz[n]\ (4\,n^2\,\pi^2 + d^2\,kzsi[n]^2)\right.$$
$$Sin[hsi\,kzsi[n]])\ /\ (Cos[hsi\,kzsi[n]]\ kz[n]\ (4\,n^2\,\pi^2 + d^2\,kzsi[n]^2) -$$
$$\left.\left.i\ (4\,n^2\,\pi^2 + d^2\,kz[n]^2)\ kzsi[n]\ Sin[hsi\,kzsi[n]])\right)\right];$$

```
MatrixY = Table[0, {2}];
MatrixY = ReplacePart[MatrixY, 2 Ex kz[0] wm, 1];
```

```
mat = Array[0, {2, 2}];

Eqs = {
    -HQ (Bm1 - Bm2) - (Bm1 + Bm2) kzsi1 wm,
    HQsi (-Bm2 e^(-i hp kzsi1) + Bm1 e^(i hp kzsi1)) - e^(-i hp kzsi1) (Bm2 + Bm1 e^(2 i hp kzsi1)) kzsi1 wm
   };

Coeffs = {Bm1, Bm2};
Do[Do[
    mat = ReplacePart[mat, Coefficient[Eqs[[j]], Coeffs[[i]]], {j, i}];
    , {i, 1, 2, 1}], {j, 1, 2, 1}];
```

```
fmin = 0.1;
fmax = 5;
fpoints = 100;
df = N[(fmax - fmin) / (fpoints - 1), 5];

count = 1;
result = Array[0 &, fpoints];
```

```
AbsoluteTiming[
 Monitor[
   For[f = fmin, f ≤ (fmax + 0.3 * df), f += df,

    MatrixZ = LinearSolve[mat, MatrixY];
    Txf[n_] := ((-MatrixZ[[2]] e^(-i hp kzsi1) + MatrixZ[[1]] e^(i hp kzsi1)) Qm[n]/d
        (Cos[hsi kzsi[n]] - (i (4 n^2 π^2 + d^2 kz[n]^2) kzsi[n] Sin[hsi kzsi[n]])/
            (kz[n] (4 n^2 π^2 + d^2 kzsi[n]^2)))^-1) Exp[i kz[n] (z - hp - hsi)];

    result = ReplacePart[result, Txf[0], count];
    count += 1;
   ], {ProgressIndicator[(count - 1) / fpoints], N[100 * (count - 1) / fpoints]}];
]
CoolColor[z_] := Hue[0.71 - 0.75 z, 1, 0.1 + z^0.3];

(*Import Comsol data*)
SetDirectory[NotebookDirectory[]];
comsol = Import[
   "Comsol freq, S21 parameter, d=150um w=75um, f=0.1,5 points=100.csv"];

ListPlot[{Abs[result], comsol[[All, 2]]}, PlotRange → Full,
 DataRange → {fmin, fmax}, PlotLegends → {"Modal Matching", "Comsol"},
 Joined → True, AxesOrigin → {fmin, 0}, Joined → True,
 PlotLabel → "Modal matching Vs Comsol", Frame → True,
 FrameLabel → {"Frequency (THz)", "Transmission"}]
Abs[{N[(c * 10^-12)/(√eps d)], N[(c * 10^-12)/(√eps wm)]}]
```

```
{0.080005, Null}
```

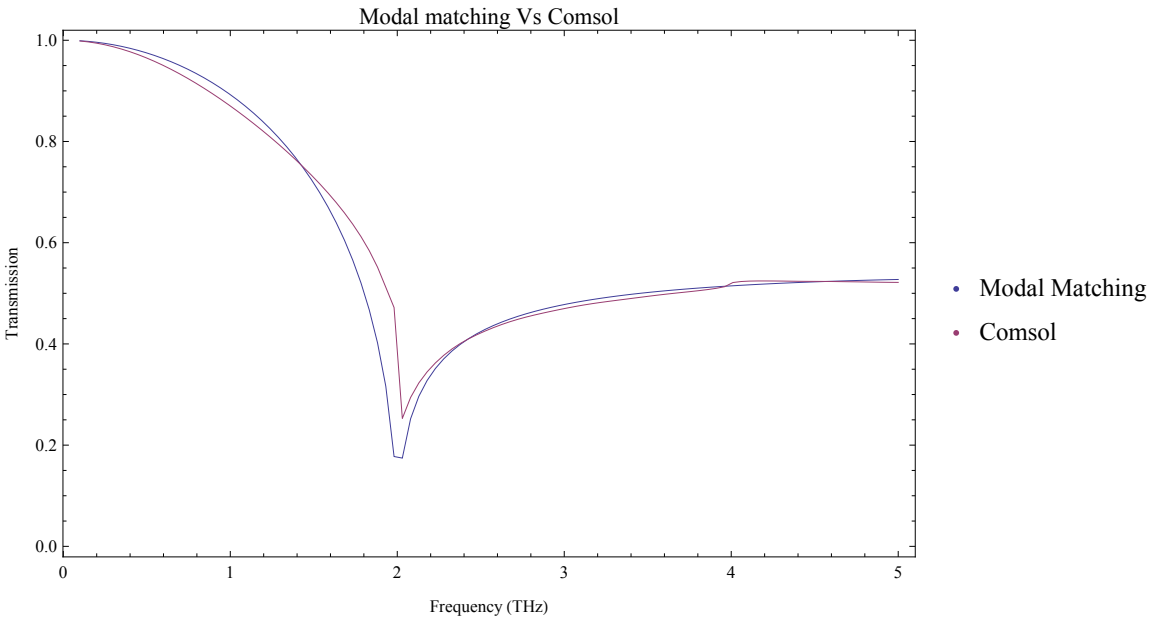
Modal matching Vs Comsol
Transmission
Frequency (THz)
1.0
0.8
0.6
0.4
0.2
0.0
0
1
2
3
4
5
Modal Matching
Comsol

```
{2., 4.00802}
```

References

[1] Kimmitt, M.F. Restrahlen to T-rays - 100 years of terahertz radiation. *Journal of biological physics*, **29**, 77 (2003). 1

[2] Chan, W.L., Deibel, J., and Mittleman, D.M. Imaging with terahertz radiation. *Reports on Progress in Physics*, **70**, 1325 (2007). 1

[3] Jansen, C., Wietzke, S., Peters, O., Scheller, M., Vieweg, N., Salhi, M., Krumbholz, N., Jördens, C., Hochrein, T., and Koch, M. Terahertz imaging: applications and perspectives. *Applied Optics*, **49**, E48 (2010).

[4] Ajito, K. and Ueno, Y. THz Chemical Imaging for Biological Applications. *IEEE Transactions on Terahertz Science and Technology*, **1**, 293 (2011). 1, 2

[5] Kampfrath, T., Tanaka, K., and Nelson, K.A. Resonant and nonresonant control over matter and light by intense terahertz transients. *Nature Photonics*, **7**, 680 (2013). 1

[6] Karpowicz, N., Zhong, H., Zhang, C., Lin, K.I., Hwang, J.S., Xu, J., and Zhang, X.C. Compact continuous-wave subterahertz system for inspection applications. *Applied Physics Letters*, **86**, 054105 (2005). 1

[7] Ahi, K. and Anwar, M. Advanced terahertz techniques for quality control and counterfeit detection. page 98560G (2016). 1

[8] Ahi, K. and Anwar, M. Modeling of terahertz images based on x-ray images: a novel approach for verification of terahertz images and identification of objects with fine details beyond terahertz resolution. page 985610. International Society for Optics and Photonics (2016). 1

[9] Ahi, K., Asadizanjani, N., Shahbazmohamadi, S., Tehranipoor, M., and Anwar, M. Terahertz characterization of electronic components and comparison of terahertz imaging with x-ray imaging techniques. page 94830K. International Society for Optics and Photonics (2015). 2

[10] Zeitler, J.A., Taday, P.F., Newnham, D.a., Pepper, M., Gordon, K.C., and Rades, T. Terahertz pulsed spectroscopy and imaging in the pharmaceutical setting–a review. *The Journal of pharmacy and pharmacology*, **59**, 209 (2007). 2

[11] Shen, Y.C. Terahertz pulsed spectroscopy and imaging for pharmaceutical applications: A review. *International Journal of Pharmaceutics*, **417**, 48 (2011). 2

[12] Konek, C., Wilkinson, J., Esenturk, O., Heilweil, E., and Kemp, M. Terahertz spectroscopy of explosives and simulants: RDX, PETN, sugar, and L-tartaric acid. page 73110K. International Society for Optics and Photonics (2009). 2

[13] Abraham, E., Younus, A., Delagnes, J.C., and Mounaix, P. Non-invasive investigation of art paintings by terahertz imaging. *Applied Physics A*, **100**, 585 (2010). 2

[14] Fitzgerald, A.J., Berry, E., Zinovev, N.N., Walker, G.C., Smith, M.A., and Chamberlain, J.M. An introduction to medical imaging with coherent terahertz frequency radiation. *Physics in Medicine and Biology*, **47**, R67 (2002). 2

[15] Tewari, P., Taylor, Z.D., Bennett, D., Singh, R.S., Culjat, M.O., Kealey, C.P., Hubschman, J.P., White, S., Cochran, A., Brown, E.R., and Grundfest, W.S. Terahertz imaging of biological tissues. *Studies in health technology and informatics*, **163**, 653 (2011). 2

[16] Yu, C., Fan, S., Sun, Y., and Pickwell-MacPherson, E. The potential of terahertz imaging for cancer diagnosis: A review of investigations to date. *Quantitative Imaging in Medicine and Surgery*, **2**, 33 (2012). 2, 106

[17] Korter, T., Balu, R., Campbell, M., Beard, M., Gregurick, S., and Heilweil, E. Terahertz spectroscopy of solid serine and cysteine. *Chemical Physics Letters*, **418**, 65 (2006). 2

[18] Rungsawang, R., Ueno, Y., Tomita, I., and Ajito, K. Terahertz notch filter using intermolecular hydrogen bonds in a sucrose crystal. *Optics express*, **14**, 5765 (2006). 2

[19] Markelz, A., Roitberg, A., and Heilweil, E. Pulsed terahertz spectroscopy of DNA, bovine serum albumin and collagen between 0.1 and 2.0 THz. *Chemical Physics Letters*, **320**, 42 (2000). 2, 105

[20] Simon Ebbinghaus, Seung Joong Kim, Matthias Heyden, Xin Yu, Martin Gruebele, David M. Leitner, and Martina Havenith. Protein Sequence- and pH-Dependent Hydration Probed by Terahertz Spectroscopy (2008). 2

[21] Leitner, D.M., Gruebele, M., and Havenith, M. Solvation dynamics of biomolecules: Modeling and terahertz experiments. *HFSP Journal*, **2**, 314 (2008). 2

[22] Markelz, A.G. Terahertz Dielectric Sensitivity to Biomolecular Structure and Function. *IEEE JOURNAL OF SELECTED TOPICS IN QUANTUM ELECTRONICS*, **14** (2008). 2

[23] Charles L. Brooks, Martin Karplus, and B. Montgomery Pettitt. *Proteins: A Theoretical Perspective of Dynamics, Structure, and Thermodynamics*, volume 143 of *Advances in Chemical Physics*. John Wiley & Sons, Inc., Hoboken, NJ, USA (2009). ISBN 9780470508602. 2

[24] Son, J.H. *Terahertz biomedical science & technology* (????). ISBN 9781466570443. 2

[25] Lee, Y.S. *Principles of terahertz science and technology*. Springer (2009). ISBN 9780387095394, Ch. 4.3. 2

[26] Bründermann, E., Chamberlin, D., and Haller, E. Novel design concepts of widely tunable germanium terahertz lasers. *Infrared Physics & Technology*, **40**, 141 (1999). 2

[27] Kundu, I., Dean, P., Valavanis, A., Chen, L., Li, L., Cunningham, J.E., Linfield, E.H., and Davies, A.G. Discrete Vernier tuning in terahertz quantum cascade lasers using coupled cavities. *Optics express*, **22**, 16595 (2014). 2

[28] Lee, Y.S. *Principles of terahertz Science and technology*. Springer (2009). ISBN 9780387095394, ch 4.8. 2

[29] Tani, M., Herrmann, M., Kono, S., and Sakai, K. Generation and detection of terahertz pulsed radiation with photoconductive antennas and their application to imaging. In *2002 International Topical Meeting on Microwave Photonics, MWP 2002 - Technical Digest*, pages 1–4 (2002). ISBN 4885521874. 2, 3

[30] Dexheimer, S.L. *Terahertz Spectroscopy: Principles and Applications* (2007). ISBN 142000770X, Ch. 2. 2, 3

[31] Dai, J., Liu, J., and Zhang, X.C. Terahertz Wave Air Photonics: Terahertz Wave Generation and Detection With Laser-Induced Gas Plasma. *IEEE Journal of Selected Topics in Quantum Electronics*, **17**, 183 (2011). 2

[32] Reimann, K. Table-top sources of ultrashort THz pulses. *Reports on Progress in Physics*, **1597**, 1597 (2007). 2

[33] Jördens, C., Schlauch, T., Li, M., Hofmann, M.R., Bieler, M., and Koch, M. All-semiconductor laser driven terahertz time-domain spectrometer. *Applied Physics B*, **93**, 515 (2008). 3

[34] Perenzoni, M. and Paul, D.J. (editors). *Physics and Applications of Terahertz Radiation*, volume 173 of *Springer Series in Optical Sciences*. Springer Netherlands, Dordrecht (2014). ISBN 978-94-007-3836-2, Ch. 2. 3

[35] Müller, R., Gutschwager, B., Hollandt, J., Kehrt, M., Monte, C., Müller, R., and Steiger, A. Characterization of a Large-Area Pyroelectric Detector from 300 GHz to 30 THz. *Journal of Infrared, Millimeter, and Terahertz Waves*, **36**, 654 (2015). 3

[36] Lee, Y.S. *Principles of terahertz science and technology* (2009). ISBN 9780387095394, Ch. 4.9.3. 3

[37] Hadi, R.A., Sherry, H., Grzyb, J., Zhao, Y., Förster, W., Keller, H.M., Cathelin, A., Kaiser, A., and Pfeiffer, U.R. A 1 k - Pixel Video Camera for 0 . 7 – 1 . 1 Terahertz Imaging Applications in 65 - nm CMOS. *IEEE JOURNAL OF SOLID - STATE CIRCUITS*, **47**, 2999 (2012). 3

[38] Al Hadi, R., Grzyb, J., Heinemann, B., and Pfeiffer, U.R. A Terahertz Detector Array in a SiGe HBT Technology. *IEEE Journal of Solid-State Circuits*, **48**, 2002 (2013). 3

[39] Escorcia, I., Grant, J., Gough, J., and Cumming, D.R.S. Uncooled CMOS terahertz imager using a metamaterial absorber and pn diode. *Optics Letters*, **41**, 3261 (2016). 3

[40] Darrow, J.T., Zhang, X.C., Auston, D.H., and Morse, J.D. Saturation Properties of Large-Aperture Photoconducting Antennas. *IEEE JOURNAL OF QUANTUM ELECTRONICS*, **28** (1992). 3

[41] Lee, Y.S. *Principles of terahertz science and technology* (2009). ISBN 9780387095394, Ch. 3.3.5. 3

[42] Clough, B., Dai, J., and Zhang, X.C. Laser air photonics: Beyond the terahertz gap. *Materials Today*, **15**, 50 (2012). 3

[43] Hunsche, S., Koch, M., Brener, I., and Nuss, M. THz near-field imaging. *Optics Communications*, **150**, 22 (1998). 3, 4, 46

[44] van der Valk, N.C.J. and Planken, P.C.M. Electro-optic detection of subwavelength terahertz spot sizes in the near field of a metal tip. *Applied Physics Letters*, **81**, 1558 (2002). 3

[45] Cocker, T.L., Jelic, V., Gupta, M., Molesky, S.J., Burgess, J.A.J., Reyes, G.D.L., Titova, L.V., Tsui, Y.Y., Freeman, M.R., and Hegmann, F.A. An ultrafast terahertz scanning tunnelling microscope. *Nature Photonics*, **7**, 620 (2013). 3, 46

[46] Huber, A.J., Keilmann, F., Wittborn, J., Aizpurua, J., and Hillenbrand, R. Terahertz Near-Field Nanoscopy of Mobile Carriers in Single Semiconductor Nanodevices. *Nano Letters*, **8**, 3766 (2008).

[47] Eisele, M., Cocker, T.L., Huber, M.A., Plankl, M., Viti, L., Ercolani, D., Sorba, L., Vitiello, M.S., and Huber, R. Ultrafast multi-terahertz nano-spectroscopy with sub-cycle temporal resolution. *Nature Photonics*, **8**, 841 (2014). 3, 4, 46

[48] Adam, A.J.L. Review of Near-Field Terahertz Measurement Methods and Their Applications. *Journal of Infrared, Millimeter, and Terahertz Waves*, **32**, 976 (2011). 3

[49] Blanchard, F., Doi, A., Tanaka, T., Hirori, H., Tanaka, H., and Kadoya, Y. Real-time terahertz near-field microscope. *Optics Express*, **19**, 3523 (2011). 3

[50] Yada, H., Nagai, M., and Tanaka, K. Origin of the fast relaxation component of water and heavy water revealed by terahertz time-domain attenuated total reflection spectroscopy. *Chemical Physics Letters*, **464**, 166 (2008). xxi, 3, 103, 104, 105

[51] Macfaden, A.J., Reno, J.L., Brener, I., and Mitrofanov, O. 3 μm aperture probes for near-field terahertz transmission microscopy. *Applied Physics Letters*, **104**, 011110 (2014). 3, 46

[52] Masson, J.B., Sauviat, M.P., Martin, J.L., and Gallot, G. Ionic contrast terahertz near-field imaging of axonal water fluxes. *Proceedings of the National Academy of Sciences of the United States of America*, **103**, 4808 (2006). 3

[53] Chiu, C.M., Chen, H.W., Huang, Y.R., Hwang, Y.J., Lee, W.J., Huang, H.Y., and Sun, C.K. All-terahertz fiber-scanning near-field microscopy. *Optics Letters*, **34**, 1084 (2009).

[54] Acbas, G., Niessen, K.a., Snell, E.H., and Markelz, a.G. Optical measurements of long-range protein vibrations. *Nature communications*, **5**, 3076 (2014). 3

[55] Oh, S.J., Kim, S.H., Ji, Y.B., Jeong, K., Park, Y., Yang, J., Park, D.W., Noh, S.K., Kang, S.G., Huh, Y.M., Son, J.H., and Suh, J.S. Study of freshly excised brain tissues using terahertz imaging. *Biomedical optics express*, **5**, 2837 (2014). 3

[56] Ji, Y.B., Kim, S.H., Jeong, K., Choi, Y., Son, J.H., Park, D.W., Noh, S.K., Jeon, T.I., Huh, Y.M., Haam, S., Lee, S.K., Oh, S.J., and Suh, J.S. Terahertz spectroscopic imaging and properties of gastrointestinal tract in a rat model. *Biomedical optics express*, **5**, 4162 (2014). 3

[57] Swift, R.D., Wattson, R.B., Decker, J.A., Paganetti, R., and Harwit, M. Hadamard transform imager and imaging spectrometer. *Applied optics*, **15**, 1595 (1976). 4

[58] Kutyniok, G. Theory and applications of compressed sensing. *GAMM-Mitteilungen*, **36**, 79 (2013). 4, 49

[59] Candes, E., Romberg, J., and Tao, T. Robust uncertainty principles: exact signal reconstruction from highly incomplete frequency information. *IEEE Transactions on Information Theory*, **52**, 489 (2006). 4, 48

[60] Donoho, D.L. Compressed sensing. *IEEE Transactions on Information Theory*, **52**, 1289 (2006). 4

[61] Shrekenhamer, D., Watts, C.M., and Padilla, W.J. Terahertz single pixel imaging with an optically controlled dynamic spatial light modulator. *Optics Express*, **21**, 12507 (2013). 4, 18

[62] Liu, L., Rahman, S., Cheng, L.J., Fay, P., Jiang, Z., Qayyum, J., Shams, M., and Xing, H.G. Approaching real-time terahertz imaging with photo-induced coded apertures and compressed sensing. *Electronics Letters*, **50**, 801 (2014).

[63] Augustin, S., Hieronymus, J., Jung, P., and Hübers, H.W. Compressed Sensing in a Fully Non-Mechanical 350 GHz Imaging Setting. *Journal of Infrared, Millimeter, and Terahertz Waves*, **36**, 496 (2015).

[64] Watts, C.M., Shrekenhamer, D., Montoya, J., Lipworth, G., Hunt, J., Sleasman, T., Krishna, S., Smith, D.R., and Padilla, W.J. Terahertz compressive imaging with metamaterial spatial light modulators. *Nat. Photon.*, **8**, 605 (2014).

[65] Vasile, T., Damian, V., Coltuc, D., and Petrovici, M. Single pixel sensing for THz laser beam profiler based on Hadamard Transform. *Optics and Laser Technology*, **79**, 173 (2016).

[66] Chan, W.L., Charan, K., Takhar, D., Kelly, K.F., Baraniuk, R.G., and Mittleman, D.M. A single-pixel terahertz imaging system based on compressed sensing. *Applied Physics Letters*, **93** (2008). 4

[67] Chen, Q., Jiang, Z., Xu, G.X., and Zhang, X.C. Near-field terahertz imaging with a dynamic aperture. *Optics Letters*, **25**, 1122 (2000). 4

[68] Born, M. and Wolf, E. *Principles of optics : electromagnetic theory of propagation, interference and diffraction of light*. Cambridge University Press (1999). ISBN 9780521642224. 7, 11

[69] Kittel, C. *Introduction to Solid State Physics*. Wiley, New York, 8th edition (2004). ISBN 978-0471415268. 16

[70] Giles, R.H. Characterization of Material Properties at Terahertz Frequencies. *Submillimeter Technology Laboratory, University of Massachusetts* (1995). 17

[71] Lee, Y.S. *Principles of terahertz science and technology* (2009). ISBN 9780387095394. xii, xiii, 17, 18, 25, 30, 31

[72] Jin, Y.s., Kim, G.j., and Jeon, S.g. Terahertz Dielectric Properties of Polymers. *Journal of the Korean Physical Society*, **49**, 513 (2006). 17

[73] Dai, J., Zhang, J., Zhang, W., and Grischkowsky, D. Terahertz time-domain spectroscopy characterization of the far-infrared absorption and index of refraction of high-resistivity, float-zone silicon. *Journal of the Optical Society of America B*, **21**, 1379 (2004). 18, 37, 68

[74] Alius, H. and Dodel, G. Amplitude-, phase-, and frequency modulation of far-infrared radiation by optical excitation of silicon. *Infrared Physics*, **32**, 1 (1991). 18, 37, 64

[75] Cheng, L.J. and Liu, L. Optical modulation of continuous terahertz waves towards cost-effective reconfigurable quasi-optical terahertz components. *Optics Express*, **21**, 28657 (2013). 18, 37

[76] Goodman, J.W. *Introduction to Fourier optics*. Roberts & Co (2005). ISBN 9780974707723. 19, 20, 54, 55

[77] Kowarz, M.W. Homogeneous and evanescent contributions in scalar near-field diffraction. *Applied Optics*, **34**, 3055 (1995). 19, 20, 55, 68, 100

[78] Green, M.A. Self-consistent optical parameters of intrinsic silicon at 300 K including temperature coefficients. *Solar Energy Materials and Solar Cells*, **92**, 1305 (2008). xii, xv, 20, 38, 54, 57, 68

[79] Hendry, E., Hibbins, A.P., and Sambles, J.R. Importance of diffraction in determining the dispersion of designer surface plasmons. *Physical Review B - Condensed Matter and Materials Physics*, **78** (2008). 21

[80] García-Vidal, F.J., Martín-Moreno, L., and Pendry, J.B. Surfaces with holes in them: new plasmonic metamaterials. *Journal of Optics A: Pure and Applied Optics*, **7**, S97 (2005). 21

[81] Slocum, D.M., Slingerland, E.J., Giles, R.H., and Goyette, T.M. Atmospheric absorption of terahertz radiation and water vapor continuum effects. *Journal of Quantitative Spectroscopy and Radiative Transfer*, **127**, 49 (2013). 28

[82] P. E. Powers. *Fundamentals of Nonlinear Optics*. CRC Press (2011). ISBN 9781420093513, ch. 3. 28

[83] Bass, M., Franken, P.a., Ward, F., and Weinreich, G. Optic Rectification. *Physical Review Letters*, **9**, 446 (1962). 28

[84] Franken, P.A., Hill, A.E., Peters, C.W., and Weinreich, G. Generation of optical harmonics. *Physical Review Letters*, **7**, 118 (1961). 28

[85] Nahata, A., Weling, A.S., and Heinz, T.F. A wideband coherent terahertz spectroscopy system using optical rectification and electro-optic sampling. *Applied Physics Letters*, **69**, 2321 (1996). 30

[86] Ulbricht, R., Hendry, E., Shan, J., Heinz, T.F., and Bonn, M. Carrier dynamics in semiconductors studied with time-resolved terahertz spectroscopy. *Reviews of Modern Physics*, **83**, 543 (2011). 36, 98

[87] Furman, S.A. and Tikhonravov, A.V. *Basics of optics of multilayer systems*. World Scientific Publishing (1992). ISBN 2863321102. 36

[88] Jeon, T.I. and Grischkowsky, D. Nature of Conduction in Doped Silicon. *Physical Review Letters*, **78**, 1106 (1997). 37

[89] Gaubas, E. and Vanhellemont, J. Comparative Study of Carrier Lifetime Dependence on Dopant Concentration in Silicon and Germanium. *Journal of The Electrochemical Society*, **154**, H231 (2007). 37, 41

[90] Withayachumnankul, W., Png, G.M., Yin, X., Atakaramians, S., Jones, I., Lin, H., Ung, B.S.Y., Balakrishnan, J., Ng, B.W.H., Ferguson, B., Mickan, S.P., Fischer, B.M., and Abbott, D. T-Ray Sensing and Imaging. *Proceedings of the IEEE*, **95**, 1528 (2007). 41

[91] Yates, F. Complex Experiments. *Supplement to the Journal of the Royal Statistical Society*, **8**, 27 (1935). 42

[92] Sloane, N.J. Multiplexing Methods in Spectroscopy. *Mathematics Magazine*, **52**, 71 (1979). 44, 65

[93] Bethe, H.A. Theory of Diffraction by Small Holes. *Physical Review*, **66**, 163 (1944). 46

[94] Mitrofanov, O., Lee, M., Hsu, J.W.P., Pfeiffer, L.N., West, K.W., Wynn, J.D., and Federici, J.F. Terahertz pulse propagation through small apertures. *Applied Physics Letters*, **79**, 907 (2001). 46

[95] Harwit, M. and Sloane, N.J.A.N.J.A. *Hadamard transform optics*. Academic Press (1979). ISBN 9780123300508. 47, 65, 83

[96] Natarajan, B.K. Sparse Approximate Solutions to Linear Systems. *SIAM Journal on Computing*, **24**, 227 (1995). 49

[97] Chen, S.S., Donoho, D.L., and Saunders, M.A. Atomic Decomposition by Basis Pursuit. *SIAM REVIEW c Society for Industrial and Applied Mathematics*, **43**, 129 (2001). 49

[98] Huang, Y., Ng, M.K., and Wen, Y.w. A Fast Total Variation Minimization Method for Image Restoration (2008). 50, 84

[99] Candes, E. and Romberg, J. l1-magic: Recovery of sparse signals via convex programming. *https://statweb.stanford.edu/~candes/l1magic/*, **4**, 14 (2005). 50

[100] Aβmann, M. and Bayer, M. Compressive adaptive computational ghost imaging. *Scientific Reports*, **3**, 405 (2013). 50, 86

[101] Sun, B., Edgar, M.P., Bowman, R., Vittert, L.E., Welsh, S., Bowman, A., and Padgett, M.J. 3D Computational Imaging with Single-Pixel Detectors. *Science*, **340**, 844 (2013). 64

[102] Griffiths, D.J.D.J. *Introduction to electrodynamics*. Prentice-Hall of India (2007). ISBN 9788120316010. 71

[103] Edgar, M.P., Gibson, G.M., Bowman, R.W., Sun, B., Radwell, N., Mitchell, K.J., Welsh, S.S., and Padgett, M.J. Simultaneous real-time visible and infrared video with single-pixel detectors. *Scientific Reports*, **5**, 10669 (2015). xvii, 73, 74, 84

[104] Sarid, D. and Challener, W.A. *Modern introduction to surface plasmons : theory, Mathematica modeling, and applications*. Cambridge University Press (2010). ISBN 9780521767170. 76

[105] Daubechies, I. The wavelet transform, time-frequency localization and signal analysis. *IEEE transactions on information theory*, **36**, 961 (1990). 86

[106] Castro Neto, A.H., Peres, N.M.R., Novoselov, K.S., and Geim, A.K. The electronic properties of graphene (2009). 88

[107] George, P.A., Strait, J., Dawlaty, J., Shivaraman, S., Chandrashekhar, M., Rana, F., and Spencer, M.G. Ultrafast Optical-Pump Terahertz-Probe Spectroscopy of the Carrier Relaxation and Recombination Dynamics in Epitaxial Graphene. *Nano Letters*, **8**, 4248 (2008). 88

[108] Dawlaty, J.M., Shivaraman, S., Chandrashekhar, M., Rana, F., and Spencer, M.G. Measurement of ultrafast carrier dynamics in epitaxial graphene. *Applied Physics Letters*, **92**, 42116 (2008).

[109] Choi, H., Borondics, F., Siegel, D.A., Zhou, S.Y., Martin, M.C., Lanzara, A., and Kaindl, R.A. Broadband electromagnetic response and ultrafast dynamics of few-layer epitaxial graphene. *Applied Physics Letters*, **94**, 172102 (2009). 90

[110] Wang, H., Strait, J.H., George, P.A., Shivaraman, S., Shields, V.B., Chandrashekhar, M., Hwang, J., Rana, F., Spencer, M.G., Ruiz-Vargas, C.S., and Park, J. Ultrafast relaxation dynamics of hot optical phonons in graphene. *Applied Physics Letters*, **96**, 81917 (2010).

[111] Hale, P.J., Hornett, S.M., Moger, J., Horsell, D.W., and Hendry, E. Hot phonon decay in supported and suspended exfoliated graphene. *Physical Review B*, **83**, 121404 (2011). 88

[112] Geim, A.K. and Novoselov, K.S. The rise of graphene. *Nature materials*, **6**, 183 (2007). 88

[113] Balandin, A.A., Ghosh, S., Bao, W., Calizo, I., Teweldebrhan, D., Miao, F., and Lau, C.N. Superior Thermal Conductivity of Single-Layer Graphene. *Nano Letters*, **8**, 902 (2008). 88

[114] Zhang, Y., Brar, V.W., Girit, C., Zettl, A., and Crommie, M.F. Origin of spatial charge inhomogeneity in graphene. *Nature Physics*, **5**, 722 (2009). 88

[115] Gammelgaard, L., Caridad, J.M., Cagliani, A., Mackenzie, D.M.A., Petersen, D.H., Booth, T.J., and Bøggild, P. Graphene transport properties upon exposure to PMMA processing and heat treatments (2014).

[116] Yu, Q., Jauregui, L.A., Wu, W., Colby, R., Tian, J., Su, Z., Cao, H., Liu, Z., Pandey, D., Wei, D., Chung, T.F., Peng, P., Guisinger, N.P., Stach, E.A., Bao, J., Pei, S.S., and Chen, Y.P. Control and characterization of individual grains and grain boundaries in graphene grown by chemical vapour deposition. *Nature Materials*, **10**, 443 (2011).

[117] Eun Lee, J., Ahn, G., Shim, J., Sik Lee, Y., and Ryu, S. optical separation of mechanical strain from charge doping in graphene. *Nature Communications*, **3** (2012). 88, 89, 90

[118] Ferrari, A.C., Meyer, J.C., Scardaci, V., Casiraghi, C., Lazzeri, M., Mauri, F., Piscanec, S., Jiang, D., Novoselov, K.S., Roth, S., and Geim, A.K. Raman Spectrum of Graphene and Graphene Layers. *Physical Review Letters*, **97**, 187401 (2006). 89

[119] Das, A., Pisana, S., Chakraborty, B., Piscanec, S., Saha, S.K., Waghmare, U.V., Novoselov, K.S., Krishnamurthy, H.R., Geim, A.K., Ferrari, A.C., and Sood, A.K. Monitoring dopants by Raman scattering in an electrochemically top-gated graphene transistor. *Nature Nanotechnology*, **3**, 210 (2008). 89

[120] Dresselhaus, M.S., Jorio, A., Souza Filho, A.G., and Saito, R. Defect characterization in graphene and carbon nanotubes using Raman spectroscopy. *Philosophical transactions. Series A, Mathematical, physical, and engineering sciences*, **368**, 5355 (2010). 89, 94

[121] Can\textbackslashccado, L.G., Jorio, A., Ferreira, E.H.M., Stavale, F., Achete, C.A., Capaz, R.B., Moutinho, M.V.O., Lombardo, A., Kulmala, T.S., and Ferrari, A.C. Quantifying Defects in Graphene via Raman Spectroscopy at Different Excitation Energies. *Nano Letters*, **11**, 3190 (2011).

[122] Eckmann, A., Felten, A., Mishchenko, A., Britnell, L., Krupke, R., Novoselov, K.S., and Casiraghi, C. Probing the Nature of Defects in Graphene by Raman Spectroscopy. *Nano Letters*, **12**, 3925 (2012).

[123] Froehlicher, G. and Berciaud, S. Raman spectroscopy of electrochemically gated graphene transistors: Geometrical capacitance, electron-phonon, electron-electron, and electron-defect scattering. *Physical Review B*, **91**, 205413 (2015). 89, 94

[124] Liu, C.H., Chang, Y.C., Norris, T.B., and Zhong, Z. Graphene photodetectors with ultra-broadband and high responsivity at room temperature. *Nature Nanotechnology*, **9**, 273 (2014). 89

[125] Koppens, F.H.L., Mueller, T., Avouris, P., Ferrari, A.C., Vitiello, M.S., and Polini, M. Photodetectors based on graphene, other two-dimensional materials and hybrid systems. *Nature Nanotechnology*, **9**, 780 (2014). 89

[126] Docherty, C.J., Lin, C.T., Joyce, H.J., Nicholas, R.J., Herz, L.M., Li, L.J., and Johnston, M.B. Extreme sensitivity of graphene photoconductivity to environmental gases. *Nature communications*, **3**, 1228 (2012). 89, 90

[127] Tielrooij, K.J., Song, J.C.W., Jensen, S.A., Centeno, A., Pesquera, A., Zurutuza Elorza, A., Bonn, M., Levitov, L.S., and Koppens, F.H.L. Photoexcitation cascade and multiple hot-carrier generation in graphene. *Nature Physics*, **9**, 248 (2013). 90, 94

[128] Freitag, M., Low, T., Xia, F.N., and Avouris, P. Photoconductivity of biased graphene. *Nature Photonics*, **7** (2013).

[129] Frenzel, A.J., Lui, C.H., Shin, Y.C., Kong, J., and Gedik, N. Semiconducting-to-metallic photoconductivity crossover and temperature-dependent Drude weight in graphene (2014). 89, 90, 94

[130] Jensen, S.A., Mics, Z., Ivanov, I., Varol, H.S., Turchinovich, D., Koppens, F.H.L., Bonn, M., and Tielrooij, K.J. Competing Ultrafast Energy Relaxation Pathways in Photoexcited Graphene. *Nano Letters*, **14**, 5839 (2014). 89, 90, 94

[131] Shi, S.F., Tang, T.T., Zeng, B., Ju, L., Zhou, Q., Zettl, A., and Wang, F. Controlling Graphene Ultrafast Hot Carrier Response from Metal-like to Semiconductor-like by Electrostatic Gating. *Nano Letters*, **14**, 1578 (2014). 89, 93

[132] Shi, S.F., Tang, T.T., Zeng, B., Ju, L., Zhou, Q., Zettl, A., and Wang, F. Controlling graphene ultrafast hot carrier response from metal-like to semiconductor-like by electrostatic gating. *Nano letters*, **14**, 1578 (2014). 90, 94

[133] Stantchev, R.I., Sun, B., Hornett, S.M., Hobson, P.A., Gibson, G.M., Padgett, M.J., and Hendry, E. Noninvasive, near-field terahertz

imaging of hidden objects using a single-pixel detector. *Science Advances*, **2**, e1600190 (2016). 91, 101

[134] Mitrofanov, O., Yu, W., Thompson, R., Jiang, Y., Greenberg, Z., Palmer, J., Brener, I., Pan, W., Berger, C., de Heer, W., and Jiang, Z. Terahertz near-field imaging of surface plasmon waves in graphene structures (2015). 91

[135] Chen, J., Badioli, M., Alonso-González, P., Thongrattanasiri, S., Huth, F., Osmond, J., Spasenović, M., Centeno, A., Pesquera, A., Godignon, P., Zurutuza Elorza, A., Camara, N., García de Abajo, F.J., Hillenbrand, R., and Koppens, F.H.L. Optical nano-imaging of gate-tunable graphene plasmons. *Nature*, **487**, 77 (2012). 91

[136] Alonso-González, P., Nikitin, A.Y., Gao, Y., Woessner, A., Lundeberg, M.B., Principi, A., Forcellini, N., Yan, W., Vélez, S., Huber, A.J., Watanabe, K., Taniguchi, T., Casanova, F., Hueso, L.E., Polini, M., Hone, J., Koppens, F.H.L., and Hillenbrand, R. Acoustic terahertz graphene plasmons revealed by photocurrent nanoscopy. *Nature Nanotechnology*, pages 1–16 (2016).

[137] Lundeberg, M.B., Gao, Y., Woessner, A., Tan, C., Alonso-González, P., Watanabe, K., Taniguchi, T., Hone, J., Hillenbrand, R., and Koppens, F.H.L. Thermoelectric detection and imaging of propagating graphene plasmons. *Nature Mater.*, page doi:10.1038/nmat4755 (2016). 91

[138] Low, T. and Avouris, P. Graphene plasmonics for terahertz to mid-infrared applications (2014). 91

[139] Jablan, M., Buljan, H., and Soljačić, M. Plasmonics in graphene at infrared frequencies. *Physical Review B - Condensed Matter and Materials Physics*, **80** (2009). 91

[140] Hornett, S.M., Stantchev, R.I., Vardaki, M.Z., Beckerleg, C., and Hendry, E. Subwavelength Terahertz Imaging of Graphene Photoconductivity. *Nano Letters*, **16**, 7019 (2016). 94

[141] Hendry, E., Koeberg, M., O'Regan, B., and Bonn, M. Local Field Effects on Electron Transport in Nanostructured TiO ₂ Revealed by Terahertz Spectroscopy. *Nano Letters*, **6**, 755 (2006). 94

[142] Stantchev, R.I., Hornett, S.M., Hobson, P.A., and Hendry, E. Enhanced THz transmission and imaging of a subwavelength slit via light-induced diffraction. *Physical Review A - Atomic, Molecular, and Optical Physics*, **92** (2015). 101

[143] Hendry, E., Garcia-Vidal, F.J., Martin-Moreno, L., Rivas, J.G., Bonn, M., Hibbins, A.P., and Lockyear, M.J. Optical control over surface-plasmon-polariton-assisted THz transmission through a slit aperture. *Physical Review Letters*, **100** (2008). 101

[144] Sophia Fox, A.J., Bedi, A., and Rodeo, S.A. The basic science of articular cartilage: structure, composition, and function. *Sports health*, **1**, 461 (2009). 102, 103

[145] Eyre, D. Collagen of articular cartilage. *Arthritis Res*, **4**, 30 (2002). 102

[146] Pritzker, K.P.H., Gay, S., Jimenez, S.A., Ostergaard, K., Pelletier, J.P., Revell, K., Salter, D., and van den Berg, W.B. Osteoarthritis cartilage histopathology: Grading and staging. *Osteoarthritis and Cartilage*, **14**, 13 (2006). 102

[147] Minns, R.J. and Steven, F.S. The collagen fibril organization in human articular cartilage. *Journal of anatomy*, **123**, 437 (1977). 103

[148] Lane, J.M. and Weiss, C. Review of articular cartilage collagen research. *Arthritis & Rheumatism*, **18**, 553 (1975). 103

[149] Houle, M.A., Couture, C.A., Bancelin, S., Van der Kolk, J., Auger, E., Brown, C., Popov, K., Ramunno, L., and L??gar??, F. Analysis of forward and backward Second Harmonic Generation images to probe the nanoscale structure of collagen within bone and cartilage. *Journal of Biophotonics*, **8**, 993 (2015). 103

[150] Beard, M.C., Turner, G.M., and Schmuttenmaer, C.A. Terahertz Spectroscopy. *The Journal of Physical Chemistry B*, **106**, 7146 (2002). 105

[151] Sun, J., Niehues, G., Forbert, H., Decka, D., Schwaab, G., Marx, D., and Havenith, M. Understanding THz spectra of aqueous solutions: Glycine in light and heavy water. *Journal of the American Chemical Society*, **136**, 5031 (2014). 105

[152] Liu, X., Parrott, E.P.J., Ung, B.S.Y., and Pickwell-MacPherson, E. Exploiting total internal reflection geometry for efficient optical modulation of terahertz light. *APL Photonics*, **1**, 076103 (2016). 109